DISSOLUTION KINETICS OF CALCIUM ALUMINATE IN STEELMAKING SLAGS

DISSOLUTION KINETICS OF CALCIUM ALUMINATE IN STEELMAKING SLAGS

BY KEYAN MIAO, B. ENG

A Thesis Submitted to the School of Graduate Studies in Partial Fulfilment of the Requirements for the Degree Master of Engineering

Master of Engineering (2017) McMaster University

Materials Science and Engineering Hamilton, Ontario

TITLE: Dissolution Kinetics of Calcium Aluminate in Steelmaking Slags

AUTHOR: Keyan Miao, B. Eng. (McMaster University, Canada)

SUPERVISOR: Dr. Neslihan Dogan

NUMBER OF PAGES: xv, 134

Lay Abstract

The present work is a pioneer study on the dissolution of calcium aluminate particles in liquid oxide mixtures using the unique real-time observation approach. Experiments were conducted to provide a better understanding of the effects of various steelmaking conditions on inclusion removal during the refinement of liquid steel.

An existing dissolution model is further refined by introducing an additional parameter that is correlated to the properties of oxide mixtures. It has been found that the dissolution model can be applied not only to calcium aluminate inclusions but also to alumina inclusions. Hence, the approach proves the potential university nature of the dissolution model.

A clear understanding of the dissolution kinetics of inclusions helps to optimize the current steelmaking routes and enhance the removability of inclusions. Steel with a minimum amount of inclusions has better properties from all aspects, which improves its applicability in all fields.

Abstract

Inclusion removal is critical for the production of clean steel. A better understanding of removal processes require knowledge of the effect of process parameters on dissolution kinetics. The present research focuses on the kinetics of calcium aluminate inclusion dissolution in relevant steelmaking slags that contain CaO, Al_2O_3 and SiO_2.

In-situ observation of inclusion dissolution in slag is conducted using a high temperature, confocal scanning laser microscope (HT-CSLM). The particles used in this experimental work are produced in the laboratory and the production technique is explained in detail. The change in particle size is recorded with time and the effects of temperature, slag composition and inclusion morphology are investigated. The images are extracted from video and they are analysed to record the change in equivalent radius of a single particle during the dissolution process. The original and normalized dissolution data is used to determine the dissolution mechanism and to improve existing dissolution models.

It has been found that an increase in temperature increases the dissolution rate. At 1550°C and 1600°C, there is no product layer formation at the slag-inclusion interface and so, the dissolution process is faster. Slag composition shows a significant influence on the dissolution kinetics due to differences in the dissolution driving force and viscosity. Additionally, the dissolution rate depends on the morphology of inclusion as available reaction sites vary significantly.

Rate limiting steps are discussed based on the shrinking core model and diffusion in stagnant fluid model. It is shown that the rate limiting step for dissolution is the diffusion

through a product layer at 1500°C whereas it is mass transfer in slag at 1550°C and 1600°C. The diffusion coefficient of alumina is obtained by applying a one-dimension diffusion model. The calculated results varied between 5.5×10^{-11} and 2.6×10^{-10} m^2/s depending on experimental conditions. Slag viscosity was found to be an important parameter for the modelling of the dissolution process. A modification to the correlation between the correction coefficient and slag viscosity was proposed. This modification improved the prediction of the dissolution path for calcium aluminate and alumina inclusions in steelmaking slags. This novel study provides an understanding of dissolution mechanisms and it offers data on the dissolution rate of CA_2 inclusions in the slags related to the process of steelmaking. The results from this work can be used by steelmakers to aid in process design.

Acknowledgements

I am greatly indebted to my supervisor, Dr. Neslihan Dogan for the encouragement, guidance and support throughout my study. I would like to express my gratitude to her for all I have learned from her.

I wish to thank the faculty, researchers, staff and graduate students in the Department of Materials Science and Engineering in the course of my study. I am grateful to Dr. K. S. Coley, Dr. Wangzhong Mu and Dr. Kezhuan Gu for their help and great ideas. I appreciate the assistance I received from the fellow graduate students Mukesh Sharma and Michelia Alba.

I am also grateful for the support of my parents throughout my graduate study.

Table of Contents

Table of Figures

Table of Tables

Symbols and abbreviations

A	Surface area
ΔA	Error of surface area
Bi	Biot number
C	Concentration
C_0	Initial concentration
C^B	Bulk concentration
C^i	Interfacial concentration
C^P	Concentration in particle
ΔC	Concentration difference
D	Diffusion coefficient
F_g	Gravitational force
F_σ	Capillary force
F_μ	Friction force
$\Delta G°$	Gibbs free energy change at standard state
J	Mass transfer flux
K	Equilibrium constant
M	Molar mass
Me	Arbitrary metal
N	Mole of substance
N_r	Relative Si to S transfer rate
P	Pressure
P*	Critical nucleation pressure
P^A	Ambient pressure
P^{EX}	Excess nucleation pressure
P^F	Ferrostatic pressure
Pe	Peclet number
R	Inclusion equivalent radius at time t
R_0	Initial inclusion equivalent radius

ΔR	Error of equivalent radius
Re	Reynolds number
Sc	Schemit number
T	Temperature
T_b	Metal bath temperature
T^{lc}	Calcium alloy wire liquidus temperature
T_{BS}	Metal bath superheat
V	Volume
X	Mole fraction
a	Activity
b	Stoichiometric constant
d	Diameter
f	Correction coefficient
g	Gravitational acceleration
h	Henrian activity
h_1	Heat convection coefficient
h_2	Equilibrium slag height
k	Dimensionless saturation concentration
k_1	Chemical reaction constant
k_2	Rate constant
k_b	Boltzmann constant
k_w	Effective thermal conductivity
m	Mass
r	Radical distance
t	Time
x	Distance from inclusion surface
α_L	Linear thermal expansion coefficient
ε	Labyrinth factor
η	Dynamic viscosity
θ	Contact angle

θ'	Dimensionless bath temperature
λ	Average jump distant of diffusing ion
ρ	Molar density
ρ'	Density
ρ'_0	Standard state density
σ_{sg}	Inclusion-gas interfacial tension
σ_{sl}	Inclusion-slag interfacial tension
σ_{sm}	Inclusion-metal interfacial tension
σ_{lm}	Slag-metal interfacial tension
τ	Total dissolution time
υ	Velocity
φ	Porosity
%R	Calcium recovery rate
$\cos\theta_{IMS}$	Overall wettability

Chapter 1 Introduction

There has been an increasing demand for the production of clean steel with a low inclusion content. Steel cleanliness largely depends on the size, shape, chemistry and number of inclusions in the final steel product [1]. Although the specific requirements of allowable inclusion content and size vary according to the application, the common requirement is the need to minimize the amount and size of the inclusions and to control the composition and size distribution in the final product. These inclusions can be controlled by two approaches: the modification of the composition and morphology of the inclusions or the removal of inclusions to the waste slag phase.

Oxide and sulphide inclusions can be modified with the addition of calcium using powder injection or wire feeding. A well-known example is the modification of solid alumina inclusions into liquid or partially liquid calcium aluminates [2]. Insufficient or superfluous addition of calcium leads to incomplete or excessive modification of alumina inclusions and the formation of unwanted inclusions such as $CaO.2Al_2O_3$ and $CaO.6Al_2O_3$ that can cause rapid clogging of pouring tubes and reversion of sulfur to the melt.

The resulting inclusions would ideally be removed from the liquid steel to slag phase in the ladle, tundish or mold prior to casting. Therefore, it is important to understand the inclusion-slag interaction in order to improve the removability of inclusions from liquid steel. During ladle refining, inclusions are transported to the steel-slag interface where they are separated from metal and dissolved in the slag. Fast dissolution kinetics help to prevent the re-entrainment of inclusions into liquid steel [3].

Early research [4] that is relevant to the kinetics of inclusion removal has been obtained by using a technique in which a cm-size refractory rod is immersed in a slag for a period of time, removed and then analysed for slag corrosion and/or penetration. Although much has been learned using this approach, the difference in scale from bulk materials to inclusions is likely to have a significant bearing on the dissolution kinetics of inclusions in a slag and this will certainly result in influencing the capillary effects. Additionally, the data that is obtained using an indirect (dip test) procedure relies on a comparison of the initial and final conditions of a sample.

The confocal scanning laser microscope (CSLM) technique allows for the continuous in-situ observation of micron-size samples in real time and at a high resolution. This is a unique feature of the CSLM technique that would not be possible by most other conventional imaging techniques in the conditions that are relevant to the steelmaking process. The process overcomes the drawbacks of the dipping technique.

Several researchers [5–7] have applied the CSLM technique to study the dissolution behaviour of a single oxide particle in slag. The high resolution, fast scanning rates, sharp image quality of the microscope and quantitative analysis of the images provide vital information about the dissolution kinetics and mechanism of inclusions dissolution in slag. However, the CSLM technique has been applied to limited inclusion types, such as Al_2O_3, $MgAl_2O_4$, MgO, CaO and SiO_2.

The calcium dialuminate ($CaO{\cdot}2Al_2O_3$) inclusions are harmful to productivity and steel [1]. With limited time between calcium injection and tapping, the formation of solid calcium aluminates is essentially inevitable. The objective of this study is to develop a fundamental

understanding of the removal of calcium aluminate inclusions during the refining of liquid steel and to find a way to accelerate dissolution and improve steel cleanliness. The relationships between the dissolution rate, temperature, slag SiO_2 content and inclusion morphology are examined. This research applies both in-situ dissolution observation and a post-experiment slag analysis to provide a better understanding of the slag-inclusion interaction. The results from this work will assist steelmakers with optimizing their process parameters for better inclusion removal in processes that deal with steel refining.

Chapter 2 Literature Review

2.1 Steel Refining

The term steel refining refers all the treatments done after oxygen steelmaking and before casting, shown as the boxed process in Figure 2.1 [8]. Primary steelmaking involves converting liquid iron from a blast furnace and steel scrap into steel via basic oxygen steelmaking or melting scrap steel and direct reduced iron (DRI) in an electric arc furnace. Then liquid steel is refined to acquire correct composition and remove the undesired constituents, after which it can be cast. In the context of this thesis, "refining" refers to the secondary refining as opposed to primary refining during oxygen steelmaking. The main tasks of steel refining facilities in modern steelmaking plants are to precisely control and homogenize steel chemistry, further increase cleanliness to satisfy requirements on final properties [9].

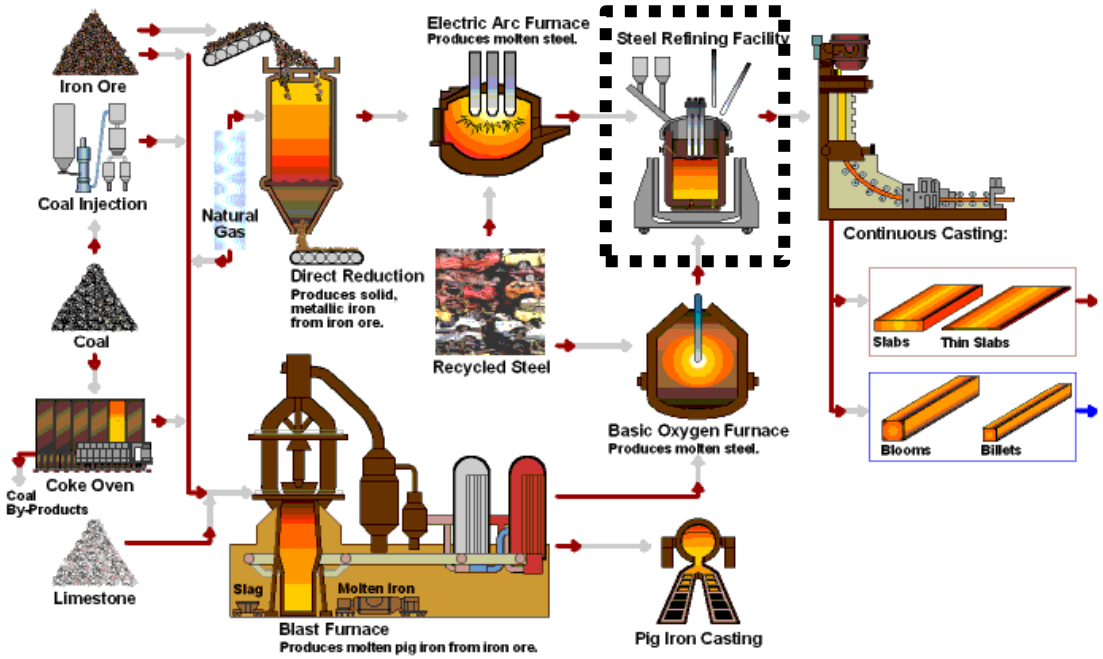

Figure 2.1 Flow line of steelmaking [8]

Numerous of refining techniques and equipment have been developed over the years. Details of these techniques can be found elsewhere [2,9,10]. Although these techniques have different metallurgical functions and structures, successful equipment all share three characteristics [11].

1. Secondary refining, which includes decarburization, desulfurization, dephosphorization, degassing, removing inclusions and adjusting steel chemistry.
2. Providing excellent conditions for reaction kinetics, that is vacuuming, gas stirring, degassing and increase the number of reaction sites.
3. Avoiding secondary oxidation and dissolution of gas during liquid steel transferring. Tapping from the nozzle to avoid direct contact between steel and air.

2.2 Steel Deoxidation

The crude steel after primary steelmaking processes has high oxygen content varying from approximately 200 to 800 ppm depending on the blowing practice [12]. The solubility of oxygen in liquid steel is considerably higher than solid. Hence oxygen will be rejected during the solidification process. Oxygen forms gas bubble blisters and oxides, which are detrimental to the casting process and the quality of the final products [12].

The oxygen content can be reduced by deoxidation process during steel refining. This process involves adding metals into the steel. These metals react with oxygen to form oxides called inclusions. The general deoxidation reaction of metal Me is written in Equation (2.1). The strength of the deoxidants is determined by oxygen affinity, associated with equilibrium constants of deoxidation reactions[13]. Deoxidation strength also depends on the activity of deoxidation products. Lower the oxide activity, stronger the deoxidation strength of the corresponding deoxidant [13]. The deoxidation strength of commonly applied metals would increase in the following order: Mn, Si, Al, Ca [10]. Different deoxidation agents are used depending on the desired level of deoxidation. The minimum dissolved oxygen content that can be possibly achieved with Mn is 100 – 200 ppm. Steel is called to be "semi-killed" if dissolved oxygen content is reduced to about 15 – 70 ppm by adding Mn followed by Si. Killed steel contains very low dissolved oxygen, (2 - 4 ppm) and is usually achieved with Al and Ca deoxidation [2]. Even though the strength of deoxidants can be predictable by thermodynamics, it is important to realize that the actual final oxygen content in steel also depends on the other factors such as the amount of deoxidants added and sequences if multiple deoxidants are added [12].

$$Me + x[O] = MeO_x \quad (2.1)$$

Deoxidation takes place directly or indirectly, or through vacuuming [10,12]. Direct deoxidation is also known as deoxidation by precipitation. It is done by adding deoxidants in the form of blocks, which react directly with dissolved oxygen in the steel to precipitate deoxidation products [10]. Indirect deoxidation is designed to transfer oxygen from liquid steel (high oxygen concentration) to the slag (low oxygen concentration) during deoxidation. It is achieved by adding powder deoxidant to slag to reduce the oxygen potential in slag [12]. Vacuuming deoxidation is achieved by placing the ladle under vacuum which will break the equilibrium between [O] and [C]. Reactions with C and O proceed further to produce CO gas to remove dissolve [O] and [C] [9,14]. In most of the steel refining facilities, direct deoxidation is the preferred approach [12].

The reason is mainly economic: deoxidation by precipitation takes less time and requires fewer deoxidants. However, deoxidation products form in liquid steel, which takes longer time later to float up to slag. Indirect deoxidation is not favoured because deoxidant consumption is higher in comparison to direct deoxidation. Besides, deoxidation through diffusion takes longer but can be improved with Ar stirring. Vacuum deoxidation does not consume any deoxidant. Deoxidation product is CO gas, which can be easily removed from liquid steel. However, investment in vacuuming equipment is required [15].

2.3 Inclusion Triggered Nozzle Clogging

Depending on the origins, inclusions can be classified either as endogenous or exogenous [16]. Endogenous inclusions are formed inevitably as the products of the refining process.

For example, deoxidation with Al produces Al_2O_3 [1]. Exogenous inclusions are those can be eliminated by optimizing steelmaking operations [17]. Typical examples include MgO and CaO from the refractory line of the furnace. Both types show impacts on the steel production [18].

Before casting in a mould, liquid steel is transferred from a ladle into tundish at the bottom of the ladle furnace called submerged entry nozzle (SEN). It has been found that SENs are commonly blocked by accumulating oxides and other complex inclusions, especially when casting steel grades that are deoxidized by aluminium [19,20]. A clogged nozzle restricts liquid steel from transfer freely between processes, is well known to be a challenge in continuous casting.

Two clogging mechanisms have been proposed. Snow and Shea [21] proposed that SENs are blocked by inclusions that formed in ladles far from SEN then deposit at nozzles. While other researchers, summarized by Heng Cui and co-workers [22], claimed that formation and precipitation of alumina inclusions both occur close to the SEN. Details of the mechanisms will not be discussed as they are out of the scope of this work. However, regardless of the mechanism proposed, inclusions are believed to be one of the greatest contributors of clogged nozzles.

2.4 **Inclusion Removal**

Inclusions have detrimental effects on the casting processes, and quality of final product hence must be removed. That is achieved by three steps: flotation, separation and dissolution [23]. Large size inclusions are brought from the liquid steel up to slag-steel

interface, where inclusions are dissolved into slag. Details of floatation are out of the scope of this study, therefore, will not be discussed, but a clear understanding of the behaviour of inclusions after reaches slag-metal interface is believed to be one of the fundamental knowledge required for this research.

2.4.1 Inclusion Flotation

Due to economic considerations, rinse time for calcium treated inclusions can be as short as 10 minutes [24]. Hence Ar blowing is applied to improve the rate of inclusion removal [25]. Adapting from hydrometallurgy, inclusion removal by bubble flotation contains six steps: (1) inclusions approach bubbles, (2) form liquid films between bubble and inclusion, (3) inclusions oscillation or slide on bubble surface, (4) film drainage and bubbles rupture to form three phases contact (TPS) then (5) stabilized and (6) float up [25]. This process is shown schematically in Figure 2.2.

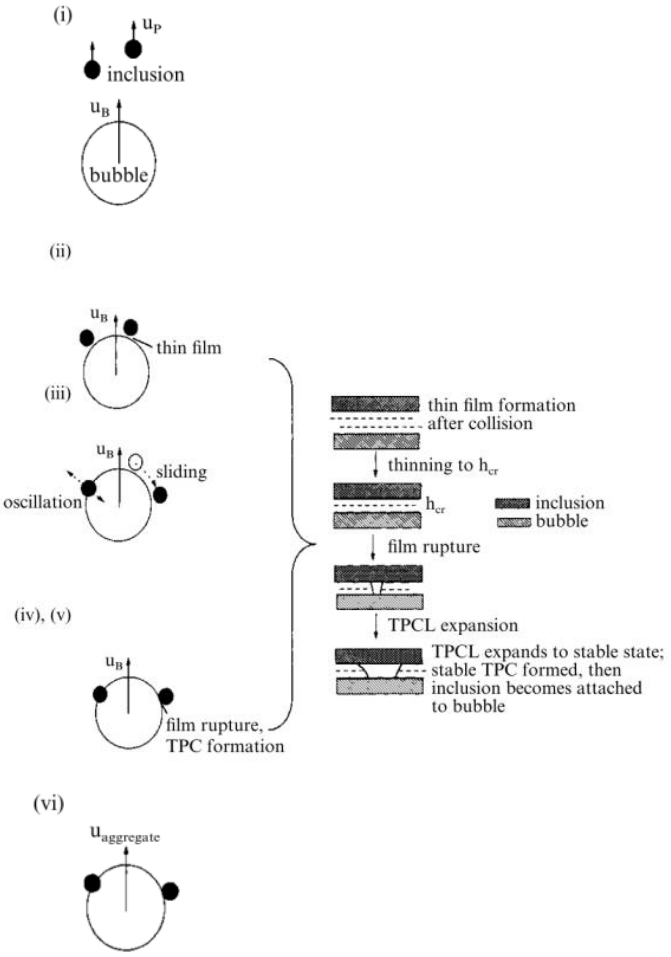

Figure 2.2 Six steps of bubble flotation [25]

Large size inclusions are easier to remove because there is a higher chance for inclusion to collide with gas bubble [25]. The critical liquid film thickness of gas bubble is also lowered, which means easier for larger size inclusions to attach to gas bubbles. The optimal bubble size for inclusion removal is between 1 and 5 mm [25]. Flotation is a complex phenomenon involving other important factors such as slag turbulence, liquid film formation and drainage time [25]. As flotation is not directly related to the inclusion dissolution kinetics, it will not be discussed in further detail here.

Limited experimental works related to the inclusion separation at the steel-slag interface were conducted [26–28]. Similar conclusions were made between researchers that the efficiency of inclusion separation largely depends on the properties of the slag such as low surface tension and low viscosity. The size of inclusions being large also plays an important role. However, the behaviour of inclusions at the slag-steel interface cannot be predicted directly based on these findings.

Mathematical models based on force balances and fluid dynamics were developed to predict the behaviour of inclusions after reaching steel-slag interface [23,26,29–31]. Among all the proposed models, the one developed by Strandh et al. [23] provides a clear indication of whether an inclusion of known size can be successfully transferred into slags with known physical properties. The model was confirmed to be valid for industrial data. It is possible to predict whether inclusions will be successfully transferred into slag, remain in liquid steel or reverse back from slag to liquid steel, referred as pass, remain and oscillate respectively in the literature. Only "pass" is the successful scenario for inclusion removal. One diagram can be generated for each type of inclusion to help visualize the modelling results, an example of CaO-Al_2O_3 (50/50 wt%) inclusion in 3 industrial ladle slags A1, B1, B2 is given in Figure 2.3. A1 and B1 have similar composition while B2 has significantly higher SiO_2 and lower Al_2O_3 content. The overall wettability $\cos\theta_{IMS}$ is expressed as Equation (2.2), which is the ratio of the difference between inclusion-metal σ_{sm} and inclusion-slag surface tension σ_{sl} to slag-metal surface tension σ_{lm}. Slag is said to be wetting if overall wettability > 0 and not wetting if < 0.

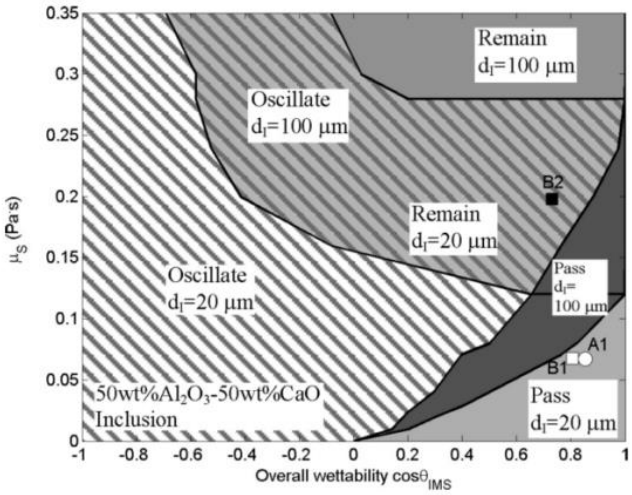

Figure 2.3 Effect of slag viscosity and overall wettability on interfacial behaviour of CaO-Al_2O_3 (50/50 wt%) inclusion [23]

$$\cos\theta_{IMS} = \frac{\sigma_{sm} - \sigma_{sl}}{\sigma_{lm}} \tag{2.2}$$

Inclusion behaviour maps like Figure 2.3 is composed of three predominant regions. The behaviour of inclusion at the slag-steel interface can be predicted based on slag viscosity (y-axis) and overall wettability (x-axis) of the system. In Figure 2.3 two inclusions with a diameter of 20 and 100 μm are considered. The "pass" region can be found at the low viscosity and high overall wettability corner of the plot, the properties of slag A1 and B1 are covered in this region. With such combination of properties, inclusions experience less restriction to their movement in slag and more restriction when trying to leave such slag. Inclusion with a 100 μm diameter pushes pass-oscillation and oscillation-remain boundary upward. This finding indicates that the model has excellent agreement with flotation theory: it is easier to remove large inclusions (diameter > 30μm) [32–34].

2.4.2 **Inclusion Dissolution**

Slags cannot be designed only to enhance the ability to absorb inclusions at the slag-steel interface. Slag compositions may be compromised to fulfil other important objectives for example desulfurization. In the case of slag being imperfect on inclusion absorption, it is critical to optimise the slag so the inclusions can be dissolved before re-entering the liquid steel.

The entire dissolution process involves a number of sequential steps. A component in the inclusion needs to dissociate from the inclusion, diffuse in inclusions and slag to be considered as "dissolved". The detail of steps of inclusion direct dissolution can be found elsewhere [35,36]. The shrinking core models (SCM) successfully capture some of the core concepts of particles dissolution [37]. It has been extensively applied in studying the dissolution kinetics of various types of inclusions [5,7,38,39].

The most commonly applied SCMs are chemical reaction control and mass transfer control at boundary layer in the literature. In this work, product layer diffusion control SCM is also considered, as it was found to be the controlling dissolution mechanism of calcium aluminate in certain conditions [35].

Table 2.1 Mathematical expression of three rate controlling mechanisms based on SCM [37]

Controlling mechanism	Dissolution profile	Total dissolution time
Chemical reaction	$\frac{t}{\tau} = 1 - \frac{R}{R_0}$ (2.3)	$\tau = \frac{\rho R_0}{bk_1 C}$ (2.4)
Boundary layer diffusion	$\frac{t}{\tau} = 1 - \left(\frac{R}{R_0}\right)^2$ (2.5)	$\tau = \frac{\rho {R_0}^2}{2bD\Delta C}$ (2.6)
Product layer diffusion	$\frac{t}{\tau} = 1 - 3\left(\frac{R}{R_0}\right)^2 + 2\left(\frac{R}{R_0}\right)^3$ (2.7)	$\tau = \frac{\rho {R_0}^2}{6bD\Delta C}$ (2.8)

The chemical reaction control assumes the chemical reaction between the solute (inclusion) and the solvent (slag) is the slowest step of the dissolution process. The rate of chemical reaction is proportional to the power of the interfacial concentration of the reactant, depending on the order of reaction rate. For reaction rate of x order, the rate of dissolution is written as Equation (2.9) [37],

$$\frac{dN}{dt} = -bk_1 AC^x \tag{2.9}$$

where b, k_1 and A are the stoichiometric constant, reaction rate constant and the slag-inclusion contact area, respectively. Writing total amount of reactant N as the product of molar density ρ and volume V, so Equation (2.9) can be transformed to Equation (2.10).

$$-\rho \frac{dR}{dt} = bk_1 C^x \tag{2.10}$$

Integrating Equation (2.10) over the corresponding range of time t and radius of inclusion R gives Equation (2.11), which predicts the change of inclusion radius over time due to slow chemical reaction. The rearranged forms of the equations for chemical reaction control mechanism and the prediction of total dissolution time are shown as Equation (2.3) and (2.4) in Table 2.1.

$$t = \frac{\rho}{bk_1C^x}(R_0 - R) \tag{2.11}$$

In the case of diffusion through boundary layer being the slowest step of inclusion dissolution, it is assumed that a constant concentration gradient of the rate-limiting species is built at the slag-particle interface once dissolution starts. The mass transfer coefficient can be related to the dimensionless numbers shown in Equation (2.12), which can be simplified to Equation (2.13) when the inclusions fall in the Stoke's regime [37]. Stoke's regime means the dissolving particles are sufficiently small or slag is very viscous so that the Reynolds number Re and Schmidt number Sc are insignificant compared to the constant value of 2 in Equation (2.12) [37].

$$\frac{k_2 d}{D} = 2 + 0.6Re^{\frac{1}{3}}Sc^{\frac{1}{2}} = 2 + 0.6\left(\frac{\eta}{\rho' D}\right)^{\frac{1}{3}}\left(\frac{v\rho' d}{\eta}\right)^{\frac{1}{2}} \tag{2.12}$$

$$k_2 = \frac{D}{R} \tag{2.13}$$

The driving force for dissolution in the case of boundary layer diffusion control is the concentration difference in the slag adjacent to the slag-inclusion interface, denoted as ΔC

in Equation (2.14). Substituting the rate constant k (Equation (2.13)) into Equation (2.14) generates Equation (2.15).

$$\frac{dN}{dt} = -bk_2 A\Delta C \tag{2.14}$$

$$\frac{dN}{dt} = -b\frac{D}{R} A\Delta C \tag{2.15}$$

Integrating Equation (2.15) over total dissolution time and rearranging the results gives the mathematical expressions of the change in inclusion radius with time t when dissolution is controlled by diffusion through boundary layer and prediction of total dissolution time τ, shown as Equation (2.5) and (2.6) in Table 2.1.

An important missing part from the original boundary layer diffusion control SCM is the effect of convection on the rate of dissolution. Yan et al. [40] claimed the mass transfer coefficients are underestimated for large particles in the case of diffusion through boundary layer control mechanism. Different mass transfer coefficients should be used based on the values of the Peclet number Pe. They proposed that Equation (2.16) and (2.17) should be used instead of Equation (2.13) for two cases which Pe > 10000 and < 10000, respectively. They claimed that the SCM with adjusted mass transfer coefficient predicts dissolution profiles better than the original boundary layer diffusion SCM. It should be noted that they validated their modelling results for a limited experimental data available in the literature.

$$k_2 = \frac{1.11D \cdot Pe^{\frac{1}{3}}}{2R} \tag{2.16}$$

$$k_2 = \frac{D\sqrt{\left(4 + 1.21Pe^{\frac{2}{3}}\right)}}{2R} \tag{2.17}$$

Another rate controlling mechanism is the diffusion through product layer. This rate controlling mechanism considers that a thin, dense and continuous reaction product layer is formed during the dissolution process. Diffusion of the solute through that layer is the slowest step, hence control the entire dissolution process. Steady state diffusion was assumed, so the mass transfer flux J is expressed in Equation (2.18) and follows Fick's First Law.

$$J = D\frac{dC}{dr} \tag{2.18}$$

Hence the rate of inclusion consumption $\frac{dN}{dt}$ can be written as Equation (2.19).

$$\frac{dN}{dt} = -4\pi R^2 D\frac{dC}{dr} \tag{2.19}$$

Integrating Equation (2.19) from the initial radius R_0 to any radius R gives Equation (2.20).

$$-\frac{dN}{dt}\left(\frac{1}{R} - \frac{1}{R_0}\right) = 4\pi D\Delta C \tag{2.20}$$

Integrating Equation (2.20) again across time t gives the mathematical expression of diffusion through product layer control SCM (Equation (2.7)) and the theoretical total dissolution time τ (Equation (2.8)) in Table 2.1.

Another modelling approach is applied to predict the dissolution rate of particles in steelmaking slags. It is based on the Fick's Second Law in spherical coordinates, and the inclusion size change was captured with the term containing the boundary velocity v (Equation (2.21)). The equation was solved numerically by Lee et al. [39].

$$\frac{dC}{dt} = D\frac{1}{r^2}\frac{d}{dr}\left(r^2\frac{dC}{dr}\right) + v\frac{dC}{dr} \tag{2.21}$$

The comparison of dissolution curves, which is represented by the normalized equivalent radius of particle vs normalized time, based on four different rate controlling mechanisms as mentioned above is provided in Figure 2.4. The controlling mechanisms can be distinguished by their characteristic shapes. The straight line represents the dissolution curve of chemical reaction control SCM. The dissolution rate is constant due to the constant solvent concentration at the slag-inclusion interface.

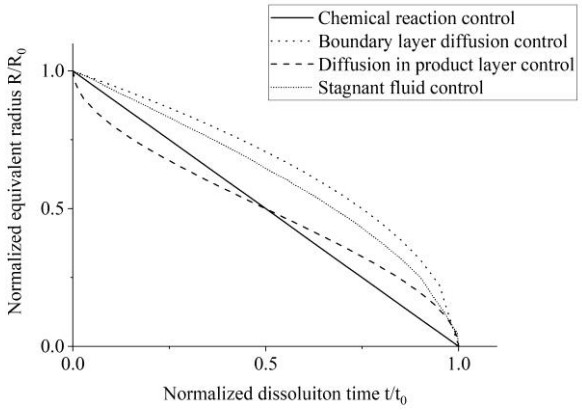

Figure 2.4 Normalized radius of a particle with respect to normalized dissolution time based on different rate controlling mechanisms

The dissolution curve for both boundary layer diffusion control SCM and the stagnant fluid control model has a parabolic shape. As the particle shrinks, the decrease of particle radius is faster due to the increasing area to volume aspect ratio. The diffusion through product layer control and diffusion through stagnant fluid control share similar shape. At the beginning of the dissolution process, the dissolution rate is faster due to high concentration gradient. As the product layer forms and thickens, the rate of diffusion slows down. Towards the end of the dissolution process, dissolution rate increases again as the volume of the particle become very small relative to the surface of the particle. The shape of dissolution curves is an important indication to suggest a dissolution mechanism and is used extensively in inclusion dissolution studies.

The dissolution models included in Figure 2.4 are developed for specific controlling mechanisms. To develop a universal inclusion dissolution model, a more fundamental dissolution model was developed based on Fick's Second Law and its analytical solution (Equation (2.22) and (2.23)), and the conservation of mass at slag-inclusion interface

(Equation (2.24)) [41]. C_0, C^i and C^P are the concentration of the rate-limiting species in the bulk of slag, slag-inclusion interface and inclusion.

$$\frac{dC}{dt} = D\frac{1}{r^2}\frac{d}{dr}\left(r^2\frac{dC}{dr}\right) \tag{2.22}$$

$$\Delta C = \frac{(C_0 - C^i)R}{r} erfc\left(\frac{r-R}{2\sqrt{Dt}}\right) \tag{2.23}$$

$$\left(C^P - C^i\right)\frac{dR}{dt} = -D\frac{dC}{dr} \tag{2.24}$$

The derivative of Equation (2.23) over distance r gives Equation (2.25), which can be substituted into the Stefan condition in Equation (2.24) to generate Equation (2.26). At the slag-inclusion interface, r = R, so Equation (2.26) can be simplified to Equation (2.27). Equation (2.27) describes the position change of slag-inclusion interface with time as a function of diffusion coefficient D, dimensionless saturation concentration k and correction coefficient f [41]. The dimensionless saturation concentration is the ratio of concentration difference between slag bulk composition and saturation concentration to concentration difference between dissolving particle concentration and saturation concentration in slag (Equation (2.28)). It is possible to estimate the diffusion coefficient D and correction coefficient f by comparing experimental data to solutions of Equation (2.27).

$$\frac{d\Delta C}{dr} = \frac{(C_0 - C^i)R}{r^2} erfc\left(\frac{r-R}{2\sqrt{Dt}}\right) + \frac{(C_0 - C^i)R}{r}\frac{e^{-\frac{(r-R)^2}{4Dt}}}{\sqrt{\pi Dt}} \tag{2.25}$$

$$\left(\frac{dR}{dt}\right)_{r=R} = D\left[\frac{(C_0 - C^i)R}{(C^P - C^i)R^2} erfc\left(\frac{R-R}{2\sqrt{Dt}}\right) + \frac{(C_0 - C^i)R}{(C^P - C^i)R}\frac{e^{-\frac{(R-R)^2}{4Dt}}}{\sqrt{\pi Dt}}\right] \quad (2.26)$$

$$\frac{dR}{dt} = -\frac{kD}{R} - k\sqrt{\frac{D}{\pi t}} \quad (2.27)$$

$$k = \frac{C^i - C_0}{C^P - C^i} \quad (2.28)$$

To be able to apply the identical dissolution model of various controlling mechanisms, correction coefficient f is introduced to Equation (2.27) to give Equation (2.29).

$$\frac{dR}{dt} = -\frac{kD}{R} - fk\sqrt{\frac{D}{\pi t}} \quad (2.29)$$

By assigning f = 1 or f = 0, Equation (2.29) represents two different profiles of concentration gradient at the slag-inclusion interface. These cases are classified into the invariant interface and invariant field conditions. Schematic diagrams of the two distinct concentration gradient are provided in Figure 2.5. The governing behaviour of the interface is believed to be determined by slag viscosity, and the mathematical treatment of this phenomenon is achieved by using a correction coefficient f [41,42].

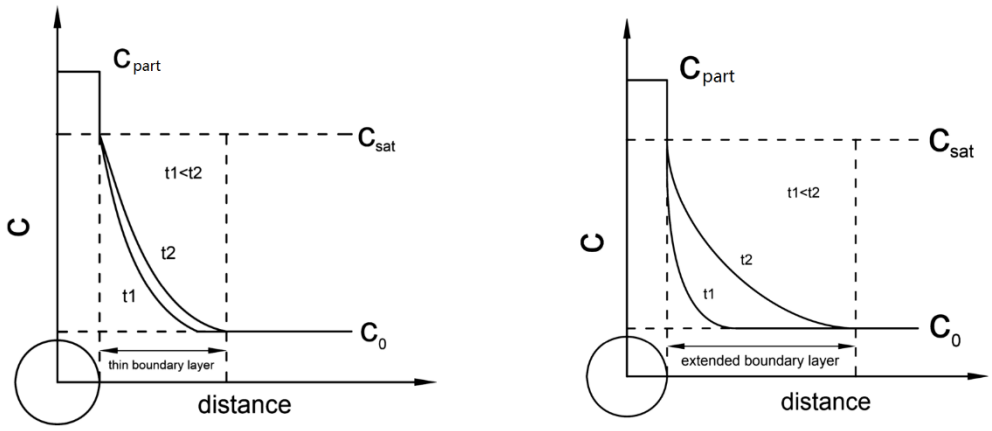

(a) (b)

Figure 2.5 Schematic diagram of concentration gradient in (a) invariant field (b) invariant interface condition [41]

For slag with low viscosity, inclusions may move freely in slag, the relative motion between inclusions and slag is fast. Moving and rotating result vigorous convection, which suppresses the development of the boundary layer. The boundary layer will be relatively thin and remain virtually unchanged throughout the dissolution process, follows the invariant field condition shown in Figure 2.5 (a). With the driving force being steady, the time-dependent term in Equation (2.29) therefore can be removed by assigning f = 0. The dissolution rate is then dominated by the change of inclusion surface area to volume ratio in the remaining of Equation (2.29). The dissolution curve exhibits parabolic shape [41].

On the other hand, inclusions are trapped in viscous slag and it is relatively difficult for inclusions to move or rotate in viscous slag. The limited motion between inclusions and slag minimizes the effect of convection on dissolution. The boundary layer hence gradually develops as shown in Figure 2.5 (b). The concentration difference is assumed to be fixed by the local equilibrium at two ends of the boundary layer. As boundary layer extends, the

concentration gradient, being dissolution driving force, decreases, resulting in reduction of the dissolution rate [41]. The dissolution curves show S-shape. For viscous slag, dissolution rate depends only on the diffusion. The correction coefficient, f equals 1.

Michelic et al. [41,42] suggested that any realistic particle dissolution is controlled by mass transport in slag between infinitely fluid and infinitely viscous, so the value of f would range between 0 and 1. The correction coefficient is related to viscosity when the solvent is liquid [42]. One mathematical correlation between correction coefficient and the slag properties was reported for SiO_2 dissolution experiments at 1450ºC [41]. Equation (2.30) suggests correction coefficients have a linear correlation with bulk slag viscosity η. Based on Figure 2.6 provided in the same literature, the correlation in Equation (2.30) can be still improved. Besides, this approach is developed for mass transfer in the liquid, so may not be valid for cases involving the formation of solid product layer at the slag-inclusion interface.

$$f = 0.15006\eta \tag{2.30}$$

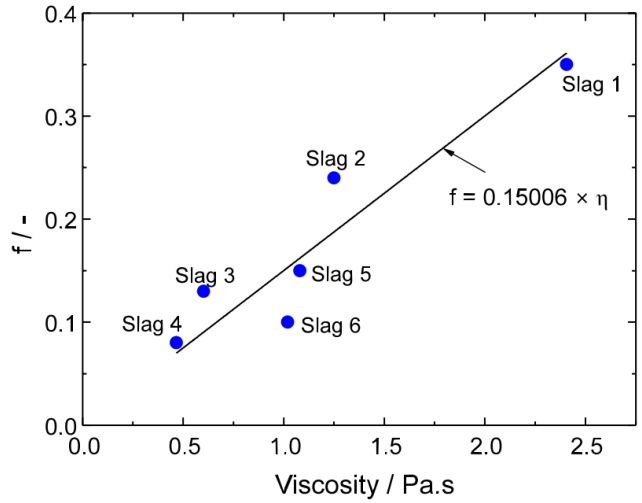

Figure 2.6 Correlation between the correction coefficient f and slag viscosity at 1450ºC [41]

2.5 **Previous Inclusion Dissolution Studies**

As in great interest of the steelmaking industry, dissolution of non-metallic inclusion such as Al_2O_3, CaO, MgO, SiO_2 and spinel has been studied extensively using high temperature confocal scanning laser microscope (HT-CSLM). The same experimental approach was used in this study.

CSLM technique allows for continuous in-situ observation of micron-size samples in real time. This is a unique feature of the CSLM technique that would be impossible by most other conventional imaging techniques in the conditions relevant to the steelmaking processes and overcomes the drawbacks of the dipping technique. The CSLM was introduced to steel research by Emi et al. [43–45] to study the crystal growth during solidification in Fe-C melts. Since then it has been used to examine dynamic changes such as particle collision, cluster formation and solidification at steelmaking temperatures

[27,28,46–49]. The basis of CSLM has not changed since its first application in the 1950s, for nerve cells visualization [50].

Confocal optics enables moving image observation of samples in real time with high magnification and high contrast even without the interference of high intensity radiant light at high temperatures. The principle of confocal microscopes is to place a pinhole aperture close to the end of the light path inside the confocal so that only light from the focal plane can pass through. With all the rest of the light block by the pinhole aperture, imaging of unfocused points are not possible [50]. A schematic drawing of a CSLM light path is shown in Figure 2.7 [51]. The laser from above is the light source, indicated as blue lines, can illuminate the volume around the focal point. The light from the illuminated volume cannot pass the dichroic beam splitter, gets deflected towards a detector. However, the light from the focal plane can only pass the pinhole to be detected, drawn as the solid green lines in Figure 2.14. While the rest of the light paths, shown as green dash lines, are obstructed by the aperture.

The scanning rate is crucial to facilitate the reaction occurrence and its rate analysis. Laser scanning in the horizontal plane is accomplished by the acoustic optic deflector, whereas the vertical position of the stage (focal plane) is controlled by the galvano mirror. The configuration and high power input of the furnace makes it possible to heat the sample up to 1700°C by radiation. The heat source is a 1.5 kW Halogen lamp focused on the sample using a gold mirror. The elliptical shape and gold coating of the mirror allow most reflected beams from the lamp to focus on the upper focal point, where the sample is placed.

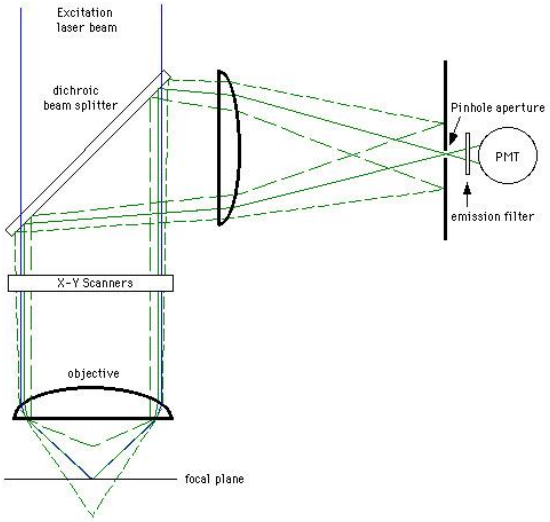

Figure 2.7 Schematic diagram of a CSLM light path [51]

A collection of the particle dissolution studies using CSLM and some studies using rotating rod/disk method is provided in the following.

2.5.1 **Al_2O_3 Dissolution**

Majority of the previous studies [52] focused on the dissolution of Al_2O_3 in steelmaking slags, as it is probably the most common inclusion detected in Al-killed steels. The summary of experimental conditions used for Al_2O_3 dissolution studies is provided in Table 2.2. Except for one study, the diameters of particles used are all below 200 μm. Slag compositions studied are industrial relevant slag compositions. The experimental temperature ranges from 1450 to 1550°C, which is about the typical steelmaking range.

Monaghan et al. [6,7,52–54] studied the dissolution of Al_2O_3 in CaO-SiO_2-Al_2O_3 slags between 1477 and 1577°C using CSLM. The dissolution times of particles with a 100 μm radius were found to significantly decrease from 600 s to less than 200 s when temperature

increases from 1477 to 1550°C. Irregular alumina were found to rotate while dissolving. Although it is well understood that the relative motion between inclusion and slag enhances convection so inclusion dissolution will be accelerated, the effect of particle rotation was not considered in the rate constant calculation. The authors were not able to conclude whether the rate controlling mechanism is the chemical reaction or diffusion in concentration boundary layer based on a comparison between the actual dissolution data and derived models. The difference between predictions based on both mechanisms was insignificant. Based on the assumption that dissolution process is controlled by diffusion at the boundary layer, the values of calculated diffusion coefficients varied from 10^{-11} to 10^{-10} m^2/s at 1550°C [52]. It was concluded that the dissolution is at least partially controlled by the mass transport because the calculated diffusion coefficient increased with an increase in temperature and it is inversely proportional to the slag viscosity according to the Eyring's relation (Equation (2.31)). In Equation (2.31), k_b and λ are the Boltzmann constant and average ion jumping distance respectively. This finding agrees well with other dissolution studies using similar slags with rotating rod method [7,35,38,52,54–56]. Rods made of the same substance as the inclusions were partially immersed in the slag and rotated to enforce convection. The dissolution kinetics were determined by recording the rod weight loss and measuring the chemistry of slag.

$$D = \frac{k_b T}{\eta \lambda} \tag{2.31}$$

Liu et al. [6] calculated Al_2O_3 diffusion coefficients based on the diffusion in stagnant fluid control model. The diffusion coefficients were varied from 2.4×10^{-11} to 9.7×10^{-11} m^2/s

between 1470 and 1630°C. The results are different from the values calculated using the SCM by Monaghan et al. [6,7,52–54].

Table 2.2 Summary of experimental conditions of Al_2O_3 dissolution studies available in the literature

Inclusion Diameter (μm)	Temperature (°C)	Slag Composition (wt%)	Ref.
100	1504	16.3CaO-19.3Al_2O_3-64.5SiO_2	[7,38,52]
	1550		
	1577		
	1477	28.0CaO -23.7Al_2O_3-48.3SiO_2	
	1504		
	1550		
138	1430	33.4CaO-19.5Al_2O_3-39.5SiO_2-7.3MgO	[55]
122	1480		
142			
112	1530		
84			
96	1550		
220	1500	33.4CaO-19.5Al_2O_3-39.5SiO_2-7.3MgO	[57]
220		36CaO-21Al_2O_3-42SiO_2-0.4MgO	
180		59CaO-36Al_2O_3-5SiO_2	
500	1470	29.7CaO-24.1Al_2O_3-46.2SiO_2	[6]
	1500		
	1550		
	1600		
	1630		
260	1450	48.4CaO-48.9Al_2O_3-1.5SiO_2-0.52MgO	[39]
	1470		
	1500		
200	1450	51.5CaO-46.6Al2O3-1.3SiO2-0.5MgO	
	1470		
	1500		
200	1450	48.4CaO-48.9Al_2O_3-0.52MgO	[3]
	1470		
	1500		
	1450	51.5CaO-46.6Al_2O_3-0.50MgO	
	1470		
	1500		

2.5.2 **CaO Dissolution**

There are few studies [58–61] available on the dissolution of CaO in transition elements free slag. Kinetics of lime dissolution has been studied mainly for oxygen steelmaking process, where slag contains constituents such as FeO_x, CaF_2 and $CaCl_2$ [62,63]

Amini et al. [60] studied the effect of additives and temperature on the dissolution rate of CaO in steelmaking slag using rotating rod method. The experimental conditions are provided in Table 2.3. A 50CaO-42Al_2O_3-8SiO_2 master slag was used as the baseline to compare with other types of slags. Additives are CaF_2, FeO_x, TiO_2 and MnO_x, which are out of the scope of the present study. However, it is important to mention that the diffusivities of CaO in the master slag varied from 1.32×10^{-9} to 3×10^{-9} m^2/s when temperature increased from 1500 to 1600°C. Sun et al. [58] studied the dissolution of CaO in slags with higher SiO_2 contents with CSLM. The diffusion coefficient was found to be 2×10^{-11} m^2/s at 1600°C. The most significant difference between the dissolution behaviour of CaO in the low and high SiO_2 slags is the presence of reaction product. No dissolution reaction product was observed during the experiments with the low silica slag. There was a 50 μm thick product layer composed of Ca_2SiO_4 (C_2S) and Ca_3SiO_5 (C_3S) observed between the CaO particle and slag. They also found the dissolution rate of CaO was faster with additional 10 wt% MgO in the slag, which will effectively reduce the formation of reaction products. They also suggested that the viscosity of slag decreases with an increase in MgO content [59]. It is worth mentioning that both studies concluded that the mass transport in slag plays an important role in the dissolution of CaO in steelmaking slags.

Table 2.3 Summary of experimental conditions of CaO dissolution studies available in the literature

Inclusion Diameter (μm)	Temperature (°C)	Slag Composition (wt%)	Ref.
800	1450, 1500, 1550, 1600	$45CaO\text{-}10Al_2O_3\text{-}45SiO_2$	[58,59]
		$30CaO\text{-}10Al_2O_3\text{-}60SiO_2$	
		$40CaO\text{-}20Al_2O_3\text{-}40SiO_2$	
		$26.7CaO\text{-}20Al_2O_3\text{-}53.3SiO_2$	
		$40CaO\text{-}10Al_2O_3\text{-}40SiO_2\text{-}10MgO$	
		$26.7CaO\text{-}10Al_2O_3\text{-}53.3SiO_2\text{-}10MgO$	
		$35CaO\text{-}20Al_2O_3\text{-}35SiO_2\text{-}10MgO$	
		$23.3CaO\text{-}20Al_2O_3\text{-}46.7SiO_2\text{-}10MgO$	
2 mm thickness	1430	$50CaO\text{-}42Al_2O_3\text{-}8SiO_2$	[60]
	1500		
	1600		
2 mm thickness	1430	$45.3CaO\text{-}45Al_2O_3\text{-}9.7SiO_2$	[61]
	1500		
	1600		

2.5.3 **Spinel Dissolution**

Mg-Al-O spinel was not studied as much as simple oxides like alumina. Some of the spinel dissolution studies are listed in Table 2.4. The initial particle size, as well as the slag composition, are given.

Monaghan et al. [64] studied the effect of different slag composition on $MgAl_2O_4$ spinel dissolution using CSLM. Mg cation and AlO_x^{y-} anions are released into the slag when spinel dissolves. By comparing dissolution profile with SCM, they concluded that the spinel dissolution is at least partially controlled by the diffusion in the boundary layer.

Diffusion of the AlO_x^{y-} anions, such as AlO_3^{3-} and AlO_4^{5-} were believed to be rate limiting species compare to Mg^{2+}. Mg^{2+} is smaller than AlO_x^{y-} anions, so they diffuse faster. Mg^{2+} therefore will have a higher diffusion coefficient, and overall kinetics is determined by diffusion of AlO_x^{y-} anions. This statement is confirmed with experimentally determined diffusion coefficients. 4.6×10^{-9} and 2.2×10^{-11} m^2/s for Mg^{2+} and AlO_x^{y-} in 40CaO-20 Al_2O_3-40SiO_2 slag [65]. Another important fact pointed out was how the dissolution of $MgAl_2O_4$ could be associated with Al_2O_3. The researchers [64] claimed that the diffusion coefficients obtained from spinel dissolution would be the same as from alumina dissolution because Al_2O_3 is the rate determining species for spinel. Similar assumptions were made by other researchers, and similar conclusions are reached [26,66,67]. Even though there is an agreement between these studies, the experimental parameters studied are still limited to develop a fundamental understanding of dissolution mechanism for spinel inclusions.

Table 2.4 Summary of experimental conditions of $MgAl_2O_4$ dissolution studies available in the literature

Inclusion Diameter (μm)	Temperature (°C)	Slag Composition (wt%)	Ref.
200	1500	$59CaO-36Al_2O_3-5SiO_2$	[26]
		$36CaO-21Al_2O_3-42SiO_2$	
		$33CaO-19.5Al_2O_3-39.5SiO_2-7.3MgO$	
70	1504	$16.3CaO-19.3Al_2O_3-64.5SiO_2$	[64]
68		$22.1CaO-21.5Al_2O_3-56.4SiO_2$	
56		$28CaO-23.7Al_2O_3-48.3SiO_2$	
195	1550	$48CaO-5.3Al_2O_3-46.7SiO_2$	[66]
169		$32.6CaO-35.7Al_2O_3-31.7SiO_2$	

2.5.4 **Limitation of Confocal Scanning Laser Microscope**

The CSLM has proven to be a useful tool in studying phenomenon related to steelmaking processes Based on the experience of the author in the present study, CSLM has some limitations. For example, in order to observe particles that are fully immersed in the slag, the slag needs to be free of considerable amounts of transition elements such as Fe, Mn, Cr or Ti. These elements affect the transparency of the system and might hinder in situ observation of the process [5,68]. Soll-Morris and co-workers [69] were able to observe the dissolution of Al_2O_3 in SiO_2-CaO-Al_2O_3-FeO slag with a maximum 9.16% FeO in dissolution experiments. According to the image they reported, the liquid slag was not transparent however the boundary of inclusion during its dissolution can be identified. Secondly, the size of the particle which can be observed in the CSLM should be in the

range of 50-1000 μm. Even though size range of inclusions of interest to steelmakers is relatively smaller, the dissolution kinetics is too fast to observe the smaller size of inclusions (< 30 μm). Also, the listed issues should also be considered: i) The relative density of particle should be considered to evaluate the particle trajectory (sinking to the bottom of the crucible or floating on the surface of the slag) during operation. The suspended particles are required to model dissolution process accurately; ii) The heating rate should be carefully set to ensure that inclusion dissolution starts at the designed temperature. In the case of slow heating rates, the particle is likely to be dissolved before reaching experimental temperature. In the case of high heating rates, the furnace temperature can exceed the experimental temperature; iii) The particle should have relatively low porosity to inhibit the bubble formation during inclusion dissolution. Otherwise it might be difficult to identify the phase boundary between particle and slag system; iv) If an accurate measurement of inclusion dissolution is desired, the amount of particle dissolved in slag should not affect the driving force considerably, and the mass of the particle should be less than 0.1wt% of the slag [39].

2.6 **Inclusion Modification by Calcium Treatment**

To reduce the detrimental effect of inclusions such as Al_2O_3 on SEN clogging, calcium is added close to the end of steel refining process mostly in forms of Ca cored wire or calcium alloyed powder. The two main purposes are to increase inclusion size and adjusting chemistry [2,13]. As explained in section 2.4.1, large inclusions are easier to be removed by flotation. The melting point of inclusions decreases with increasing Ca content, become liquid or semi-liquid calcium aluminates that do not deposit on SENs as easy as solid alumina inclusions. Calcium modification is also used to control inclusion shapes which

has shown to have an important effect on physical properties of steel for example strength [70].

2.6.1 **Calcium Dissolution**

Pure calcium has a boiling point of about 1490°C, which is lower than the typical steelmaking temperatures [13]. Therefore calcium vaporizes then dissolves in liquid steel after injection. The reaction follows Equation (2.32), where square brackets denote the dissolved calcium in liquid steel. Due to volatile nature of calcium, the majority of the injected calcium escapes from the system as calcium vapour, and only limited amount of calcium successfully dissolves [71]. The fraction of calcium dissolved is referred as calcium recovery, calcium retention or calcium yield.

$$Ca_{(g)} = [Ca] \tag{2.32}$$

Calcium yield is measured immediately after the addition because calcium concentration decreases rapidly with time due to its high reactivity and low vapour pressure. Calcium yield is defined as weight percent of calcium remaining in steel about 30 to 60 s after the injection. The values can vary from 5 to 35 wt% under different operating conditions, and the typical calcium yield is about 12 wt% [72–75]. Based on plant data in Tata Steel, S. Basak et al. [75] proposed a correlation between calcium recovery rate %R of CaSi wire and number of operation parameters, shown in Equation (2.33).

$$\%R = 179872 \cdot Bi^{-0.95}\theta'^{-1.01}{N_r}^{-0.853} \tag{2.33}$$

where Bi, θ' and Nr denote the Biot Number, dimensionless bath temperature and relative transfer rate of silicon to sulfur respectively. Mathematical expressions of the Bi, θ' and Nr are given in Equation (2.34), (2.35) and (2.36). All the related parameters are listed in Table 2.5.

$$Bi = \frac{h_1 d}{k_w} \tag{2.34}$$

$$\theta' = \frac{T_b - T_{lc}}{T_b - T_{S,mp}} \tag{2.35}$$

$$N_r = \frac{D_{Si}^{\frac{1}{2}}\left(C_{Si}^{i} - C_{Si}^{B}\right)}{D_S^{\frac{1}{2}} C_S^{B}} \tag{2.36}$$

Table 2.5 List of parameters to calculate calcium recovery rate, %R

h_1: heat convection coefficient	d: diameter of cored wire	k_w: effective thermal conductivity of wire	T_b: bath temperature
T_{lc}: wire liquidus temperature	$T_{S,mp}$: Steel melting point	D_{Si}: Si diffusivity in steel	C_{Si}^{i}: Si concentration at wire-steel interface
C_{Si}^{B}: Si concentration in bulk steel	D_S: diffusivity of S in steel	C_S^{B}: S concentration in bulk steel	Tl: liquidus temp

The authors [75] showed a good agreement between measured plant data and the theoretical value of calcium yield (All the plant data fall between ±5% of the calculated calcium yield)

and they suggested that Equation (2.33) is beneficial for industrial applications to predict calcium yield. The advantage of the proposed correlation is its accessibility. All the parameters in Equation (2.33) can be measured directly during the operations. Operators therefore can quickly adjust the configurations to optimize the process.

Ueshima et al. [72] found the calcium yield depends on the calcium vapour pressure at the boundary layer between calcium alloy and bulk steel melt. In Figure 2.8, P_{Ca}* is the critical vaporization pressure, namely the maximum calcium partial pressure without gasifying. Calcium escapes from liquid steel if localized calcium partial pressure $P_{Ca} > P_{Ca}$* so local calcium partial pressure remains below critical pressure. They quantified P_{Ca}* by summation of ambient pressure P^A, excess pressure for calcium bubble nucleation P^{EX} and ferrostatic pressure P^F which depends on the depth of entry as shown in Equation (2.37)[72].

$$P_{Ca}{}^{*} = P^{A} + P^{EX} + P^{F} \tag{2.37}$$

Equation (2.37) explains one of the reasons for feeding calcium alloys in treatments. Calcium activity is lowered when calcium is alloyed with other elements such as silicon and aluminium, also as its partial pressure. In order to retain calcium in the melt for longer time utilisation and recovery, the calcium partial pressure should be lowered [75].

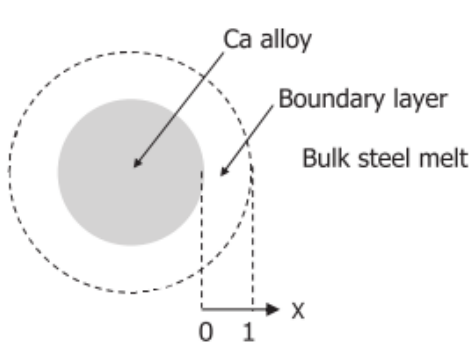

(a)

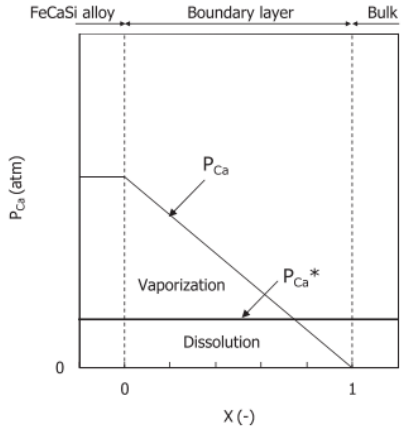

(b)

Figure 2.8 (a) Schematic diagram of dissolving calcium and the boundary layer (b) Calcium partial pressure P_{ca} and critical vaporization partial pressure P_{ca}* profile in boundary layer [72]

Lu [76] derived an equilibrium constant for Equation (2.32), valid between 1550 and 1650°C, using experimental data on calcium solubility obtained from literature [76], [77], [78]. The relationship between equilibrium constant and temperature follows Equation (2.38) [76].

$$logK_{Ca} = log\frac{P_{Ca}}{h_{Ca}} = \frac{4307.86}{T} - 4.0572 \qquad (2.38)$$

With a known critical partial pressure of calcium P_{Ca}*, it is possible to calculate the maximum solubility of calcium in liquid steel [Ca] using Equation (2.38). Calcium activity follows the Henrian law as shown in Equation (2.39) [13].

$$\begin{aligned} logh_{Ca} = log[\%Ca] - 0.072[\%Al] - 0.337[\%C] \\ +0.02[\%Cr] - 0.049[\%Ni] - 0.097[\%Si] \end{aligned} \qquad (2.39)$$

2.6.2 **Calcium Oxidation**

Calcium has a stronger affinity for oxygen than most of the elements [12]. Assuming that calcium oxide (CaO) exists as a separate phase and has an activity of one, calcium oxidation reaction as Equation (2.1) produces an equilibrium constant that can be written as:

$$logK_{Ca-O} = logh_{Ca} + logh_O \tag{2.40}$$

Assuming there is a strong two elements interaction, only first order interactions are significant. Equation (2.40) can be rewritten as follows:

$$\begin{gathered} logK_{Ca-O} = log[\%Ca] + log[\%O] \\ +e_{Ca}^{Ca}[\%Ca] + e_{Ca}^{O}[\%O] + e_{O}^{Ca}[\%Ca] + e_{O}^{O}[\%O] \end{gathered} \tag{2.41}$$

The Japan Society for Promotion of Science (JSPS) recommended values for interaction coefficient e as listed in Table 2.6 [79].

Table 2.6 Interaction coefficient of Ca, O and S [79]

j \ i	Ca	O	S
Ca	-0.002	-1290	-140
O	-515	-0.17	-0.133
S	-110	-0.27	-0.046

Applying values from Table 2.6 to Equation (2.41) and remove the low impact self-interaction terms, the equilibrium constant of calcium oxidation reaction can be simplified as shown in Equation (2.42):

$$logK_{Ca-O} = log[\%Ca] + log[\%O] - 1290[\%O] - 515[\%Ca] \qquad (2.42)$$

There is still a debate on the free energy ΔG° of Ca-O equilibrium. The reported values vary based on the experimental approach chosen [80]. Some of the free energy equations determined from previous studies and corresponding ΔG° values at 1600°C are listed in Table 2.7 [76].

Table 2.7 Thermodynamic data of Ca-CaO equilibrium

ΔG^o as a function of temperature (J/mol)	ΔG° at 1600°C (J/mol)	Reference
491187.15 - 146.42T	246942.49	[10]
566257 - 146.41T	292031.07	[81]
645200 - 148.7T	366684.90	[82]
138222.33 + 63.02T	256258.79	[83]

2.6.3 **Formation of Calcium Aluminate**

A binary phase diagram of CaO-Al_2O_3 system is shown in Figure 2.9 [65]. There are five thermodynamically stable stoichiometric combinations of alumina Al_2O_3 and CaO, including CA_6, CA_2, CA, $C_{12}A_7$ and C_3A, where C and A denote calcia and alumina respectively. The exact reaction for formation of calcium aluminates remains debatable. The two general reactions used are (2.43) and (2.44) [74,84,85].

$$x[Ca] + \left(1 - \frac{2}{3}x\right) Al_2O_3 = (CaO)_x \cdot (Al_2O_3)_{1-x} + \frac{2}{3}x[Al] \quad (2.43)$$

$$xCaO + yAl_2O_3 = xCaO \cdot yAl_2O_3 \quad (2.44)$$

The melting point of C_3A, $C_{12}A_7$, CA are below or close to the typical steelmaking temperatures hence these inclusions most likely form fully liquid or semi-liquid calcium aluminate inclusions [1]. CA_2 and CA_6 in almost all cases remain as solid phase, and they are reported that they cause nozzle clogging [73,86]. It should be noted that the ultimate goal of calcium treatment is not to modify solid inclusions into completely liquid inclusions. As long as there is a liquid phase formed on the surface of a solid inclusion and the formation of this phase can be wetted by the liquid steel or slag, the modification process is successful, and the probability of inclusions deposited on nozzle walls will be significantly lowered [10].

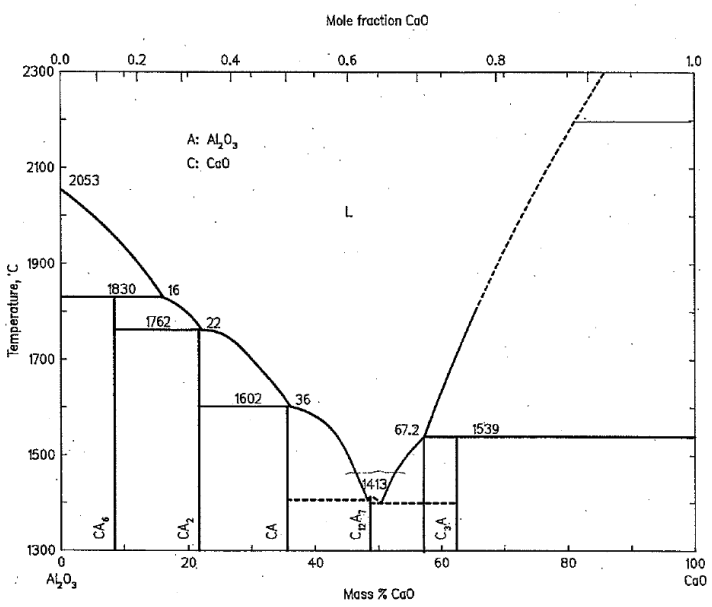

Figure 2.9 CaO-Al_2O_3 phase diagram [65]

It is difficult to modify all alumina inclusions to low melting point calcium aluminates due to the kinetics reasons such as insufficient modification time and low calcium recovery. In fact, EDS analysis results from the ArcelorMittal Dofasco Hamilton facility indicated the existence of all types of calcium aluminates in calcium treated steel [87].

Previous researchers [88–90] suggested that multiple phases are formed around an alumina inclusion during modification process with Ca addition. A schematic diagram of the formation of multiple phases surrounding an alumina inclusion is given in Figure 2.10 [88]. Dissolved calcium diffuses towards the centre of alumina inclusion during the treatment. Calcium concentration gradually decreases from steel-inclusion interface to the core of the inclusion due to slow calcium diffusion in the solid inclusion. The outer layer of alumina has high calcium concentration to form greatly modified calcium aluminates (CAx-liq and CA) with a low liquidus temperature. The degree of modification is lower close to the core,

being unmodified (Al_2O_3) or insufficiently modified (CA_2 and CA_6). The rate of modification therefore largely depends on the rate of calcium transfer in the inclusion [91]. Formation of liquid calcium aluminate inclusions require steady state calcium supply and sufficient modification time. These conditions are very unlikely can always be satisfied in real refining processes.

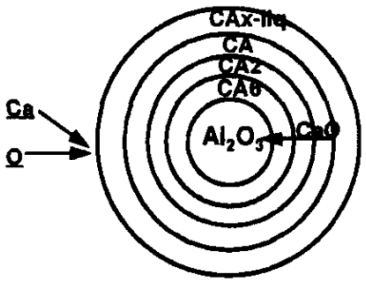

Figure 2.10 Schematic diagram of a layered calcium aluminate inclusion [88]

2.6.4 **Thermodynamic Limitation of Calcium Treatment**

There is a competition between calcium oxidation and sulfurization during steel refining process. Sulfur may either consume dissolved calcium or CaO or react with calcium aluminates to form CaS (Equation (2.45), (2.46)) [76,92]. Consequently, liquid calcium aluminate inclusions may convert to solid CA_6, CA_2 inclusions ($x \neq 0$, $y \neq 0$ in Equation (2.46)) or unmodified alumina inclusions ($x = 1$, $y = 0$ in Equation (2.46)). In both cases CaS, causes nozzle clogging as Al_2O_3 inclusions [92].

$$[Ca] + [S] = CaS \tag{2.45}$$

$$\frac{3-2y}{3x-3y}(CaO)_x(Al_2O_3)_{1-x}+\frac{2}{3}[Al]+[S] = \frac{3-2x}{3x-3y}(CaO)_y(Al_2O_3)_{1-y}+CaS \quad (2.46)$$

CA and CaS are assumed to be individual substance hence have unit activity. In the case of $C_{12}A_7$ (x ≈ 0.63, y ≈ 0.37 in Equation (2.46)) been reversed to CA, which has higher alumina content, when there is excess sulfur, the equilibrium constant K of Equation (2.46) is written as Equation (2.47).

$$K=\frac{{a_{CA}}^{33/5}\cdot {a_{CaS}}^{3}}{{a_{C_{12}A_7}}^{4/5}\cdot [h_{Al}]^2[h_S]^3}=\frac{1}{[h_{Al}]^2[h_S]^3} \quad (2.47)$$

According to Equation (2.47), the formation of CaS depends on the activity of dissolved Al and S in the melt. When K value is lower than the equilibrium constant of Equation (2.46), the formation of CaS becomes possible. Choudhary and Ghosh [93] compared the thermodynamic prediction of CaS formation and experimental data available in the literature [94]. The phase stability of CaS with respect to dissolved Al and S in liquid steel as well as temperature is represented in Figure 2.11. Two curves in Figure 2.11 represent the combination of [Al] and [S] required to reach the equilibrium of Equation (2.46) at 1500°C and 1600°C. Coordinates located to the right of the curve represents the potential formation of CaS at the corresponding temperature. The equilibrium curve in Figure 2.11 shifts outward as temperature increases from 1500°C to 1600°C. This findings indicates the combinations of [Al] and [S] that CaS can form at 1500°C may not trigger CaS formation at 1600°C if the coordinates are located below 1600°C equilibrium curve. This finding based on thermodynamic calculations was also experimentally confirmed by Y.

Ren et al. [89]. In their study, CaS particles were found in liquid steel containing 0.041 wt% [Al] and 0.003 wt% [S] at 1500°C after calcium injection.

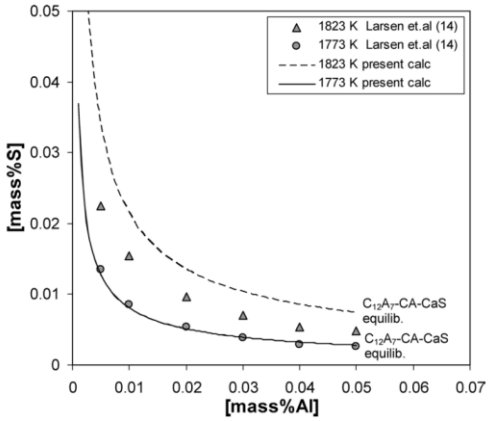

Figure 2.11 Phase stability of CaS with respect to dissolved aluminium and sulfur contents at 1773 and 1823 K [93]

Holappa et al. [80] compared the saturation limits for calcium aluminates saturation limit and calcium sulfide as shown in Figure 2.12. The allowed concentration range of Al and Ca for the formation of liquid inclusions is between two saturation curves, CaS-sat. and CaAl-sat. in Figure 2.12. The area in between is referred as the "liquid window". CaS precipitates if combinations of [Al] and [S] concentrations are above the liquid window, any combination below the liquid window means incomplete modification that forms high melting point calcium aluminates. They [80] suggested multiple CaAl-sat. curves are not needed as the effect of [S] is significant for CaS formation. CaS stable region expands when [S] increases, and the liquid window becomes smaller. When temperature increases, liquid windows at any [S] are larger. The liquid window is almost completely closed at 1550°C, when [Al] = 400 ppm. Thermodynamics determines at such combination of solutes Al and Ca in the system, it is almost impossible to form fully liquid inclusions. Therefore,

operating inside the liquid window is critical to prevent SEN clogging due to formation of excessive amount of solid inclusions.

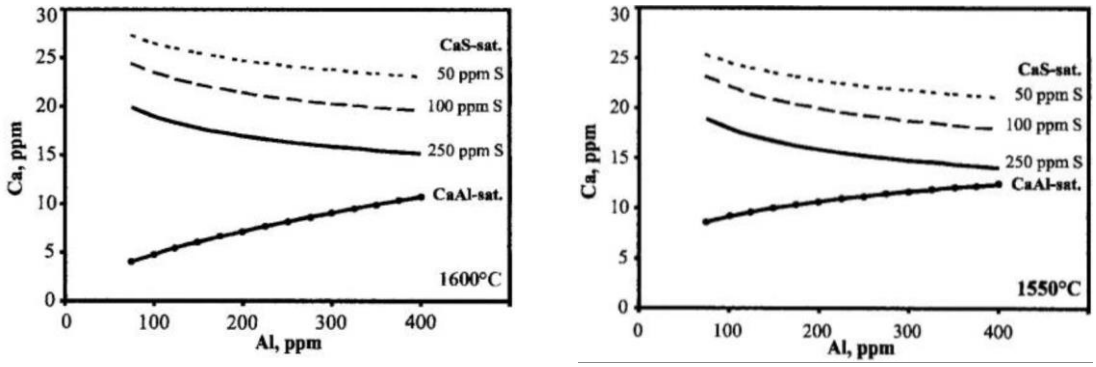

(a) (b)

Figure 2.12 Saturation limits for calcium aluminate, CaS and liquid windows at different S level at (a) 1600°C (b) 1550°C [80]

Ren and co-workers [89] characterized transient evolution behaviour of inclusions in linepipe steel production during calcium treatment. It has been found that the inclusion composition trajectory mainly depends on the sulfur content in the molten steel. Experiments were carried out using two steel grades containing 30 and 310 ppm sulfur concentration. Inclusions in low sulfur samples underwent transformation from pure Al_2O_3 to Al_2O_3-CaS (-CaO) then Al_2O_3-CaO (-CaS) and eventually completed the transformation of Al_2O_3-CaO. High sulfur samples went through similar modification process as the low sulfur grade, but complete modification from Al_2O_3 to liquid calcium aluminates was not observed. CaS population remains high even 30 minutes after Ca addition. The extent of calcium modification in low sulfur steel is less likely of been over-treated compared to that with high sulfur content [95].

The similar morphology change was observed regardless of S level in the steel. Some typical inclusions from both sample types are presented in Figure (2.13) and Figure 2.14 [89]. Image 1 to 8 in Figure 2.13 (a) and Figure 2.14 (a) are 8 different inclusions found in the steel samples before calcium treatment. The images in (b) show 8 inclusions at 30 minutes after calcium was injected. Inclusions from both samples exhibited successful spheroidization after long holding time. Inclusions in low S sample contained virtually no CaS after 30 minutes of modification time, while about 10 wt% of CaS remained in high S steel sample.

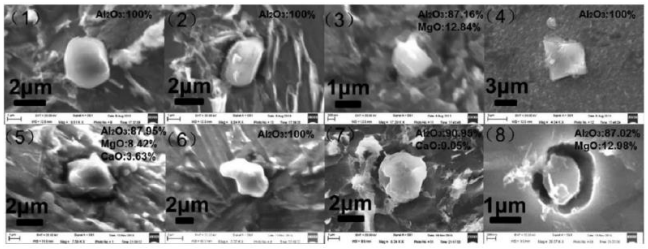

(a)

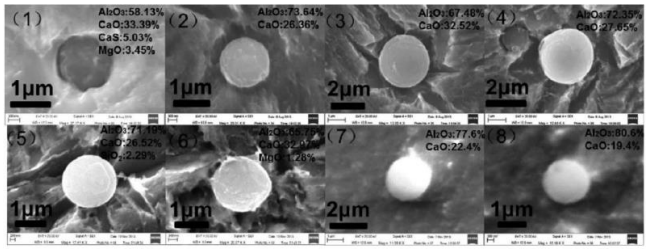

(b)

Figure 2.13 Morphology of inclusions detected in steel containing 30 ppm S (a) before Ca treatment (b) 30 min after Ca treatment [89]

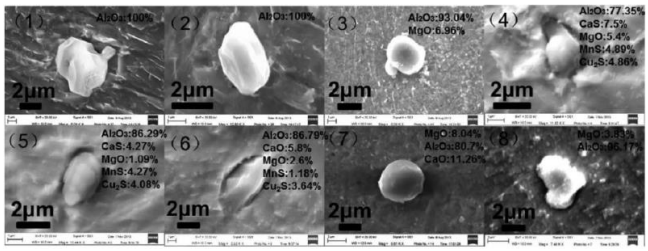

(a)

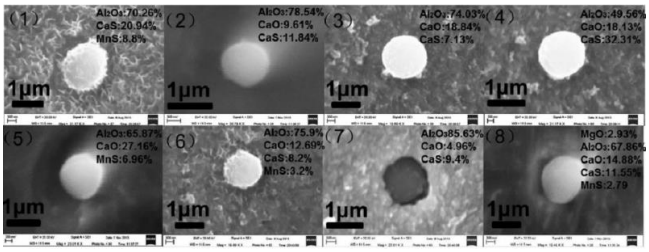

(b)

Figure 2.14 Morphology of inclusions detected in steel containing 300 ppm S (a) before Ca treatment (b) 30 min after Ca treatment [89]

In both grades, CaO was the dominant calcium containing phase, but the number of CaS inclusions increases as sulfur content increases. Based on this observation, researchers concluded that there are multiple types of CaS such as transient CaS formed at the early stage of treatment and stable CaS when steel is over-treated [89]. In the system with low S concentration, S in CaS can be replaced with O to reach equilibrium in Reaction (2.48), resulting in a decrease in the number of CaS inclusions, so is said to be transient. This finding has also been supported by other researchers [96–98].

$$3CaS + Al_2O_3 = 3(CaO) + 2[Al] + 3[S] \quad (2.48)$$

It is suggested that CaS co-exists with other inclusions in three different forms. CaS can either attach to another inclusion, evenly distribute inside other inclusions or wrap around inclusions like a ring [91].CaS rings are the most commonly observed type [73,80,93,99,100].

Kang et al. [46] claimed that attachment of CaS to another inclusion occurs very likely due to inclusion agglomeration. Yang et al. [91] suggested that CaS can disperse evenly inside calcium aluminate inclusions and this occurs because liquid calcium aluminates are essentially $CaO\text{-}Al_2O_3$ binary slag which has certain level of sulfur capacity to dissolve CaS. As temperature decreases, CaS concentration inside calcium aluminate inclusions exceeds its saturation and CaS precipitates out evenly [91]. If the cooling rate is not fast enough to lock sulfide in calcium aluminates, sulfur can diffuse out to form superficial layers with calcium rejected from liquid steel, resulting inclusion will have CaS ring surrounding the core inclusion [73].

2.7 Gaps in Knowledge and Objectives

The nature and quantity of the inclusions formed in steel are critical in steelmaking, affecting both the productivity due to clogging, and quality of the steel produced. Understanding and controlling how the inclusions can be removed efficiently is crucial to optimizing the operating conditions of steel refining units and improving end product quality. This area has attracted much attention. Several studies have been done on the dissolution side of inclusion removal, on some of the commonly encountered inclusions. However, to the best of our knowledge, there is no study on the dissolution of calcium aluminate inclusions.

Given the industrial importance of inclusion removal in steelmaking and calcium injection as one of the most commonly applied refining techniques, further study on the removability of solid calcium aluminates inclusions is required to fill the gaps in our knowledge.

The dissolution mechanism must be understood first in order to control process parameters for efficient inclusion removal. As the first study on calcium aluminate dissolution, the investigation on the sample preparation and proper experimental approaches are required to conduct successful experiments and generate reliable experimental data.

The objective of the present study is to develop a fundamental understanding of the removal of calcium aluminate inclusions during refining of liquid steel. The dissolution behaviour of inclusions at different temperature and slag composition is studied. The ultimate target is to accelerate dissolution and increase the degree of completion of inclusion removal. Last but not the least, refining of existing model or invention of new dissolution model will be attempted if the existing models do not successfully predict the dissolution process.

Chapter 3 Experimental Apparatus and Methodology

The dissolution kinetics and mechanism of CA_2 inclusions are determined for a range of temperature, slag compositions and inclusion morphology. Deliberate variations in the slag compositions are made to represent changes in steel refining process conditions.

The experimental temperature is varied between 1500° and 1600°C, a range appropriate to ladle steelmaking and expected to influence the inclusions dissolution kinetics. The experiments are conducted using particles with a diameter range of 96-417 μm. The inclusion diameter is selected based on the limitation of resolution. The phase boundary between particle and slag is not clear when a particle diameter is reduced to 30 μm. Even though the size range studied does not represent the inclusions detected in various steel types, the data collected on dissolution rate related to various slag composition can assist steelmakers to optimize refining operations. The CSLM equipment permits images of particles dissolved in slag to be recorded and the change of particle area with time is obtained using image analysis software.

Development of knowledge on the dissolution behaviour of inclusions in a slag and how these affect the dissolution kinetics and mechanism is an original contribution to our understanding of inclusion removal in ladle metallurgy. The experimental methodology can be divided into the following phases:

1. Materials Preparation, including production and design of synthetic inclusions and slag.
2. In-situ inclusion dissolution observation using the CSLM.

3. Investigation of reaction product layer between particle and slag after dissolution experiments.

3.1 Materials Preparation

3.1.1 Slag Design and Preparation

There are few considerations to be made while designing slag composition. The slag must be transparent to laser light; its composition is chosen to ensure that it has low crystallization temperature and high viscosity. Under such conditions, it is possible to follow the motion of the inclusion and maintain focus inside the liquid slag. Steelmaking slags mainly contain CaO, Al_2O_3, SiO_2, MgO, FeO, MnO and CaF_2. Because the CSLM technique precludes using slags containing transition oxides such as FeO and CrOx, slag compositions will be based on ladle type/tundish slags such as the CaO-SiO_2-Al_2O_3 system. Although some researchers [69] reported that they were able to observe interaction between inclusions and slag containing up to 9.19 wt% FeO, it will be difficult to distinguish inclusions from such slag, and inclusions are completely invisible if they sink deeply into the slag based on author's experiences.

Present study considers two slag compositions with different SiO_2 contents. The high SiO_2 content slag is referred as slag 1 (S1) and the low SiO_2 slag is slag 2 (S2). Both slags have liquidus temperatures below the experimental temperatures so good fluidity is ensured during the dissolution experiments. Slag 1 has been selected because the composition is relevant to industry and studied by previous researchers [6,38]. Slag 1 composition was used previously by Monaghan et al. [38,64] to investigate the dissolution rate of Al_2O_3 and

$MgAl_2O_4$ in tundish type slags. The comparison of dissolution time between partially modified and unmodified inclusions is possible. Slag 2 has lower SiO_2 content and slag 2 composition is close to ladle type slag composition. The purpose of introducing slag 2 is to study the effect of SiO_2 content on the dissolution kinetics of calcium aluminate particles.

The high purity laboratory grade $CaCO_3$, SiO_2 and Al_2O_3 powders were purchased from Sigma Aldrich. Details of raw materials are listed in Table 3.1. To prepare the slag, high purity oxide powders of appropriate proportions were initially mixed and then heated to a temperature, 50°C higher than the slag liquidus temperature, to fully melt in a platinum crucible. After homogenization of molten slag, slags were quenched and crushed. This process was repeated twice to ensure slag homogeneity. The compositions of resultant slags are confirmed with inductively coupled plasma optical emission spectrometry (ICP-OES) measurements as listed in Table 3.2.

Table 3.1 Properties of inclusion and slag making materials

Materials	Purity (wt%)	Size (μm)	Supplier
Al_2O_3	99.5	≤10	Sigma Aldrich
$CaCO_3$	99.95-100.05	-	Sigma Aldrich
SiO2	99.5%	≤44 (325 mesh)	Sigma Aldrich

Table 3.2 ICP results of studied slag compositions

Slag	CaO (wt%)	Al_2O_3 (wt%)	SiO_2 (wt%)	C/A	Liquidus (°C)
1	30.5 ± 0.3	23.2 ± 0.3	46.3 ± 0.6	1.3	1445
2	56.11 ± 0.2	38.6 ± 0.1	5.3 ± 0.1	1.5	1428

The slags were then hand crushed to very fine powder, in order to minimize the number of gas bubbles trapped. Approximately 0.1 g of crushed slag powder was compacted into a platinum crucible (10 mm OD x 5 mm height). Then slags were melted again in a vertical furnace at a temperature above its liquidus temperature to be used in the dissolution experiments. At elevated temperature, vacuum degassing was also applied in order to reduce the gas bubbles entrapped in molten slag.

Vacuum pump is capable of reducing pressure inside furnace to about 0.25 atm. Two cycles of vacuuming and Ar gas back filling are found to be sufficient to remove most of the gas bubbles. Figure 3.1 compares the images of slag and gas bubbles in the platinum crucibles with and without vacuuming. The circular black areas are the gas bubbles and the ring-like structure in the background is the bottom of the Pt crucible. Some gas bubbles remain after vacuuming, but both the volume and number density of bubbles decrease drastically after vacuuming. The remaining gas bubbles are assumed to have no effect on experiments if the gas bubbles do not contact the particles during experiments.

Certain number of experiments can be conducted using same slag. The exact number of experiments depends on the amount of particle dissolving in slag in each experiment. The principle is slag should be discarded if any constituent shift 1 wt% away from its initial composition. The discarded slag is removed from Pt crucible by dissolving in concentrated HF. Normally it takes 5 days to dissolve about 0.1 g slag.

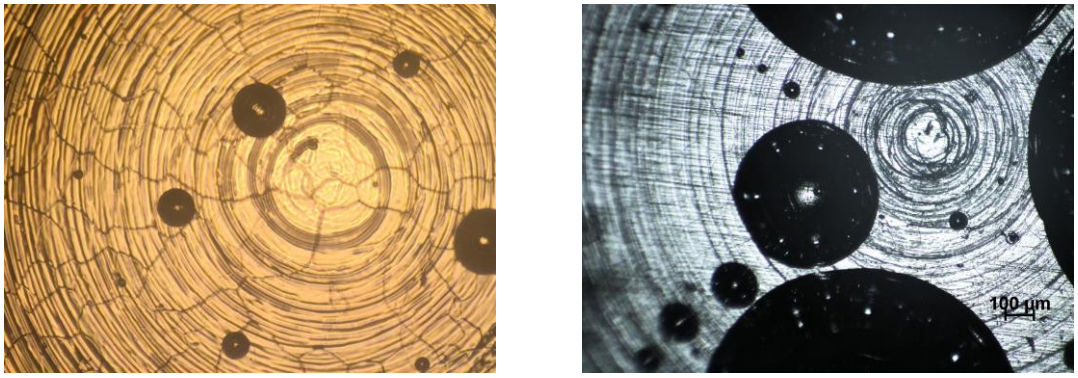

(a) (b)

Figure 3.1 Images of transparent slag and gas bubbles in Pt crucible x50 magnification (a) with vacuuming (b) without vacuuming

In some low silica content slag, crystalline phases precipitate out during slag solidification, as shown in Figure 3.2. The inhomogeneity of slag may create error when determining the slag chemistry using ICP-OES. In that case, slags are hand ground into fine powder and physically mix to produce representative samples of the slag chemistry.

Figure 3.2 Solidified slag with precipitates on the surface

3.1.2 **Synthetic Inclusion Production**

Many of the inclusion types formed during steelmaking process are not available to purchase. This limits the assessment and testing of key inclusion groups important in steelmaking. It is crucial to produce these inclusions under controlled conditions in order to provide firm base for an experimental study.

The sintering technique to produce high purity calcium dialuminate particles ($CaO \cdot 2Al_2O_3$) were adapted from literature [101,102]. Mass fraction of CaO and Al_2O_3 in CA_2 can be calculated from stoichiometry, theoretical mass fraction and actual weighted mass for both CA_2 as shown in Table 3.3. 33 wt% $CaCO_3$ and 67 wt% Al_2O_3 powders were mixed using a ball mill for an hour to avoid segregation. A slurry was then made by pouring mixed oxide powders into 500 ml deionized water. The slurry was vacuum filtrated with a Buchner funnel and Waterman #6 filter papers with 3 μm diameter meshes or any equivalents. Particles remained on filter papers were kept at 80°C for 24 hours to remove moisture. Roughly 4 wt% distilled water was added as a binder to the dry oxide powders retrieved from filter papers.

Table 3.3 The weight fraction of calculated and weighted powder

	Calculation (wt%)		Weight (g)	
Materials Product	$CaCO_3$	Al_2O_3	$CaCO_3$	Al_2O_3
CA_2	32.89	67.11	21.433 (32.89 wt%)	43.738 (67.11 wt%)

About 7 to 10 g of mixed powder was pressed under 200 MPa to produce 2.5 cm diameter pellets. The pellets were placed in an alumina crucible and sintered in a muffle furnace. The temperature was initially increased from room temperature to 900°C with a heating

rate of 10°C/min and the furnace temperature was held at this value for one hour since $CaCO_3$ decomposes to CaO and CO_2 between 600 and 1000°C [103]. Followed by 24 hours sintering at 1400°C, the furnace was then cooled to room temperature. After cooling, pellets were crushed into powder and pelletized again. This sintering process was repeated to ensure chemical homogeneity of the CA_2 particles. The CA_2 phase was confirmed by X-ray diffraction (XRD) as provided in Figure 3.3. No other phases were identified via XRD.

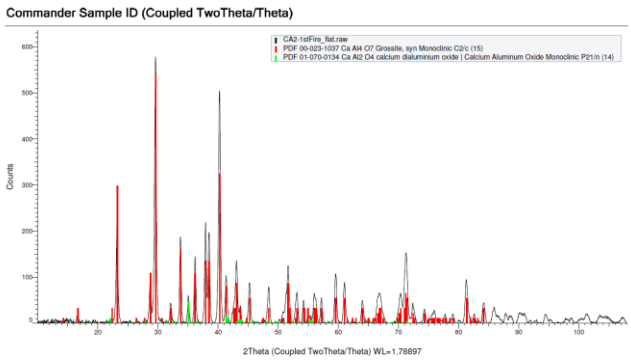

Figure 3.3 XRD results of CA_2 particles sintered at 1400°C

Even though CA_2 particles were successfully produced at 1400°C, the porosity of the particles was high. Further sintering and arc melting approaches were tested to reduce the porosity in this study.

The effects of sintering time and temperature on the porosity of the particles are studied. Firstly, the sintering time was increased from 24 hours to 144 hours at 1400°C. Then sintering temperature increased from 1400°C to 1600°C and was held at 1600°C for 48 hours. Few experiments conducted to test the reactivity of particles with slag. It has been found that there were less gas bubbles evolved when the CA_2 particles, which were sintered at 1600°C, were used. Further, particles that are sintered at 1600°C don't break up during

experiments. A schematic drawing of the thermal cycle for the proposed sintering process to produce high purity dense CA_2 particles is shown in Figure 3.4. The first three sintering steps show insignificant impact on reducing particle porosity, and it was confirmed by XRD that the mixed oxide powder will be transformed to CA_2 within 24 h holding at 1400°C. In conclusion, the first and last steps are only required to produce high purity dense CA_2 particles.

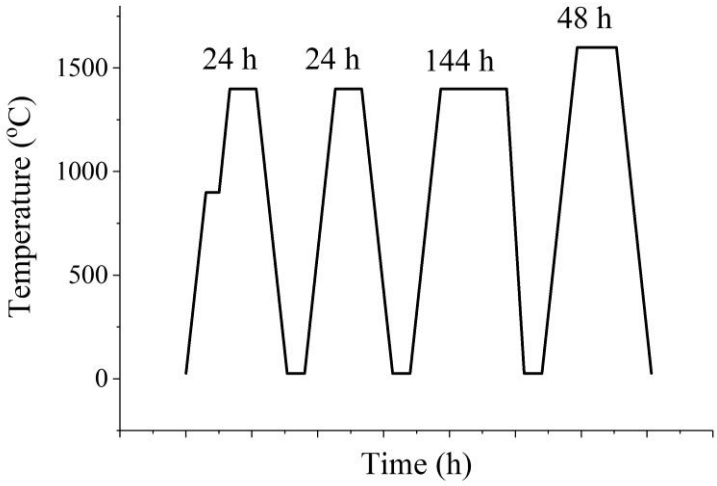

Figure 3.4 Schematic drawing of thermal cycle for sintering process to produce high purity dense CA_2 particles

Secondly, CA_2 particles sintered at 1400°C were placed on a water cooled Cu mould and melted by electric arc. High temperatures using arc is expected to melt the calcium aluminate particles then solidify to produce dense particles. Details of the arc melting operations vary from equipment to equipment and will not be included here. Kezhuan Gu helped the author to melt the CA_2 particles under defined operating conditions. One concern using electric arc is potential contamination such as W from welding head and Cu from the mould.

The particles used for dissolution experiments are fragments obtained after breaking sintered or melted CA_2 particles.

3.1.3 Pycnometric Measurements of CA_2 Inclusions

The density of inclusion was measured using a 2 ml pycnometer. Pieces of inclusions were placed in the pycnometer and then filled with isopropyl. The pycnometric measurement recorded the mass of pycnometer, pycnometer with isopropyl, pycnometer with isopropyl and inclusions, pycnometer with inclusions as m_1, m_2, m_3, m_4 respectively. The relative density of inclusion to isopropyl can be calculated using Equation (3.1), then can be easily converted to density of CA_2. The density of isopropyl is equal to 780 kg/m^3 at room temperature [104]. Ten measurements were made in total for both CA_2 particles produced by sintering and arc melting to provide a 95% confidence value of density. All the results for density measurements are listed in Table 3.4. It is believed that the variation in density of CA_2 produced using two methods is strongly related to the particle porosity. The calculations suggest that the sintered CA_2 particle has about 3 vol.% porosity. Based on an assumption that particles are isotropic, the density of sintered particle and arc melted particle is corrected to 2709 and 2788 kg/m^3 at experimental temperatures [105]. The difference between densities of both types of inclusions at maximum and minimum experimental temperatures are less than 2 kg/m^3. Hence identical density value of 2709 (sintered) and 2788 (arc melted) kg/m^3 will be used in this study at all experimental temperatures.

$$\rho'_{CA_2} = \frac{m_2 - m_1}{(m_2 - m_1) - (m_3 - m_4)} \cdot \rho'_{C_3H_8O} \tag{3.1}$$

Density of the CA_2 particle at high temperature was corrected for expansion at experimental temperatures using Equation (3.2) [106].

$$\rho' = \frac{\rho'_0}{1 + 3\alpha_L} \tag{3.2}$$

where ρ_0 and α_L denote density at room temperature and linear thermal expansion coefficient respectively. The density of both sintered and melted particles were measured and the results are provided in section. The phase morphology of both sintered and melted particles is examined by SEM and the results are summarized in section 4.1.

Table 3.4 List of density measurements of CA_2 particles using pycnometer at room temperature

Measurement	m_1	m_2	m_3	m_4	Density ratio	CA_2 density (kg/m^3)	Average density at RT with 95% confidence (kg/m^3)
Sinter-1	6.1867	6.5529	7.9813	7.7167	3.6043	2811.378	2761 ±89
Sinter-2	6.1921	6.5621	7.9749	7.7175	3.2860	2563.055	
Sinter-3	6.1886	6.5539	7.9776	7.7143	3.5814	2793.471	
Sinter-4	6.1901	6.556	7.9777	7.7146	3.5593	2776.284	
Sinter-5	6.1887	6.555	7.9762	7.7157	3.4622	2700.51	
Sinter-6	6.1912	6.5568	7.9777	7.7163	3.5086	2736.737	
Sinter-7	6.1879	6.5542	7.9777	7.7168	3.4753	2710.759	
Sinter-8	6.1888	6.5567	7.9777	7.7144	3.5172	2743.423	
Sinter-9	6.1903	6.555	7.98	7.7152	3.6507	2847.508	
Sinter-10	6.1911	6.5533	7.9778	7.716	3.6076	2813.904	
Melt-1	6.1839	6.3151	7.8095	7.7123	3.8588	3009.882	2841 ±208
Melt-2	6.1929	6.3224	7.8091	7.7107	4.1640	3247.91	
Melt-3	6.189	6.3215	7.8066	7.7118	3.5146	2741.379	
Melt-4	6.1951	6.3249	7.8052	7.7112	3.6257	2828.045	
Melt-5	6.1897	6.3194	7.8066	7.7118	3.7163	2898.739	
Melt-6	6.1911	6.3215	7.8066	7.7112	3.7257	2906.057	
Melt-7	6.1885	6.3177	7.8028	7.7109	3.4638	2701.769	
Melt-8	6.1897	6.3186	7.8016	7.7096	3.4932	2724.715	
Melt-9	6.1854	6.321	7.8058	7.709	3.4948	2725.979	
Melt-10	6.1915	6.3206	7.8031	7.7088	3.7098	2893.621	

3.2 CSLM Dissolution Experimental Set-up

The in situ observation for dissolution of particles in slag is carried out using CSLM system as shown in Figure 3.5. A particle-slag sample is placed inside the heating. At the bottom of the chamber there is a halogen lamp used as a heating element and extra light source. Using laser with a wavelength of 405 nm as a light source further enhances the resolution significantly. A feature with size of a 0.5μm can be resolved. Light source travels through a piece of silica glass for imaging of the phenomena inside the chamber. There is a gas purification system beside the CSLM to clean the dust and moisture in the gas system. The required purity of Ar gas is 99.999%. A programmable temperature controller is provided and supports rapid heating and cooling rates up to 1000°C/min with a maximum temperature of 1700°C.

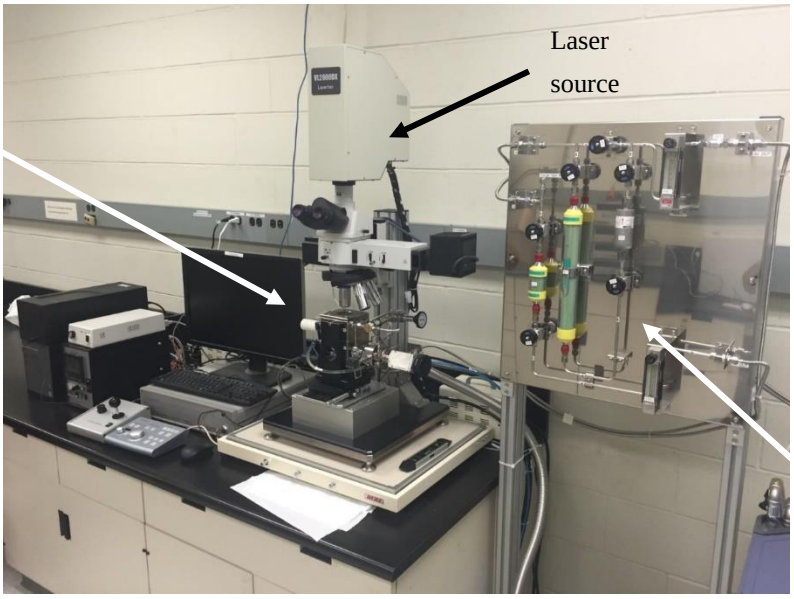

Figure 3.5 The CSLM and the auxiliaries

The schematic diagram of the experimental setup inside the heating chamber is illustrated in Figure 3.6 [107]. The temperature was measured using B type thermocouple, attached to the bottom of the crucible holder. A single CA_2 particle was placed on the surface of the pre-molten slag in a platinum crucible. The particle, sample holder and crucible were heated to the experimental temperature under high purity Ar atmosphere at 20-30 ml/min flow rate. Once slag was liquid, the inclusion completely immersed into the slag before experimental temperatures were reached. In this study, time zero is the moment designated when experimental temperature was reached. The experiments were repeated three times at each temperature to confirm reproducibility [107].

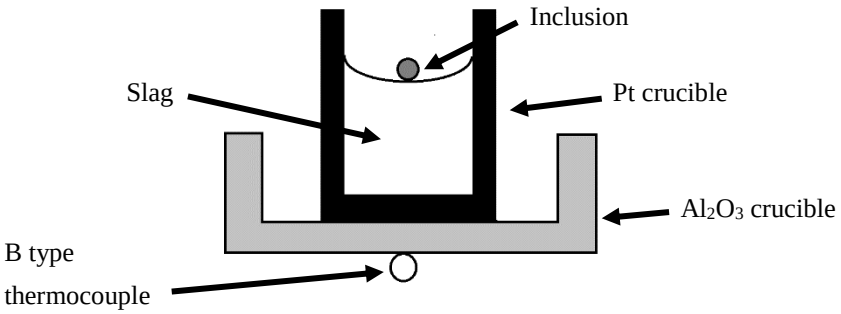

Figure 3.6 CSLM dissolution experiments setup [107]

Figure 3.7 provides the thermal cycle of dissolution experiments. The chamber was heated to 1000°C at the rate of 100°C/min, then the temperature was elevated to experimental temperature using a heating rate of 100°C/min. It was held at experimental temperature during the dissolution process and cooled to room temperature with a cooling rate of 150°C/min. Pure Fe (purity >99.9%) was used to calibrate the surface temperature of a sample. The thickness of Fe chip was 1 mm. The thermocouple temperature at the melting point of pure Fe was compared with theoretical value of 1538°C, which was considered as the actual surface temperature of the sample. The calibration data are tabulated in Table

3.5. Measurements precision increased significantly with temperature. Temperatures vary 8°C at the melting point of Fe. It is also important to remember that thermocouples have its own associated error. B type thermocouple used in present study is known to have about ±0.5% of the temperature error (±8°C) at 1600°C [108]. It was found that the surface temperature of the sample is 63 ± 5°C higher than that of thermocouple temperature when pure Fe was melted. This temperature difference was considered throughout this work [107].

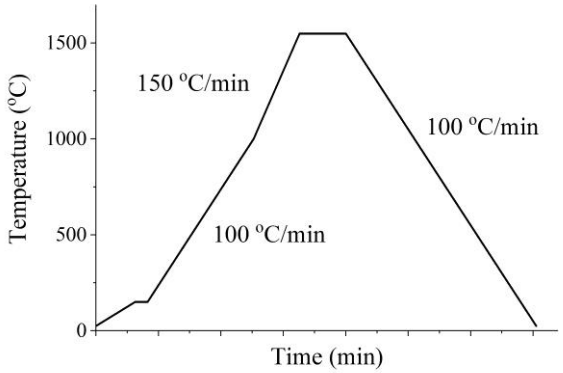

Figure 3.7 Schematic diagram of thermal cycle used for inclusion dissolution experiments [107]

Table 3.5 Comparison of measured temperatures and theoretical values for Fe phase transformation (°C)

Phase transformation	Calibration (°C)			Average (°C)	Theoretical value (°C)	Difference (°C)
	1	2	3			
α to γ	851	845	763	820	912	-92
γ to δ	1333	1333	1309	1325	1394	-69
δ to liquid	1480	1473	1472	1475	1538	-63

3.3 Investigation of Reaction Product Layer between Slag and Particle

Further dissolution experiments were conducted using vertical tube furnace to investigate the formation of product layer between slag 1 and CA_2 particle at 1500°C. The predictions and observation of a product layer will be discussed in details in the following section. The set-up and procedure of this experiment are focussed here. A schematic diagram of the experimental setup is shown in Figure 3.8. Slag was first melted in a graphite crucible at 50°C higher than the liquidus temperature of the corresponding slag to ensure homogeneity. Later slag is cooled and removed from the furnace and graphite crucible. Two CA_2 particles with a diameter of about 1 mm were placed inside the crucible and slag was positioned on top of the particles. Slag should not be sticking to the crucible walls so it can be easily removed. The slag and particle placed in the graphite crucible was then heated in the tube furnace. The crucible was raised gradually with the support of an alumina tube from the bottom to the furnace hot zone after experimental temperature is reached in the hot zone. Holding time at the hot zone depends on the size of the inclusion, especially when experiments are conducted at 1500°C. If a small particle is used, it is practically impossible to locate the particle or it can completely dissolve before cooling the slag-particle system. Therefore, the decision on holding time largely depends on the operator's experience and no algorithm is developed for calculating the optimum experimental time. In the present study, holding time was decided to be a minute. Sample was quenched by lowering the crucible to the bottom of vertical tube furnace. The crucible takes about 30 min to reach room temperature, but the high temperature interactions were believed to be preserved once slag is solid. The furnace was purged with high purity Ar gas until quenching is finished to prevent the consumption of the graphite crucible. Based on this experimental procedure, the particles remained at the bottom of the crucible. The holding time was appropriate. Slag

can then be cross sectioned or directly observed under scanning electron microscope (SEM) to identify the phases. The results of this investigation are provided in section 4.6.

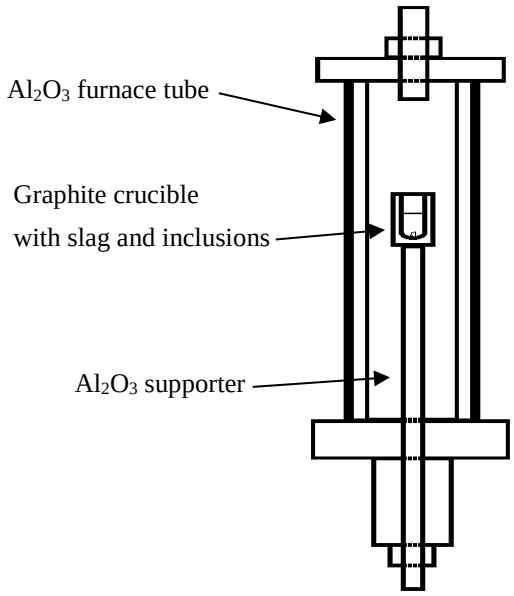

Figure 3.8 Schematic diagram of the dissolution experiments in the vertical tube furnace

Chapter 4 Experimental Result and Discussion

4.1 The Effect of Preparation Techniques on Morphology of CA_2 Inclusions

As high purity dense CA_2 particles are not available in the market, it is necessary to establish a production technique to produce CA_2 particles with high purity for dissolution experiments using CSLM. As explain in section 3.1.2, two different production techniques, sintering and arc melting, were used and the morphology of the particles was compared. Figure 4.1 (a) and (b) show the overview back scatter images of a whole CA_2 particle that is produced by sintering and arc melting using a scanning electron microscope (SEM) at low magnification. The large pieces in the centre are the particles and surrounding part is the Ni paint which supresses the effect of electron charging. During observation, low vacuum mode was used and hence only back scatter images (BSE) were available. Important topographical information can still be obtained using BSE images. In Figure 4.1, the most apparent difference between the CA_2 particles is the porosity. In Figure 4.1 (a), it can be clearly seen that consistently dispersed holes can be found on the surface of the particle. On the other hand, the surface of a CA_2 particle that is produced by arc melting appears to be free of pores at low magnification. Similar results were also seen at a higher magnification.

The surface of the arc melted CA_2 particle remains porous-free and is rather flat as seen in Figure 4.1 (d), whereas the sintered CA_2 particle, seen in Figure 4.1 (c), has a rough surface. It should be noted that there is a strong bonding between sintered particles and these particles will not easily detach from the bulk during the dissolution process. This is

important to collect continuous data and minimize any error during the interpretation of data. Pore diameters vary between 5 and 15 μm as shown in.Figure 4.1 (c).

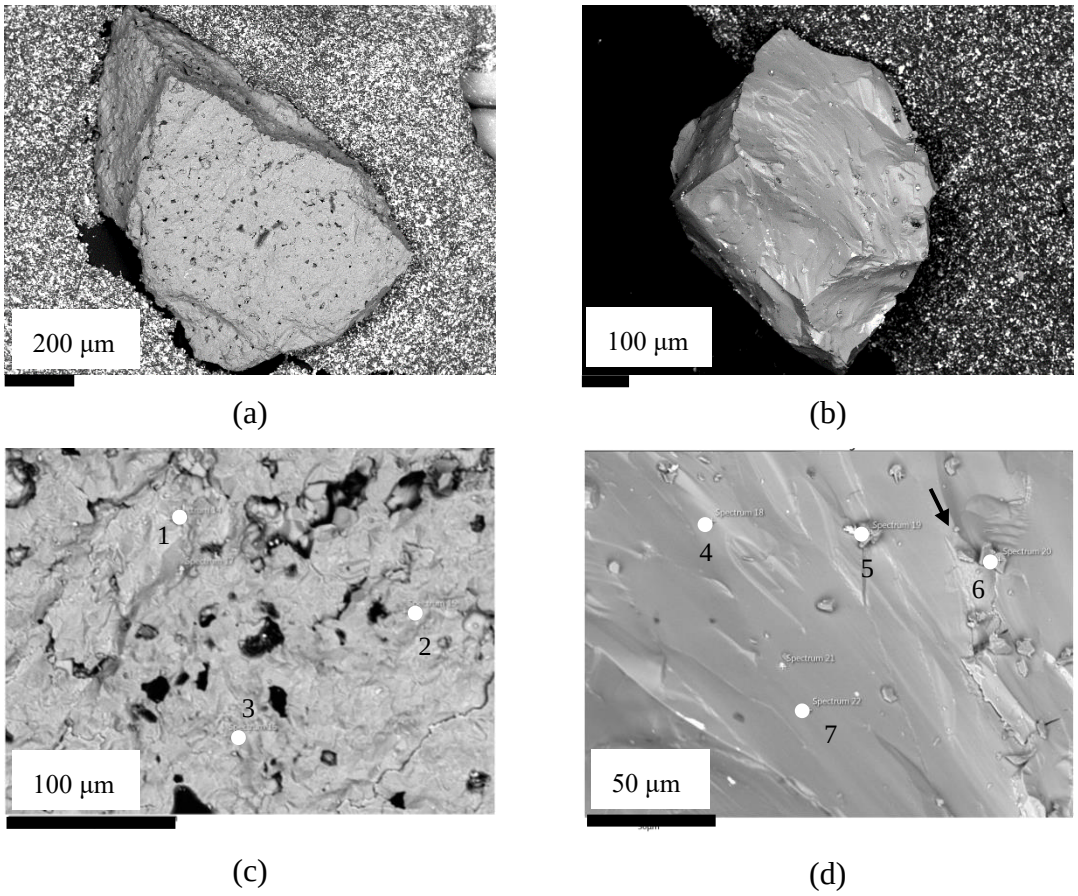

Figure 4.1 BSE images of CA_2 particles (a) sintered at 1600°C (x80) (b) melted in an arc furnace (x120) (c) sintered at 1600°C (x450) (d) melted in an arc furnace (x650)

The energy dispersive spectroscopy (EDS) results of numbered points and the overall analysis of the area in Figure 4.1 (c) and (d) are listed in Table 4.1. Both sintered and arc melted CA_2 particles are considered to be chemically homogenous since the EDS results in Table 4.1 show that there is good consistency in each sample.

Table 4.1 EDS results of numbered locations in Figure 4.1

Inclusion type	Location	Al (wt%)	Ca (wt%)	O (wt%)	C (wt%)
Sintered CA_2	1	35.4	12.4	39.7	10.0
	2	35.8	13.9	36.4	11.0
	3	34.4	13.2	40.0	9.8
	Overall	34.1	12.7	37.7	12.6
Arc melted CA_2	4	32.3	12.3	34.9	17.9
	5	34.6	15.8	41.5	15.8
	6	35.1	9.7	20.9	29.4
	7	31.8	12.9	30.5	21.2
	Overall	31.5	12.7	32.5	19.8

The important difference between sintered and arc melted particles is porosity. The presence of pores can either accelerate or decelerate the dissolution depending on if slag can enter pores to increase slag-particle contact surface. It is known that the dissolution rate largely depends on the available reaction sites. If slag can enter the pores, porous particles have a higher surface area to react with slag compared to dense inclusions. Analysis based on the dissolution of porous particles may overestimate the kinetics.

4.2 The Effect of the Inclusion Preparation Method on CSLM Dissolution Experiments

CSLM experiments were conducted to study the effect of particle preparation methods on the dissolution rates of particles in slag 2 at 1550°C. It has been found that both sintered and arc melted CA_2 particles tend to float on the slag and they are not fully covered by the

slag during experiments. Introducing these periods when the particles are floating will create some errors during the interpretation of experimental data. Figure 4.2 illustrates the images of floating particles that are obtained from recorded dissolution experiments. The pieces in the centre are particles, which can be distinguished from the slag in the background. The white lines represent the slag-inclusion boundary. In Figure 4.2 (a) (d) (e), it is clear that parts of the CA_2 islands are not covered by the slag for a long time after reaching the experimental temperature, regardless of the preparation technique. The parts of the particles that are in direct contact with Ar can be recognized by the laser reflection, indicated by the arrow marks. The strong reflection occurs as a result of the curvature differences on the slag surface close to and far from a CA_2 particle.

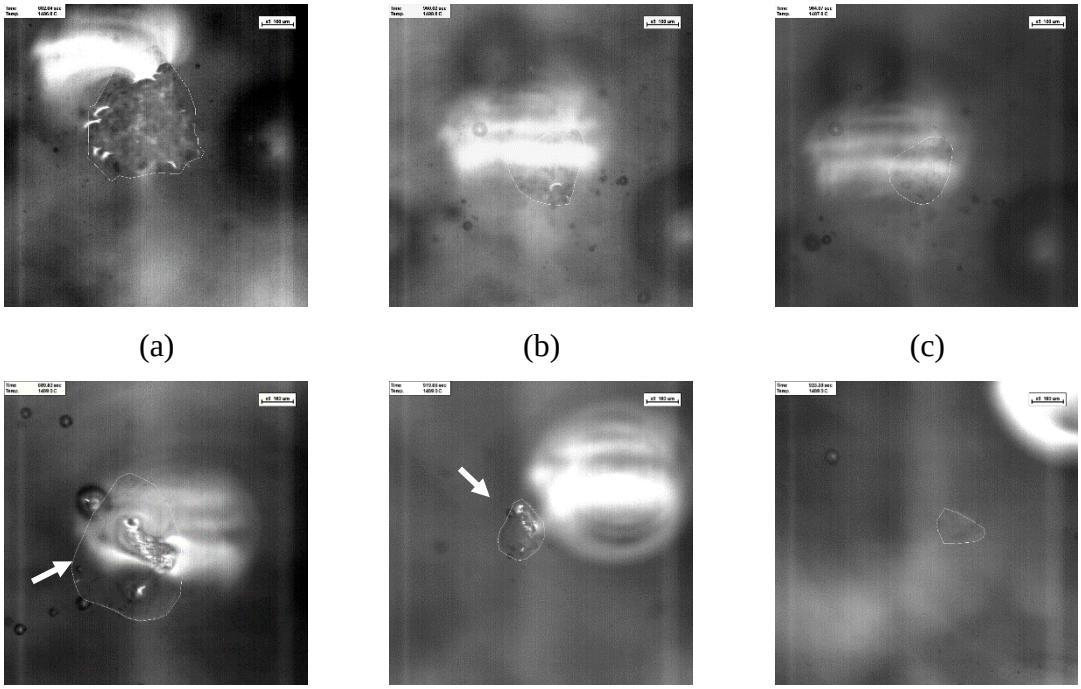

(a) (b) (c)

(d) (e) (f)

Figure 4.2 Images of the sintered CA_2 particle (a) 0 s (b) 68 s (c) 85.2 s and arc melted CA_2 particle (d) 0 s (e) 30 s (f) 34 s after reaching the experimental temperature of 1550°C in slag 2

Whether the CA_2 particle floats on the slag surface or is fully immersed is critical to the experiment, as time zero is defined to be the moment when the particle is fully immersed and the experimental temperature is reached. Table 4.2 lists the time before and after CA_2 particle is immersed during the dissolution process at 1550°C. Figure 4.3 shows the dissolution curve of each experiment using sintered and melted particles, after the temperature reach 1550°C. It has been shown that the sintered CA_2 particles require longer time to completely dissolve compared to the arc melted particles. Furthermore, the dissolution time for arc melted CA_2 particles was less than 15 s, while the sintered CA_2 particles took at least 50 s to dissolve. Porosity affects the roughness of the surface and the actual density of the CA_2 particles. This can be related the time required for inclusion to

fully immerse into the slag. Dense particles sink faster than porous particles of the same volume because the latter experience less gravitational force to balance the friction force and inertia force [36]. This may explain the relatively shorter time required for arc melted particles to be immersed as shown in Table 4.3.

The dissolution time for arc melted CA_2 inclusions are too short to generate representative experimental data. Hence, sintered CA_2 particles are preferred in dissolution experiments. It is worth mentioning that the sintered CA_2 particles were fully immersed in all slag 1 experiments before the experimental temperatures were reached. Sintering was also used in other studies [52,57,101,109] as the preparation technique, so the data that is generated using sintered CA_2 is also expected to be representative for dissolution studies.

Table 4.2 Time before and after inclusions fully immersed at 1550°C in slag 2

Inclusion type	Equivalent radius of a particle after fully immersed (μm)	Time before particle is fully immersed after reaching experimental temperature (s)	Time after particle is fully immersed after reaching experimental temperature (s)
Sintered CA_2	150	0	190
	109	80	52
	101	79	50
Melted CA_2	63	31	13
	24	48	4
	7	72	2

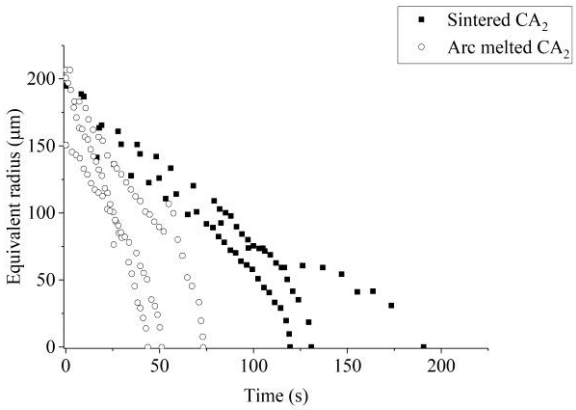

Figure 4.3 The dissolution process of the CA_2 particles in slag 2 after reaching 1550°C. This dissolution process included the floating time of particles before they fully immersed

The slag infiltration time was calculated in order to further understand the different dissolution behaviours of sintered and arc melted particles. Infiltration of slag into pores depends on the capillary force F_σ, friction force F_μ and gravitational force F_g [36]. The force balance is written as seen in Equation (4.1) [36]. If slag enters pores from the bottom, the downward gravitational force and friction force counter capillary force pushes liquid slag upwards. h_2 is the maximum height of slag in a pore when $F_g = F_\sigma$. The mathematical expression of h_2 is given as Equation (4.2) [36]. Rewriting Equation (4.1) using expression of the individual forces, gives Equation (4.3), which can be integrated to Equation (4.4) with an initial condition (x, t) = (0, 0). The depth of slag penetration in pores x of known diameter d can be written as a function of time t [36]. If slag infiltrates particles from the sides, $F_g = 0$, and the depth of slag penetration is calculated using Equation (4.5) [36].

$$F_\sigma = F_\mu + F_g \tag{4.1}$$

$$h_2 = \frac{4\sigma_{ls}\cos\theta}{dg\rho'} \tag{4.2}$$

$$d\sigma_{ls}\cos\theta - \frac{8}{\varepsilon}\eta x\frac{dx}{dt} - \frac{d^2}{4}g\rho' x = 0 \tag{4.3}$$

$$-\ln\left(1-\frac{x}{h_2}\right) - \frac{x}{h_2} = \frac{d^2 g\rho'\varepsilon}{32\eta}t \tag{4.4}$$

$$x = \sqrt{\frac{d\sigma_{ls}\cos\theta\,\varepsilon t}{4\eta}} \tag{4.5}$$

where θ and ε denote the slag-inclusion contact angle in the pore and labyrinth factor respectively. ρ_l, η and σ_{ls} represent the slag density, dynamic viscosity and interfacial tension, respectively. The labyrinth factor is introduced to quantify the difference between diffusion coefficients in a dense and porous matrix [36]. There is a disagreement on the specific mathematical correlations between the labyrinth factor, effective diffusion coefficient and the true diffusion coefficients [110–112]. Measuring ε is complicated, the labyrinth factor is calculated using Equation (4.6) for simplicity [112]. φ is the porosity which was measured to be about 3 vol%, so ε = 0.009. The porosity was calculated based on the difference between the densities of sintered and arc melted CA_2 particles. It is assumed that arc melted particles have 0 vol% porosity. The slag-inclusion contact angle θ of CA_2 is assumed to be the same as that of CA in a similar condition, which is 20° [113]. It is assumed that the slag-inclusion interfacial tension (σ_{ls}) follows the Young's relation in Equation (4.7) [113,114], depending on particle-gas surface tension σ_{sg} and slag-gas surface tension σ_{lg},.

$$\varepsilon = \varphi^2 \tag{4.6}$$

$$\sigma_{ls} = \sigma_{sg} - \left(\sigma_{lg} cos\theta\right) \tag{4.7}$$

Slag 1 and slag 2 have a density and interfacial tension of 2691 kg/m^3, 469 mN/m and 2785 kg/m^3, 163 mN/m at 1550°C respectively [65]. The initial pore diameter is assumed to be 15 μm based on the SEM images that were obtained in this work. Equation (4.2) yields an equilibrium height h'' = 4.46 m for slag 1 and 1.50 m for slag 2. h'' can then be applied to Equation (4.4) and the time required for the slag to enter a pore with a known diameter is calculated. For example according to Equation (4.4), slag 1 takes 0.2 s from the bottom and 1 s from the side in order to penetrate 15 μm into a pore that has a 15 μm diameter. On the other hand, slag 2 takes 0.14 s to enter from the bottom and 0.21 to enter from the side of a pore. Since the time needed to enter 15 μm into the pores is very short, it is safe to conclude that slag 1 and slag 2 will be able to fill most of the pores. Therefore, the actual surface area of sintered CA_2 particles that is in contact with slag, is higher than a dense arc melted CA_2 that has the same equivalent radius. This conclusion indicates that an increase in contact area due to porosity cannot explain the slow dissolution rates of sintered CA_2 particles in slag 2. Further studies are needed to provide solid conclusions.

4.3 Observation of CSLM Dissolution Experiments

Since it has been shown in the previous section that the sintered CA_2 particle has a longer time in slag during dissolution experiments, the following results and discussion are based on experiments using the sintered CA_2 particles.

All of the experiments were captured using a charge couple device (CCD) camera that was positioned above the sample. Hence, only particle projection on the horizontal plane was captured. The oxide particle was distinguished from the slag based on the contrast in each frame. In some cases, the contrast between the particle and slag was insignificant. The brightness and contrast of images was adjusted to obtain a clear boundary [107].

Figure 4.4 shows images of a sintered particle in slag 1 at 1550°C. The particle can be found in the centre of each image and the white lines represent the slag-inclusion interface. It is clear that the particle projection on the horizontal plane decreases over time.

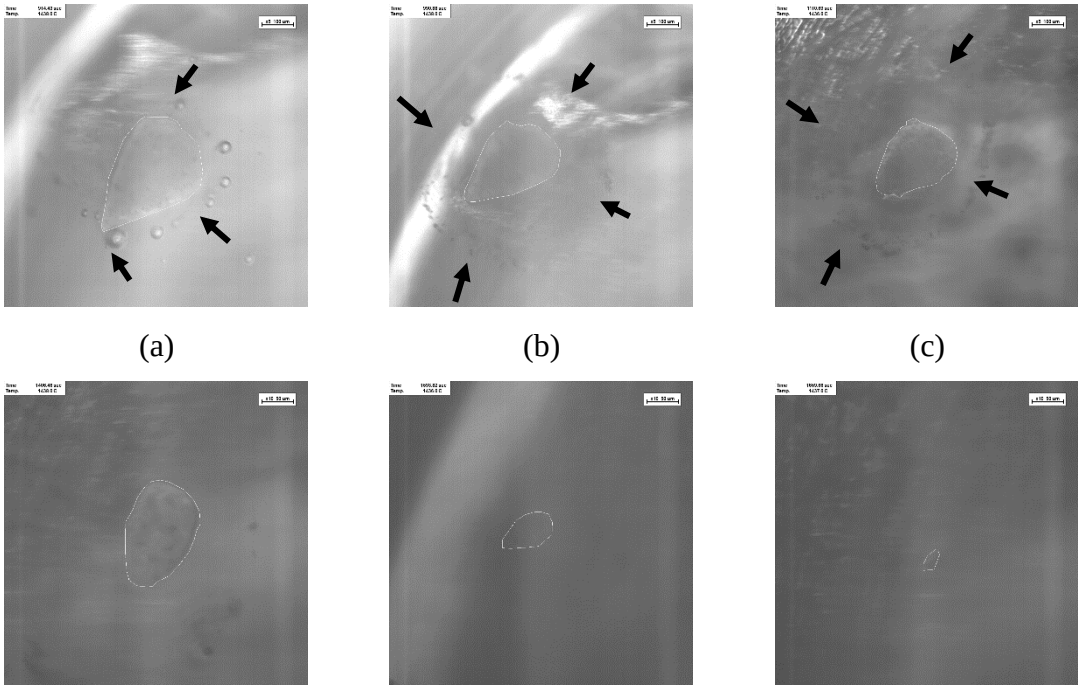

(a) (b) (c)

(d) (e) (f)

Figure 4.4 Images of the CA_2 particle dissolving in slag 1 at 1550°C

As shown in the SEM images in Figure 4.1, sintering cannot eliminate all the pores within the inclusion. Hence, there were gas bubbles that were released while the sintered inclusions dissolved. Some gas bubbles are highlighted using solid arrows in the Figure 4.4 (a). This image was taken in 4 s after time zero. Most bubbles have diameters that are less than 10 μm and they leave the slag-particle interface immediately. Gas bubbles are usually trapped in the slag. This probably occurs due to great friction force applied by the viscous slag. Further gas bubbles tend to stop at the same distance away from the inclusion and a ring of gas bubbles is formed as shown in Figure 4.4 (b) and (c). As the particle dissolves, the formation of gas bubbles slows down. The ring of gas bubbles cannot maintain its shape close to the end of dissolution since the evolution rate of gas is much lower than the escape rate of gas from the ring. This is shown in Figure 4.4 (d). Figure 4.4 (e) and (f) are taken towards the end of the dissolution before the particle completely disappeared. Inclusion maintained its original shape but all of the sharp edges seen in Figure 4.4 (a) are trimmed. The rounding phenomena reported on the dissolution of other oxides is not observed until the very end of CA_2 dissolution [5,115].

Particles move slowly in the slag and rarely rotate. The movement of particles is caused by the difference in surface tension in the slag, which is known as the Marangoni effect [7,92,115]. It can be seen that the actual shape of the sintered particles is far from spherical and it is very difficult to express the volume evolution of irregular particles using a single parameter that changes over time. In this work, the dissolving particles were assumed to be spherical for simplicity. The areas bounded by white lines were then measured using ImageJ. The equivalent radius of particles were calculated based on their projection on the horizontal plane [107].

4.4 **Thermodynamic Analysis** [107]

Both temperature and slag composition have important effects on the dissolution rate of CA_2 through changes in the driving force. To understand this better, the stable phases that were present in the $CaO\text{-}SiO_2\text{-}Al_2O_3$ slag system at 1500°C, 1550°C and 1600°C were calculated using FactSage™. The predictions are illustrated in Figure 4.5 (a), (b)and (c) respectively [107]. All of the relevant phases are marked with numbers and they are listed in Table 4.3 [107]. Points A and B represent the initial composition of slag 1 (S1) and slag 2 (S2), respectively and they are both in the fully liquid region regardless of the temperature studied. The dashed line represents the expected changes in slag composition at the slag-particle interface. It should be noted that experiments with slag 2 at 1500°C were not conducted because slag 2 was not fully liquid at that temperature.

The author believes that the mass transport is the rate limiting step at the temperature range that is studied. In the present study, AlO_x^{y-} from the dissolved CA_2 is assumed to be the rate controlling species. The author adapted a similar approach that was suggested by previous researchers [64] and this approach focusses on the dissolution kinetics of spinel inclusions. The Ca^{2+} cation is smaller than the AlO_x^{y-} anions, and it does not require to break bonds before changing position. It has also been reported that the diffusion coefficients of AlO_x^{y-} and Ca^{2+} in slag containing $40CaO\text{-}20Al_2O_3$-40 wt% SiO_2 at 1550°C were 3.44×10^{-11} m^2/s and 5.11×10^{-10} m^2/s [65]. Therefore AlO_x^{y-} diffuses slower and becomes the rate controlling species. It accumulates at the slag-inclusion interface. Consequently, the trajectory of slag composition follows the dashed line that is seen in Figure 4.5. For simplicity, AlO_x^{y-} and Ca^{2+} are referred to as Al_2O_3 and CaO respectively in the following text.

At 1500°C, the phase diagram in Figure 4.5 (a) predicts the formation of the solid $CaO{\cdot}Al_2O_3{\cdot}2SiO_2$ (CAS_2) phase when the slag is assumed to be in local equilibrium with inclusion at the interface. Based on the phase diagram in Figure 4.5 (a), CAS_2 in direct local equilibrium with CA_2 is not a thermodynamically favourable situation. There exists no phase such as "CAS_2 + CA_2", and some intermediate phase formation would normally be expected to form between CAS_2 and CA_2 at equilibrium. However, since diffusion in the solid is generally slow, the time required to reach equilibrium will most likely be longer than the total dissolution time. If local equilibrium cannot be reached at the solid-solid interface, no secondary reaction product will form. Secondly, even if any secondary reaction product forms, the amount will be insignificant. A study on CaO dissolution found the thickness of product layer is much larger for the phase that can reach local equilibrium with slag, which is CAS_2 in this case. The other product layer will be thin [58,59]. Based on the results from the CaO dissolution, the author expects that the thickness of the following reaction products if any, would be insignificant during CA_2 dissolution as well. This consideration needs to be studied further in the future. Lastly, the formation of any high Al_2O_3 activity phase is thermodynamically forbidden. In conclusion, thermodynamics can predict CAS_2 being in local equilibrium with CA_2 when dissolution occurs at 1500°C in slag 1.

Similar kinetics studies of other common non-metallic inclusions, at 1550°C and 1600°C, the driving force for CA_2 dissolution in slag 1 (Figure 4.5 (b), (c), point A) is quantified as the difference between the concentration of Al_2O_3 in initial slag and Al_2O_3 in saturated slag [5,6,39,64]. In slag that can directly reach local equilibrium with the inclusion, such as Al_2O_3, the Al_2O_3 saturated slag has compositions that correspond to a certain point on the slag-

Al_2O_3 phase boundary on Figure 4.5. However, for the dissolution of multi-component non-metallic inclusion, such as CA_2 in slag 1, it is important to understand that the local equilibrium will be reached before slag is saturated with Al_2O_3. According to the literature [65], the activity of Al_2O_3 in CA_2, Al_2O_3 and slag 1 is about 0.47, 1 and 0.001 respectively. In other words, the driving force for dissolution rate of CA_2 inclusions would be lower than that for Al_2O_3 inclusions in slag 1.

In the case of the dissolution of CA_2 in slag 2 at 1550°C, a reaction product of CA is likely to be formed. However, the presence of CA between slag 2 and CA_2 does not change the expected trend of decreasing Al_2O_3 activity from CA_2 to slag. It is known that CA can be partially liquid [98,100] and therefore, the product layer is most likely not dense enough to be an obstacle for diffusion. Diffusion through liquid part of CA is faster compared to diffusion in solid CA. This condition satisfies the criteria for modelling the dissolution process as controlled by diffusion in stagnant fluid. This will be discussed further in the following section.

At a slightly elevated temperature of 1600°C, it is thermodynamically favourable for slag 2 to reach local equilibrium with CA_2 and there will not be any reaction product. Once again, when CA_2 dissolves in slag 2 at 1600°C, it satisfies the criteria to use mass transfer models without applying additional assumptions.

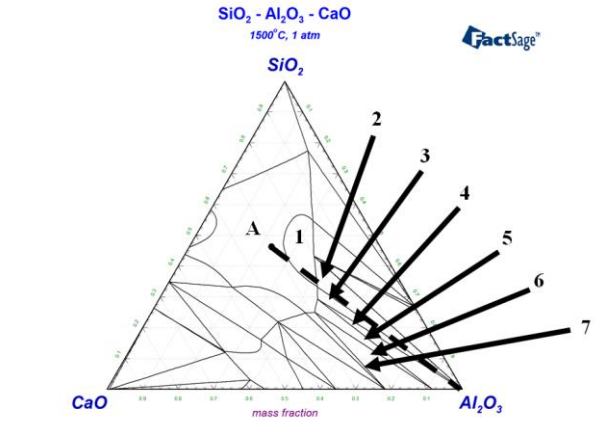

(a)

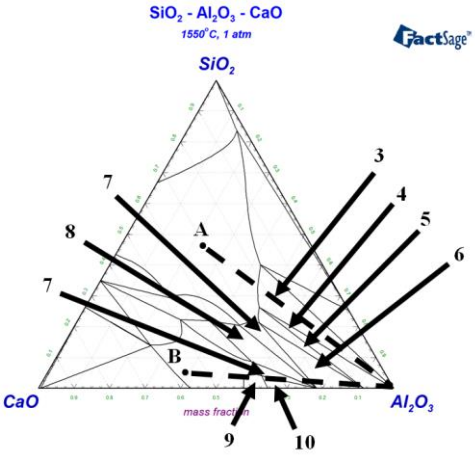

(b)

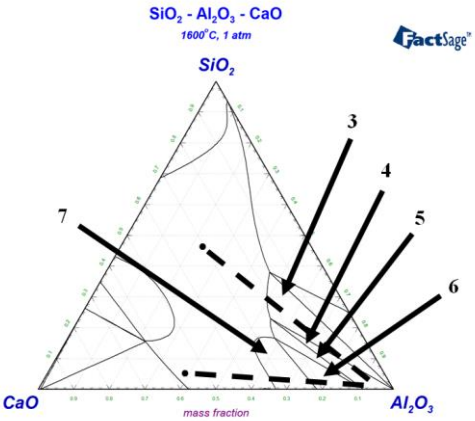

(c)

Figure 4.5 Prediction of stable phases using FactSage™ in slag 1 (A) and slag 2 (B) at (a) 1500°C (b) 1550°C (c) 1600°C [107]

Table 4.3 Explanation of numbered phases in Figure 4.5

1	Slag + $CaAl_2Si_2O_8$	2	Slag + Al_2O_3 + $CaAl_2Si_2O_8$
3	Slag + Al_2O_3	4	Slag + Al_2O_3 + $CaAl_{12}O_{19}$
5	Slag + $CaAl_{12}O_{19}$	6	Slag + $CaAl_4O_7$ + $CaAl_{12}O_{19}$
7	Slag + $CaAl_4O_7$	8	Slag + $CaAl_4O_7$ + $Ca_2Al_2SiO_7$
9	Slag + $CaAl_2O_3$ + $CaAl_4O_7$	10	Slag + $CaAl_2O_3$
A	Slag 1	B	Slag 2

4.5 CA_2 Dissolution Mechanisms [107]

In order to understand the dissolution process, it is important to establish the rate controlling mechanism of the dissolution reaction. The shrinking core model (SCM) and the diffusion in stagnant fluid model have both been applied to determine the dissolution mechanism of inclusions in the slag that is related to steelmaking conditions [3,6,37,39]. Details of the existing models that were used in this study can be found in the Literature Review. This study assumes that the chemical reactions are not a rate limiting step because the high temperature of steelmaking reactions favours high reaction rates. Thus, reaction kinetics is more likely to be controlled by the transport of elements from/to the phase interphase. Based on these models, three different rate controlling steps were considered (1) product layer diffusion SCM (2) boundary layer diffusion SCM and (3) diffusion in stagnant fluid [107]. In all modelling approaches, it is assumed that the particle has a spherical shape. The constant b is a stoichiometric constant of CA_2 that reacts with slag and b equals 1.

The dissolution mechanism can be determined by comparing the experimental results with the theoretical dissolution curves of each dissolution mechanism that are included in this study. The saturated concentration of Al_2O_3 in the investigated slag 1 was calculated using

FactSage™ version 7.0 with the database FToxid. The density of slag was calculated based on the molar volume of constituents and these calculations are provided in Appendix III. Figure 4.6 shows the normalized equivalent radius versus the normalized time for CA_2 particles that dissolve in slag 1 at 1500°C. The solid triangle and square marks represent two different dissolution experimental data types. The dashed line, dotted line and dashed-dot line all represent the dissolution mechanisms of the diffusion through product layer control, boundary layer diffusion control and diffusion in stagnant fluid control, respectively. It was found that the dissolution curve of CA_2 at 1500°C strongly agrees with the SCM that was developed for the diffusion through product layer. At the start of the dissolution process, a fast dissolution rate was observed due to a high concentration gradient. As the product layer forms and thickens and the unreacted core shrinks, the rate of diffusion slows down. Towards the end, the dissolution rate increases again as the volume of the particle becomes very small relative to the particle's surface. The author confirmed the formation of a product layer using the scanning electron microscope (SEM) technique. Details of this analysis will be discussed in Section 4.6.

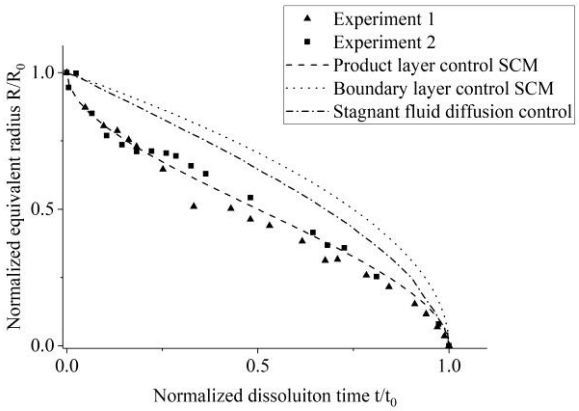

Figure 4.6 Normalized dissolution profiles of CA_2 particles in molten slag 1 at 1500°C

The dissolution profiles of the CA_2 particles dissolving in slag 1 at 1550°C and 1600°C were illustrated in Figure 4.7 and Figure 4.8, respectively. In both cases, the majority of experimental data agrees with the predictions of the diffusion in stagnant fluid control model. It should be noted that there is a slight difference in the predictions between the stagnant fluid control model and the boundary layer diffusion control SCM model. The boundary layer diffusion control SCM tends to underestimate the dissolution rate during the intermediate stage of the dissolution process. Towards the end of the dissolution process, as both models converge to the normalized equivalent radius of 1, the difference between the two models further decreases.

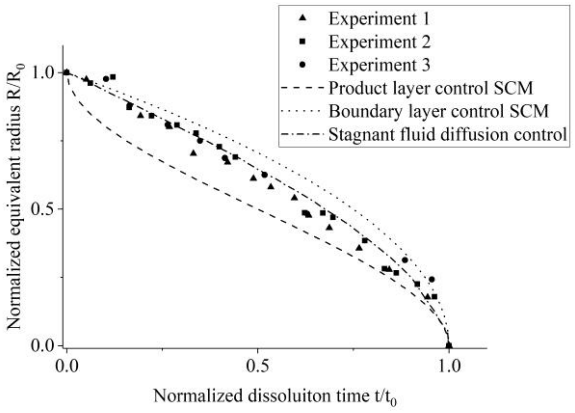

Figure 4.7 Normalized dissolution profiles of CA_2 particles in molten slag 1 at 1550°C

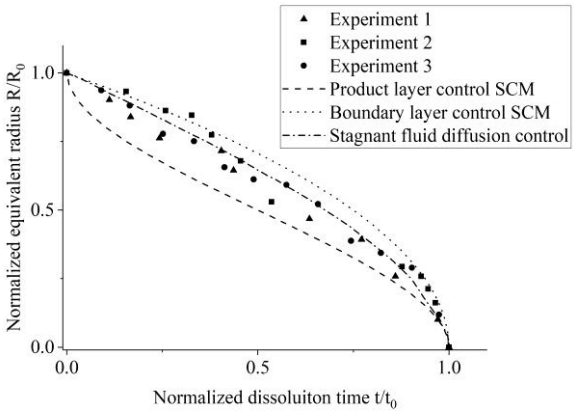

Figure 4.8 Normalized dissolution profiles of CA_2 particles in molten slag 1 at 1600°C

A comparison between the model predictions and experimental data for the dissolution rate of CA_2 particles in slag 2 at 1550°C and 1600°C is shown in Figure 4.9 and Figure 4.10, respectively. The diffusion in stagnant fluid control and boundary layer diffusion control SCM models can both predict well compared to the diffusion through product layer control model. It can be suggested that the dissolution of the CA_2 particle at 1550°C and 1600°C will be controlled by mass transport in the slag and both models are applicable. For the dissolution process, the author would favour the diffusion in stagnant fluid control model which yields a better result for the CA_2 dissolution compared to the boundary layer diffusion SCM. In fact, the difference between the theoretical model and experimental measurements was found to be insignificant. The author believes that the most important reason for this is that the boundary diffusion control SCM assumes a steady concentration gradient while the stagnant fluid diffusion model assumes that the concentration gradient changes over time during the dissolution process. The latter assumption is closer to the real dissolution process, when the slag is not infinitely viscous.

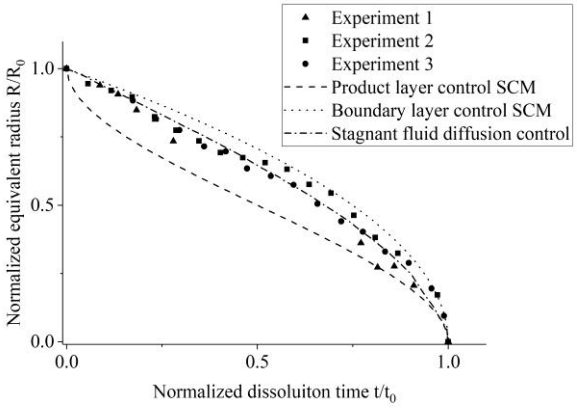

Figure 4.9 Normalized dissolution profiles of CA_2 particles in molten slag 2 at 1550°C

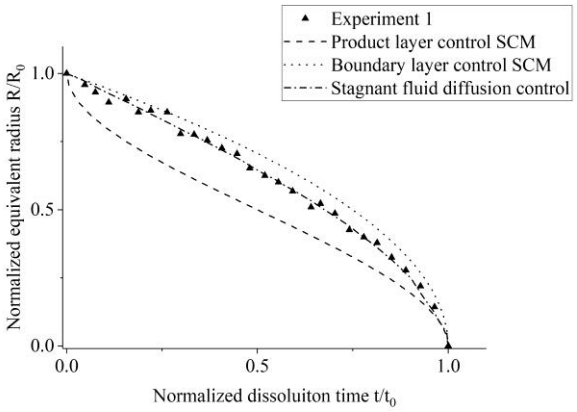

Figure 4.10 Normalized dissolution profile of CA_2 particles in molten slag 2 at 1600°C

4.6 **Confirmation of Dissolution Mechanisms**

The proposed dissolution mechanism was confirmed by conducting CA_2 dissolution experiments in the vertical tube furnace. Due to limited time, only a single experiment was conducted to confirm the product layer formation during the early stage of the dissolution process of the CA_2 particle into slag 1 (S1) at 1500°C. After the experiment, inclusions were detected at the surface of the solidified slag. The surface of the slag sample was

ground to expose the cross section and this was studied using SEM. Figure 4.11 illustrates the interface between the slag and particle that was taken from about 2 mm under the surface. The inclusion (1) can be distinguished from the contrast and porosity. The black spots that are dispersed on the surface are graphite particles from the graphite crucible. In Figure 4.11, the light grey area (3), that surrounds one side of the particle, is most likely the reaction product. The area marked with arrows in Figure 4.11 (a) represents the slag-reaction product interface. The EDS elemental mapping of the same area is provided in Figure 4.12 and a line scan across the particle-slag can be found in Figure 4.13.

There are clear concentration gradients of Al and Si detected in the proposed reaction product in Figure 4.13. Furthermore, there is no concentration gradient of Ca that was detected. This result supports the idea that the dissolution of CA_2 was controlled by diffusion in the reaction product in slag 1 at 1500°C and that the diffusion of CaO is much faster than the diffusion of Al_2O_3 in the system that was studied.

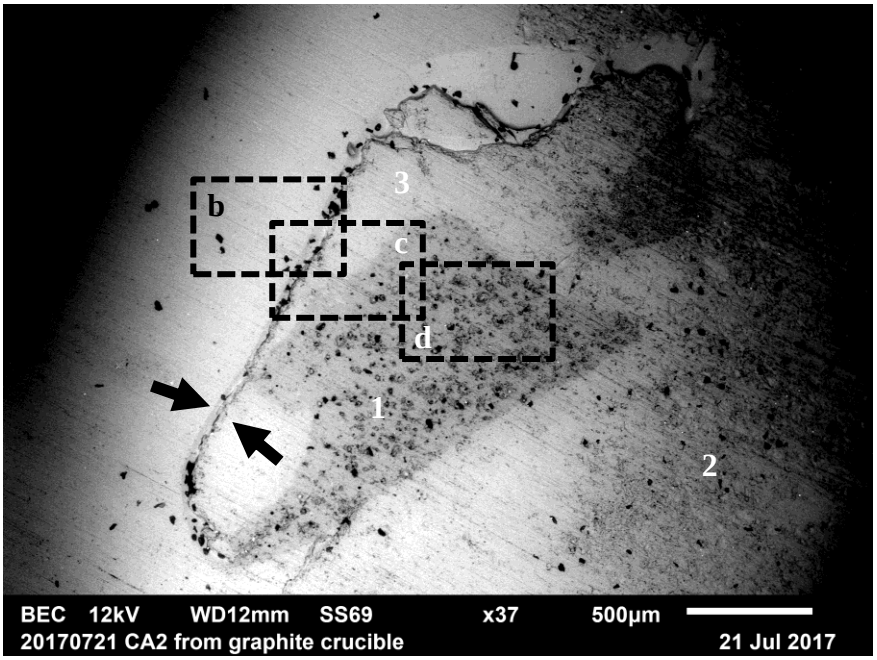

1: CA_2 particle

2: Slag

3: Reaction product

(a)

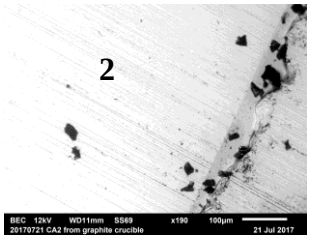

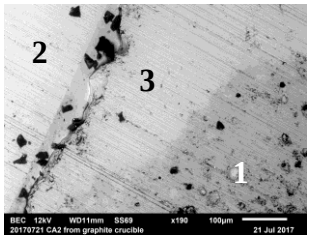

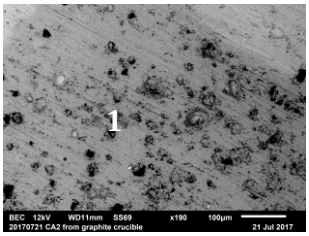

(b) (c) (d)

Figure 4.11 BSE images of areas around CA_2 particle detected at (a) x37 magnification (b) (c) (d) x190 magnification using SEM

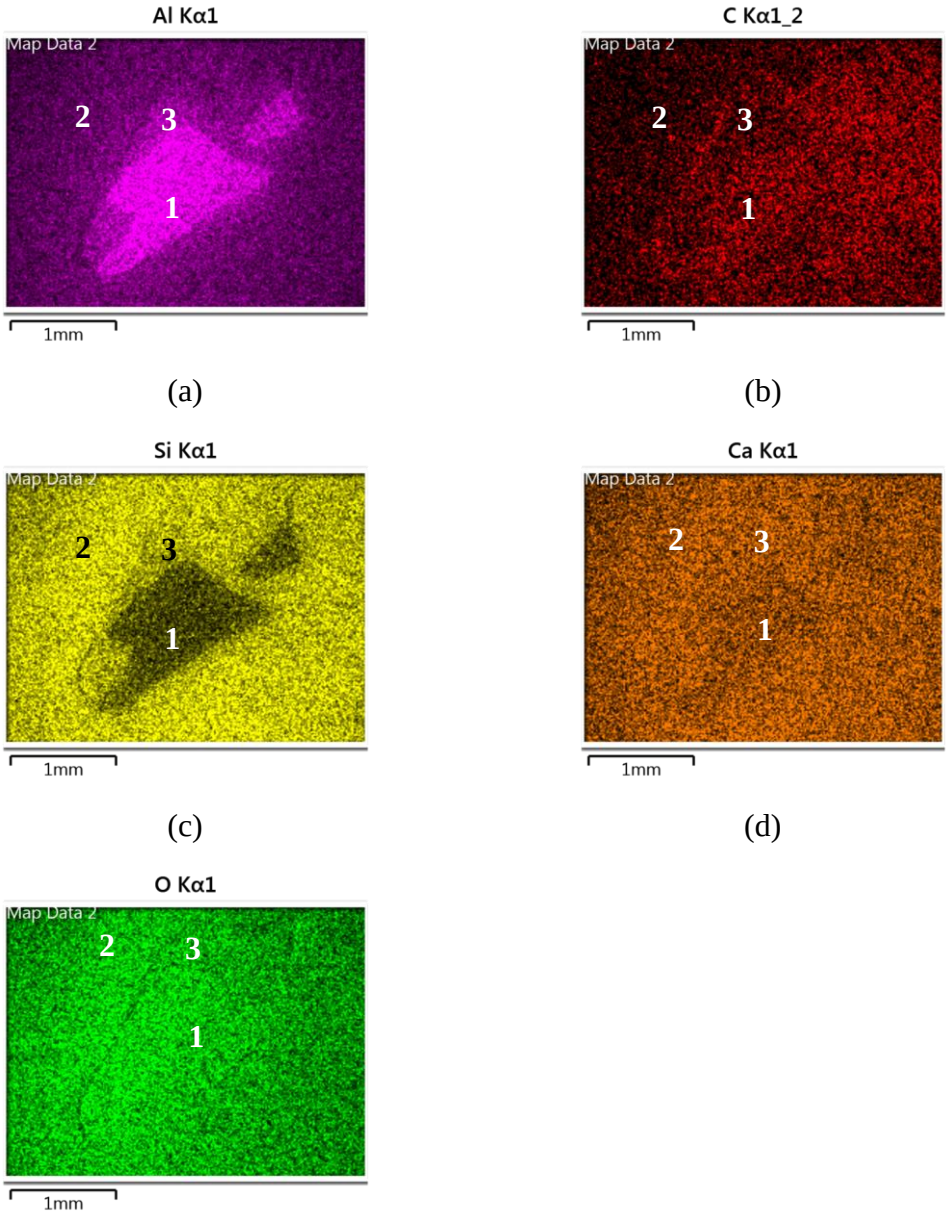

Figure 4.12 EDS elemental map of the particle and its surrounding area (a) Al (b) C (c) Si (d) Ca (e) O

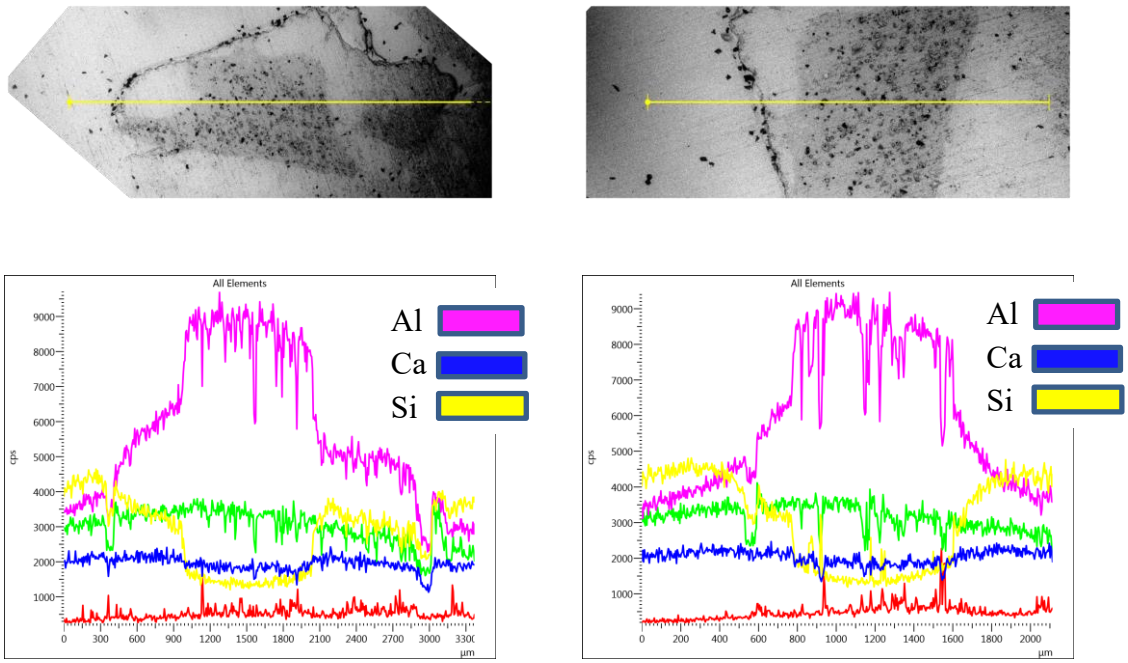

Figure 4.13 EDS line scans across the slag-particle

4.7 **The Effect of Temperature on Dissolution Kinetics**

The effect of temperature on the dissolution of CA_2 particles was studied by comparing the total dissolution time of inclusions with a similar equivalent radius in the slag 1 at three different temperatures: 1500°C, 1550°C and 1600°C. A comparison of the dissolution times is shown in Figure 4.14. The measured values for the equivalent radius of inclusions at time zero (R_0) were also provided in Figure 4.14.

The dissolution curves of experiments with 115 µm and 96 µm of CA_2 almost overlap the dissolution curve of 1600°C. A faster dissolution at a lower temperature compared to a higher temperature is generally not possible. The most probable reason is that the equivalent radius did not correctly estimate the inclusion volume for some of the irregular particles. Other than that, it is seen in Figure 4.14 that the slope of the equivalent radius-

time graph increases by increasing the temperature from 1500°C to 1550°C and then to 1600°C. This implies that the rate of dissolution increases as the temperature increases. This finding agrees with previous studies [3,6,52,54]. It is established that important kinetics parameters, such as the diffusion coefficient, driving force and reaction constant, will be enhanced when the temperature increases. The dissolution time was reduced from 393 s to 238 s when the temperature was increased from 1500°C to 1550°C. The author suggests that the variation in dissolution time is due to the distinct reaction controlling mechanism at different temperature ranges [107]. The observed dissolution time was 120 s at 1600°C and it was relatively close to that at 1550°C.

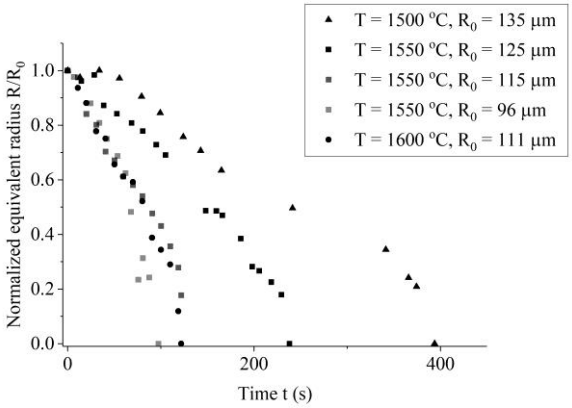

Figure 4.14 Normalized radius versus time at different temperatures in slag 1

A similar trend is found in slag 2 and in slag 1 and this is seen in Figure 4.15. The dissolution time decreases when the experimental temperature increases from 1550°C to 1600°C. In slag 2, CA_2 particles with about a 100 μm equivalent radius take about 50 s to completely dissolve at 1550°C. The dissolution curves of the two experiments at 1550°C show good consistency. This indicates that the experimental methodology has been successfully established. When the experimental temperature increases to 1600°C, the

dissolution time is significantly reduced to 27 s, which is about half of the dissolution time at 1550°C.

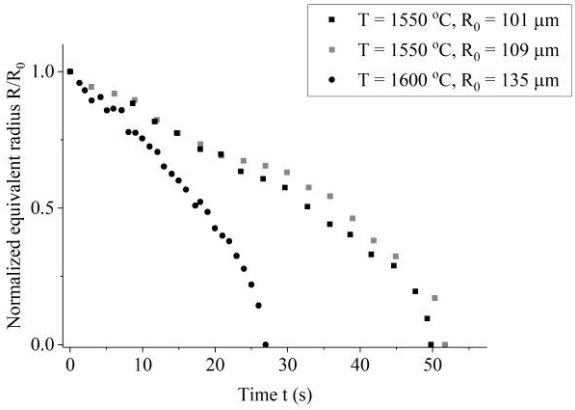

Figure 4.15 Normalized radius versus time at different temperatures in slag 2

As shown in the previous sections, the dissolution of CA_2 is controlled by diffusion in slag at both 1550°C and 1600°C. The rate depends on the diffusion coefficient D. It is conventional understanding that the correlation between the diffusion coefficient and temperature can be expressed by the Eyring's relation (Equation (2.31)) [69,116,117]. As shown in the earlier section, experimental data is close to the boundary layer diffusion control SCM which has an analytical solution of the dissolution time (Equation (2.6)). Substituting Equation (2.31) into Equation (2.6) shows that the total dissolution time is inversely proportional to the temperature (Equation (4.8)). The concentration difference of the dissolution driving force and slag viscosity of slag 1 and slag 2 at 1550°C and 1600°C are listed in Table 4.4. With the three variables, ΔC, η, T , calculated in Equation (4.8), and other parameters remaining virtually the same for each slag, the relations of the total dissolution time at the two different temperatures can be determined using the relation shown in Equation (4.9). Estimations based on Equation (4.9) predict that the dissolution

time at 1600°C is about 0.59 of the total dissolution time at 1550°C. The experimental results do follow the trend that Equation (4.9) predicts for when temperature increases.

Table 4.4 Dissolution driving force and viscosity of slag 1 and slag 2 at 1550 and 1600°C

Slag composition	Temperature (°C)	Dissolution driving force (mol/m^3 Al_2O_3)	Viscosity (Pa·S)
1	1550	6020	6.51
	1600	6639	4.32
2	1550	5872	0.493
	1600	6813	0.374

$$\tau = 3\frac{\rho {R_0}^2}{b\Delta C}\frac{\pi r\eta}{k_B T} \tag{4.8}$$

$$\tau \propto \frac{\eta}{\Delta C T} \tag{4.9}$$

Applying the corresponding parameters of slag 2 that are given in Table 4.4 to Equation (4.9) suggests that the dissolution time decreases with increments in temperature. This theoretical prediction agrees with the experimental data that is shown in Figure 4.15 and this agreement confirms that mass transfer in the slag phase is most likely the rate limiting step for the dissolution of CA_2 particles.

4.8 The Effect of Slag Composition on Dissolution Time

Figure 4.16 and Figure 4.17 compare the dissolution time of CA_2 particles at 1550°C and 1600°C. The solid and hollow data points are from experiments with slag 1 (S1) and slag 2

(S2). The important difference between the two slags was the SiO_2 content. Slag 1 and slag 2 had 46.3 and 5 wt% of SiO_2 content, respectively. The comparison included all experiments of particles with a similar radius [107].

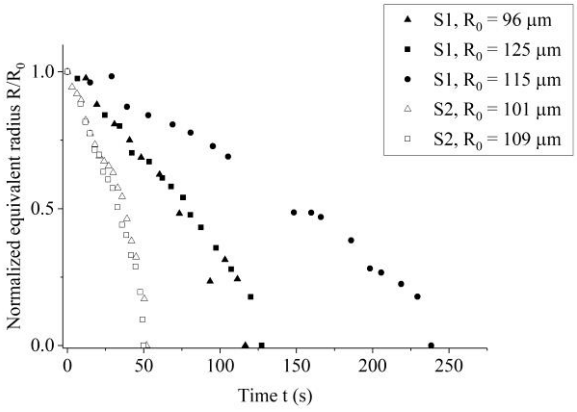

Figure 4.16 Normalized radius versus time at 1550°C in slag 1 and slag 2

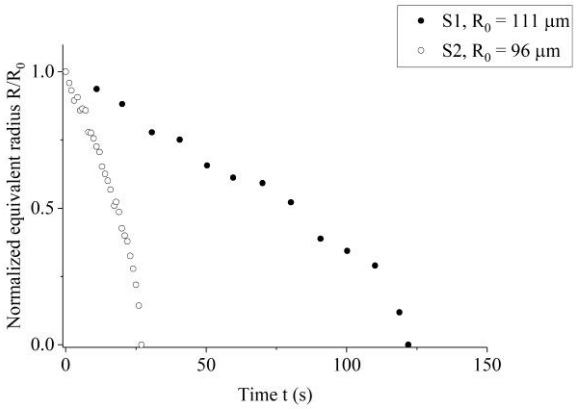

Figure 4.17 Normalized radius versus time at 1600°C in slag 1 and slag 2

The dissolution time of CA_2 particles in slag 2 was at least 70 % less than that for a similar sized particle in slag 1 at 1550°C. For all of the experiments in slag 1, the complete dissolution took more than 100 s while for experiments in slag 2, the dissolution time was

approximately 50 s. A similar occurrence was observed at 1600°C as well. A CA_2 particle of the same initial size took about 100 s more to completely dissolve in high SiO_2 S1 than in low SiO_2 S2 [107].

Equation (4.9) that was used to predict the effect of temperature can be further simplified into Equation (4.10) as comparisons are performed between particles that dissolve at the same temperature. The viscosity of slag 1 and slag 2 at 1550°C, calculated by the Urbain's model, are both given in Table 4.4. The viscosity of slag 1 is about 1 order of magnitude higher than that of slag 2. On the other hand, the concentration differences between the two slags are incomparable to the differences in viscosity. Equation (4.10) suggests that with such a combination of viscosity and dissolution driving force, the dissolution time will be significantly lowered for CA_2 to dissolve in slag 2 compared to slag 1. The trend is found to be the same as what Equation (4.10) predicts. A similar conclusion was made at a higher temperature of 1600°C. The dissolution rate of CA_2 will be significantly enhanced in lower SiO_2 content slag because of the distinct viscosity that determines the rate of mass transport.

$$\tau \propto \frac{\eta}{\Delta C} \tag{4.10}$$

4.9 **Experimental error**

The main source of error in the experiments is the uncertainty of particle size measurements based on the video of dissolution experiments. The CSLM is equipped with a camera that has very limited resolution. As shown in Figure 4.18 (a), the colour contrast between particle and slag is not sharp so the phase boundary between the particle and slag is blurry. Hence, it is difficult to confirm its exact location in the figure. Depending on the location

phase boundaries that were drawn during area measurements, the obtained equivalent radius may vary slightly. Two phase boundaries can be drawn around particles at locations where grayscale start to change (A in Figure 4.18 (b)) and locations where the changes become insignificant (B in Figure 4.18 (b)). The prior measures the minimum particle projection and the latter measures the maximum possible particle projection. An example is given in Figure 4.18 (b). It has been found that when considering the average of these two area measurements as "true" particle projection on horizontal plane, the error in area measurements $\Delta A \approx \pm 6\%$ in all experiments. Therefore, the error of an equivalent radius ΔR can be calculated with Equation (4.11) [118]. The ΔR increases as dissolution proceeds because of the A is in the denominator. However, the error of equivalent radius is still insignificant close to the end of dissolution because R is small.

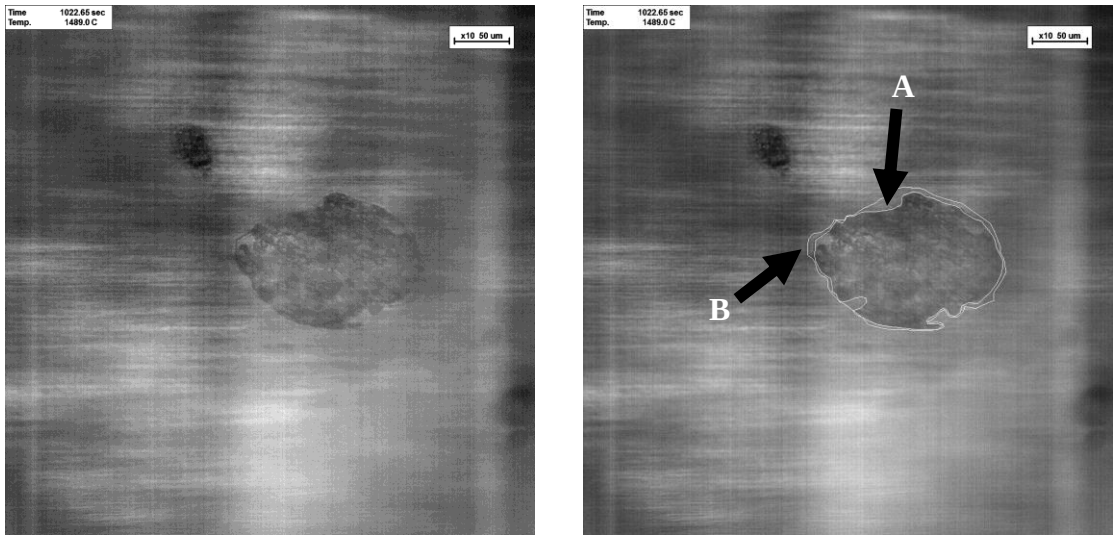

(a) (b)

Figure 4.18 Images of the CA_2 particle dissolving in slag 1 at 1550°C (a) without slag-inclusion boundary (b) with slag-inclusion boundaries

$$\Delta R = \frac{1}{2\sqrt{\frac{A}{\pi}}}\left(\frac{\Delta A}{\pi}\right) \tag{4.11}$$

Chapter 5 Modelling of the Dissolution Process

Developing a mathematical model is crucial to better understand the effects of important process parameters at high temperatures. For high temperature experiments, where obtaining quantitative results may be difficult, expensive and time consuming, mathematical modelling and numerical simulations can provide complementary insight to interpret experimental results and determine the fundamental phenomena of observed behaviour. The author compared the application of the existing models in the inclusion dissolution studies. These models are the chemical reaction control, boundary layer control, product layer control based on SCM and the diffusion in stagnant fluid control model. It has been found that the diffusion in stagnant fluid control model has the potential to describe the dissolution behaviour of CA_2 inclusions under the defined experimental conditions. However, as shown in section 4.5, the CA_2 dissolution mechanism changes with experimental conditions. It is in the author's and industries' interest to develop a universal inclusion dissolution model for various conditions. Further attempt made for better prediction of dissolution behaviour by modifying the model by introducing the new parameter correction factor f. The basis of introducing f into the stagnant fluid diffusion control model is provided in section 2.4.2.

The effect of selecting the diffusion coefficient and correction coefficient f, on the dissolution process, was studied based on the stagnant fluid control model. The solution of Equation (2.29) is represented by a relationship between a normalized radius and normalized time. Figure 5.1 (a) includes 6 normalized dissolution curves that are calculated with over 2 magnitudes of diffusion coefficients, including $D = 5\times10^{-12}$, 3×10^{-11}, 7×10^{-11}, 9×10^{-11}, 5×10^{-10} m^2/s, with the same arbitrary f = 0.5. The range of diffusion coefficients

that are used for this simulation cover the entire range of values that are suggested in the literature [65]. These curves are almost identical and they share a similar characteristic "S" shape for various diffusion coefficients. Figure 5.1 (b) shows 5 dissolution curves for f = 0.1, 0.3, 0.5, 0.7 and 0.9. The diffusion coefficient equals 7×10^{-11} m^2/s. These curves vary from the "S" shape and they are more parabolic. This indicates that the correction coefficient has a larger influence on the shape of the curve compared to the diffusion coefficient.

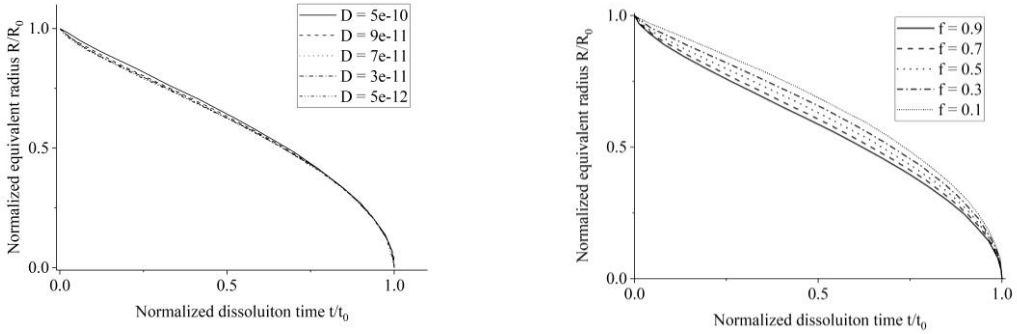

(a) (b)

Figure 5.1 Matlab solutions to Equation (2.29) with different (a) diffusion coefficient (b) correction coefficient

5.1 **Estimation of Correction Factors and Diffusion Coefficients**

A good estimation for f can be obtained by comparing numerical solutions of Equation (2.29) with experimental data. The only unknown is the diffusion coefficient D, which mainly affects the total dissolution time after other parameters are fixed in the previous steps. The first simulation was made using an experimental data for slag 2 (56.2% CaO-38.6% Al_2O_3-5.2% SiO_2) at 1600°C. Based on the corresponding phase diagram shown in Figure 4.5 (c), no reaction product is expected to be formed and slag is in direct equilibrium

with the CA_2 particle. At this condition, the driving force is the difference between the initial and saturated molar concentration of Al_2O_3 in slag. The Al_2O_3 saturated slag has a composition of 33CaO-64.5Al_2O_3-2.5SiO_2, that is all in weight percent. The calculated value of slag density is 2745 kg/m^3. The corrected density of sintered CA_2 is 2709 kg/m^3 at 1600°C and this converts to 20838 mol/m^3 Al_2O_3. The dimensionless driving forces were assumed to be constant at all three experimental temperatures. Therefore, the dimensionless saturation concentration k is calculated using 17358, 10539 and 20838 as C^i, C_0 and C^P and this yields k =1.8, which is shown in Equation (5.1).

$$k_{s2,1600℃} = \frac{C^i - C_0}{C^P - C^i} = \frac{17358 - 10539}{20838 - 17358} = 1.8 \tag{5.1}$$

In this calculation, an initial particle radius of 100 μm is assumed and this is close to the actual initial equivalent radius of CA_2 particles that are used in dissolution experiments. The diffusion coefficient of Al_2O_3 in 40CaO-20Al_2O_3-40 wt% SiO_2 slag equals 5×10^{-11}, which is used as the initial interpretation [65]. A correction coefficient with two decimal places was obtained through a two-step-interpretation. The correction coefficient is between 0 and 1 when diffusion in liquid slag is the rate controlling step. A total of 10 correction coefficients from 0 to 1 with increments of 0.1 are applied to Equation (2.29). The highest coefficient of determination R^2 was found be at 0.2. 11 correction coefficients, 0.16 to 0.25 with a 0.01 increment, are then applied to Equation (2.29) to find the best fit to experimental data. It has been found that the Matlab solution gives R^2 = 0.995248 when f = 0.20, with less than a 0.1 % difference between the R^2 value corresponding to f = 0.16 and f = 0.24. Figure 5.2 shows the normalized dissolution curves for f values ranging from 0.15 to 0.25. Comparisons of the normalized and un-normalized dissolution data and the

Matlab solution are shown in Figure 5.3. The value of the correction coefficient is fixed to be 0.20. The dissolution time for each particle is then calculated using the measured equivalent radius of each particle in Matlab with a range of diffusion coefficients. D = 7.2×10^{-11} m^2/s is the diffusion coefficient that best fits the experimental data of CA_2 dissolution in slag 2 at 1600°C.

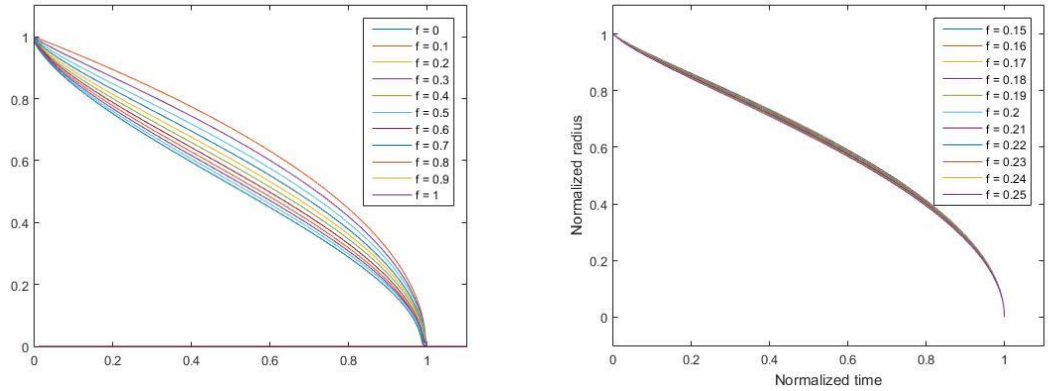

(a) (b)

Figure 5.2 Normalized Matlab solutions to diffusion in stagnant fluid control model for D = 5×10^{-11}, k = 1.8 and f from (a) 0 to 1 (b) 0.15 to 0.25

The most important difference between generating numerical solutions for each experimental condition comes from the different values of the dimensionless saturation concentration k. Unlike experiments in slag 2 at 1600°C, there is local equilibrium between slag and inclusion in other experimental conditions.

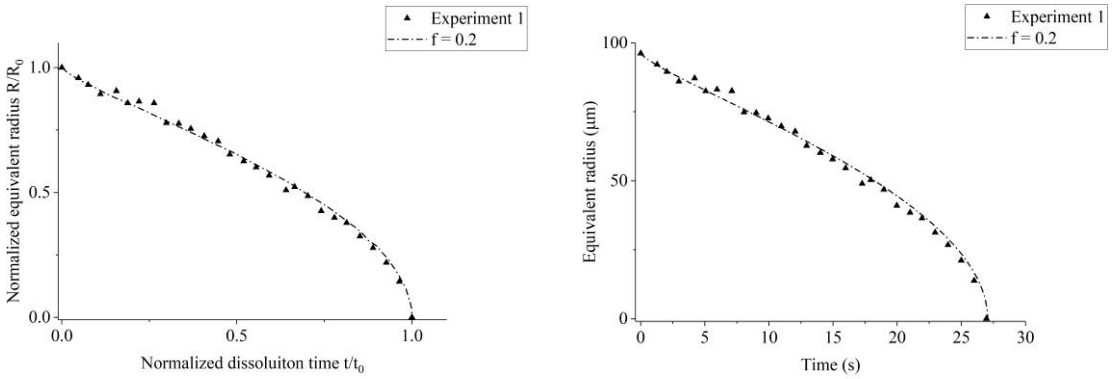

(a) (b)

Figure 5.3 Comparison of experimental and model prediction of (a) normalized (b) not normalized dissolution curve calculated with Matlab using D = 7.2×10^{-11}, k = 1.8 and f = 0.2

In the case of the dissolution of the CA_2 particle in slag 1 at 1500°C, slag reaches equilibrium with CAS_2 if slag is enriched with an Al_2O_3 particle at the inclusion-slag interface. Since CAS_2 is the only possible reaction product and it is the phase that contains the highest Al_2O_3 concentration in the system other than CA_2 inclusion, $C_{Al_2O_3\ in\ CAS_2} = C_{int}$ will be used to calculate the dimensionless saturation concentration k for this specific condition. The concentration of Al_2O_3 in CA_2 remains the same for all conditions and the bulk Al_2O_3 concentration depends on the slag that is used. The k is then calculated as:

$$k_{s1,1500℃} = \frac{C^i - C_0}{C^P - C^i} = \frac{9823 - 6423}{20838 - 9823} = 0.34 \qquad (5.2)$$

At higher temperatures of 1550°C and 1600°C, CAS_2 is not present based on the phase diagrams. So, no other reaction products are expected to form. C^i is the Al_2O_3 concentration in initial slag enriched with Al_2O_3 until it reaches Al_2O_3 activity where a = 0.47. The same approach was used for slag 1 in 1550°C and 1600°C. The k value is calculated as seen in

Equation (5.3) and (5.4). The interfacial slag composition is calculated and it equals 27.2CaO-33.7Al_2O_3-39.0SiO_2 and 26.1CaO-35.7Al_2O_3-38.2SiO_2 for 1550°C and 1600°C, respectively.

$$k_{s1,1550℃} = \frac{C^i - C_0}{C^P - C^i} = \frac{9056 - 6152}{20838 - 9056} = 0.25 \quad (5.3)$$

$$k_{s1,1600℃} = \frac{C^i - C_0}{C^P - C^i} = \frac{9551 - 6121}{20838 - 9551} = 0.30 \quad (5.4)$$

The remaining experimental condition is the S2 at 1550°C. When CA_2 dissolves in S2 at 1550°C, there is only one possible reaction product which is CA. However, as explained earlier, the CA product layer is not expected to fully stop dissolution in liquid because neither clear product layer was observed nor the experimental dissolution curves share the similar S-shape characteristics as seen in CA_2 dissolution experiments in slag 1 at 1500°C. Since slag-CA-CA_2 three phase local equilibrium is expected in the crevice of the non-continuous CA product layer, the interfacial Al_2O_3 concentration is calculated using a slag composition of 35.1CaO-60.8Al_2O_3-4.1SiO_2. This corresponds to the three phase equilibrium point that is seen in Figure 4.5 (c).

$$k_{s2,1550℃} = \frac{C^i - C_0}{C^P - C^i} = \frac{16464 - 10592}{20838 - 16464} = 1.34 \quad (5.5)$$

Figure 5.4 compares the dissolution curves for CA_2 particles in slag 1 at 1500°C, 1550°C, 1600°C and in slag 2 at 1550°C with respect to various f values. All of the parameters for the calculations are listed in Table 5.1. The value of best fitted f factors decreased as the

viscosity of slag decreased. This result is consistent with the theory suggested by Michelic et al.[41,42]. It seems that further increments of the correction coefficient f with values larger than 1 yield a solution that is similar to the result of the diffusion in the product layer control model from SCM.

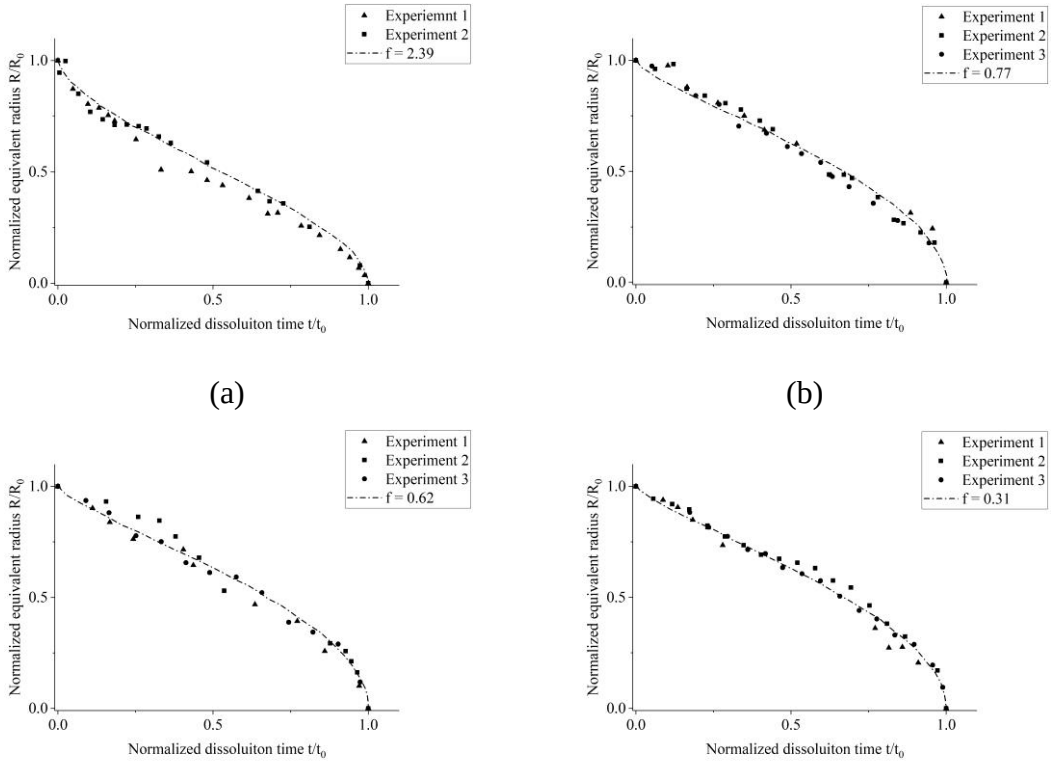

Figure 5.4 Normalized Matlab solutions to the diffusion in stagnant fluid control model for (a) slag 1, 1500°C (b) slag 1, 1550°C (c) slag 1, 1600°C (d) slag 2, 1550°C

The diffusion coefficient D can be calculated by substituting values to the function and comparing with the experimental data. The calculated, best fitting diffusion coefficients for all of the experimental data and the average of the best fitting diffusion coefficients for the same experimental condition can be found in Table 5.1. The values for the measured

dissolution time are also provided in Table 5.1 for comparison. There is a reasonable agreement between the calculated and measured values from this work and those reported by Monaghan et al. [38].

To the best of the author's knowledge, only one mathematical expression that correlates to the correction coefficient and physical properties of the system has been proposed. Feichtinger et al. [41] suggested a linear correlation between the correction coefficient and the dynamic viscosity of bulk slag. However, the suggested correction coefficients were relatively different from the values that were calculated by the proposed correlation. In the present study, a modified correlation between the correction coefficient f and the viscosity of slag at slag-inclusion interface is proposed. The empirical correlation is given in Equation (5.6), where $\alpha = 0.28$ and $\beta = 0.31$ for CA_2 dissolution in slag 1 and slag 2. Parameters α and β most likely depend on the properties of the systems. Figure 5.5 shows the linearized Equation (5.6), with the x-axis and y-axis being logarithmic viscosity and correction coefficient, respectively. The error has a fixed value of 0.04 so the variation in R^2 is less than 0.1%.

Equation (5.6) is valid for $0.33 < \eta < 11.7$. The range was defined for $0 < f < 1$. More experiments are clearly needed to further confirm Equation (5.6), but it is valid for four experimental conditions that are studied in the present study. It should be noted that the correlation between the correction coefficients and the physical properties of the system was not determined for the cases that dissolution is governed by mass transport in solid reaction product due to the lack of experimental data. Alternative properties need to be introduced to associate the correction coefficient with all experimental conditions.

$$f = \alpha\, ln(\eta) + \beta \tag{5.6}$$

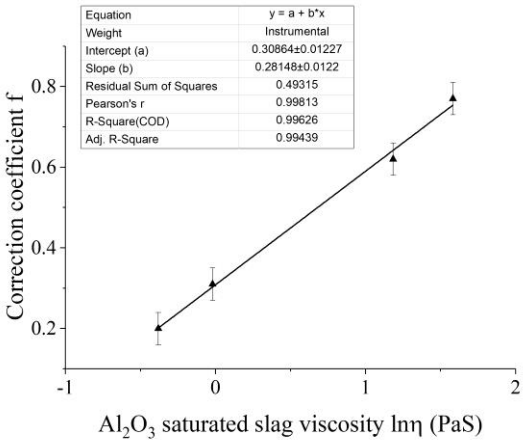

Figure 5.5 Linearized Equation (5.6) and the linear fitting calculated by Origin 2017

Table 5.1List of best fitted diffusion coefficients and the difference between measured and calculated dissolution time

Sample (slag-temperature-number)	Initial radius (μm)	Measured dissolution time, t_m (s)	Calculated diffusion coefficient $D\times10^{-11}$ (m^2/s)	Best fitted correction coefficient (m^2/s)	Average diffusion coefficient (m^2/s)	Calculated dissolution time t_c(s)	Δt (t_m-t_c) (s)
S1-1500-1	226	1861	1.1	2.39	1.5±0.40	1374	478
S1-1500-2	135	393	1.9			493	-100
S1-1500-3	171	770	1.5			791	-21
S1-1550-1	96	116	12	0.77	12±2.5	110	6
S1-1550-2	125	238	9.0			185	53
S1-1550-3	115	127	14			157	-30
S1-1600-1	417	768	26	0.62	16±9.2	1298	-530
S1-1600-2	216	355	15			350	5
S1-1600-3	111	181	7.8			94	87
S2-1550-1	150	190	3.2	0.31	5.0±1.65	123	67
S2-1550-2	109	52	6.4			66	-14
S2-1550-3	101	50	5.5			56	-6
S2-1600-1	96	27	7.2	0.2	-	-	-

The proposed correlation between correction coefficients and viscosities of saturated slag is applied to predict the values of the f factor for the dissolution of SiO_2 particles in slag at 1450°C [41]. The experimental data for 6 slag compositions is taken from the study of Feichtinger et al.[41]. The correlation that is suggested by them is provided in section 2.4.2. The corresponding SiO_2 saturated slag calculated by FactSage is shown in Table A.3 in the Appendix. Figure 5.6 plots the reported correction coefficients and the corresponding viscosities of saturated slag. Agreement is found between the reported correction coefficients and logarithmic viscosity of SiO_2 saturated slag 1, 2, 5 and 6. Slag 3 and 4 did not follow the same trend.

However, the correctness of the reported correction coefficients for slag 3 and slag 4 remains questionable. If f values, in some extent, quantify "the easiness of concentration gradient development", f is expected to increase as the viscosity of interfacial slag increases. Yet, the reported correction coefficients are lower values in slag with a higher viscosity (Sat 3, 4 in Table A.3) compared to those in lower viscosity slags (Sat 1, 2 in Table A.3). In other words, the reported values did not agree with the proposed trend of correction coefficients decrease with slag viscosity.

It is worth mentioning that the slope α of the SiO_2 dissolution curves in Figure 5.6 is almost identical to the value for the CA_2 dissolution (Figure 5.5). At the current stage of this study, it remains unknown whether that is a coincidence or if that has scientific meanings.

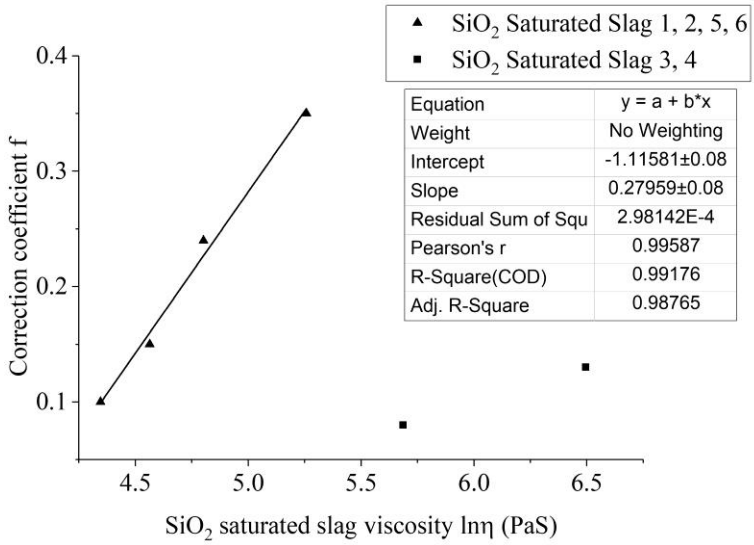

Figure 5.6 Linear fitting of correction coefficients and SiO_2 saturated slag viscosity calculated by Origin 2017 [41]

5.2 **Validation of the Model**

The dissolution model incorporating a modified correlation for the correction coefficients is validated against experimental data of alumina dissolution in slag at 1550°C and 1600°C available in literature [6,38]. Applying Equation (2.29) to the dissolution of various types of inclusions other than CA_2 may confirm the applicability of the dissolution model.

A thermodynamics analysis using FactSage confirms that there is a local equilibrium between slag and Al_2O_3 at the slag-inclusion interface. The parameters required for the calculation are provided in Table A.2. The Al_2O_3 saturated slag has a composition of 21.6CaO-45.2Al_2O_3-33.2 wt% SiO_2 and 20CaO-48.8Al_2O_3-31.2SiO_2 at 1550°C and 1600°C, respectively. The corresponding viscosity of slag equals 3.94 Pa·S and 2.39 Pa·S at 1550°C and 1600°C, respectively. The density of Al_2O_3 is assumed to be 34986 mol/m^3

[38] at both temperatures because the change in density due to thermal expansion is insignificant within the temperature range that is being studied. The dimensionless concentration, k and the correction coefficient f based on the Equation (5.6) equal 0.264 and 0.69 at 1550°C whereas k and f are 0.299 and 0.55 at 1600°C. The total dissolution time of Al_2O_3 particles is predicted with respect to the known initial size, k, and f using Equation (2.29). In Figure 5.7, the model predictions are compared with the experimental data that is obtained by Liu et al. [6]. A comparison of normalized plots from Figure 5.7 is provided in Figure 5.8. The calculated diffusion coefficients are provided in Table 5.2. The difference between the reported and calculated diffusion coefficients is insignificant. The agreement between the experimental data and the calculated diffusion curves after introducing correction coefficients is better than the normalized dissolution curves calculated by Liu et al. [6].This result suggests that the modified model can predict the dissolution of Al_2O_3 particles in the slag system that is studied and the correlation between viscosity and the correction coefficient f, shown in Equation (5.6), is valid for the system in which the diffusion of Al_2O_3 controls the dissolution process.

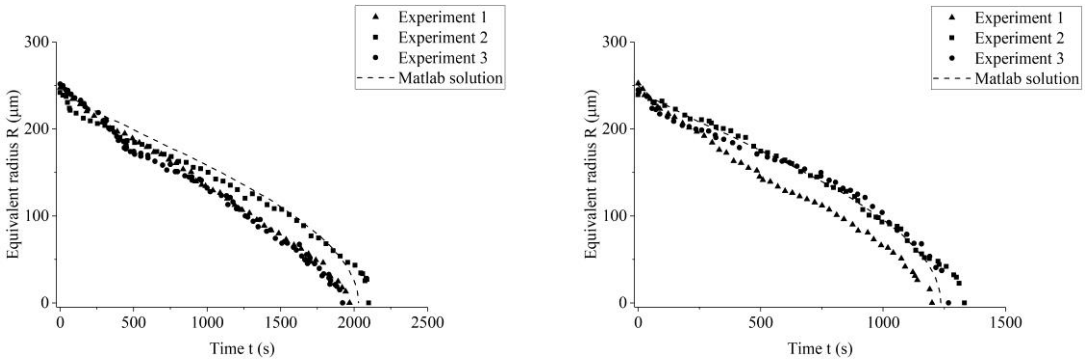

(a) (b)

Figure 5.7 Dissolution profile of Al_2O_3 particles in molten slag at by Liu et al. at (a) 1550°C (b) 1600°C [6]

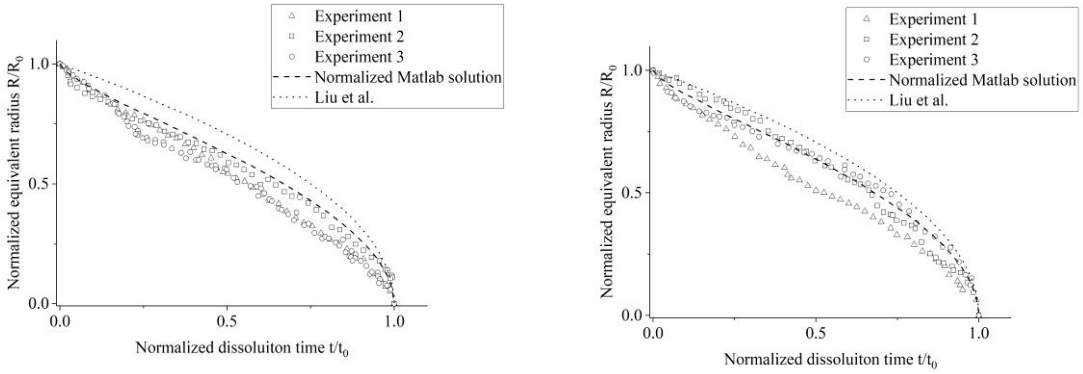

(a) (b)

Figure 5.8 Normalized dissolution profile of Al_2O_3 particles in molten slag at (a) 1550°C (b) 1600°C [6]

The initial radius of Al_2O_3 particles is 250 μm in the dissolution study by Liu et al [6]. Based on the modified model that is proposed in this work, the dissolution coefficient of an Al_2O_3 inclusion is predicted to be 3.9×10^{-11} m^2/s at 1550°C (Figure 5.7 (a)) and 5.9×10^{-11} m^2/s at 1600°C (Figure 5.7 (b)). These values are in agreement with those that are reported in the literature [6]. Similar numerical solutions for Equation (2.29) can be obtained using the Runge-Kutta or Lattice Boltzmann method [6]. On the other hand, applying the stagnant

fluid control model to the dissolution data that is reported by Monaghan et al. [38] indicates that when the initial equivalent radius is 30.5 μm, a diffusion coefficient of 3.9×10^{-11} m^2/s is needed to achieve a dissolution time of 31 s at 1550°C, as given in the literature. The diffusion is calculated to be 3.7×10^{-11} m^2/s if a 35 μm radius Al_2O_3 particle dissolves in 44 s. A summary of the reported and calculated diffusion coefficients is provided in Table 5.2.

Table 5.2Diffusion coefficients reported in the literature and calculated based on Equation (2.29) for slag similar to slag 1 at 1550°C

Initial particle radius (μm)	Dissolution time (s)	Reported diffusion coefficients $D\times10^{-11}$ (m^2/s)	Calculated diffusion coefficients $D\times10^{-11}$ (m^2/s)	Calculated diffusion coefficients Average $D\times10^{-11}$ (m^2/s)	Ref.
247	1969	3.4	3.9	3.9±0.35	[6]
242	2099	3.3	3.5		
252	1923	3.8	4.2		
30.5	31	1.6	3.9	3.8±0.14	[38]
35	44	1.87	3.7		

The average diffusion coefficients reported by Monaghan et al. and Liu et al. are 1.74×10^{-10} and 3.5×10^{-11} m^2/s at 1550°C, respectively [6,38]. They differ by about one order of magnitude. However, excellent agreement between the dissolution coefficients values at 1550°C was found after introducing the correction coefficients to the model. The dissolution coefficients values were calculated based on the experimental data of two Al_2O_3 dissolution studies.

The diffusion coefficient of Al_2O_3, that was calculated based on the CA_2 dissolution data at 1550°C, is 1.2×10^{-10} m^2/s as given in Table 5.1. This value is higher than the predicted values from this work and that can be seen in Table 5.2 [6,38]. The diffusion coefficients based on the CA_2 dissolution are believed to still be correct but further analysis is required to better explain the relationship between the diffusion coefficients, f factor and the composition of slag at the slag-inclusion interface.

Chapter 6 Improvements and Future Works

This study provided new knowledge on the dissolution kinetics of CA_2 particles in steelmaking slags at high temperatures. However, a few improvements should be made:

- The slag-inclusion interface should be analysed for each experimental condition to confirm the formation of product layer. Due to limited time, the interface between CA_2 particle and slag 1 was analysed for the experiment at 1500°C using the SEM. It is essential to have a better understanding of the mechanism with the aid of characterization techniques.

- The modelling approach discussed in the present study applies to limited cases. More experiments with different slag compositions should be conducted to validate the model. The correlation between slag viscosity and the correction coefficients must be refined with more experiments.

- The proposed diffusion coefficients of Al_2O_3 in slag 1 do not agree with the theoretical prediction. This is most likely due to the fact that sufficient data is not collected during experiments. The current experimental setup has the disadvantage of not being able to enforce particle immersion after experimental temperatures are reached. In order to achieve ideal experimental conditions, experimental approaches need to be modified so that the dissolution data captures the early stage of the dissolution curves correctly.

- Another calcium aluminate inclusion type that is problematic to the quality of steel and processing is CA_6. The author was not able to study CA_6 particles due to difficulties in particle preparation within the defined time. The production technique needs to be improved in order to produce dense CA_6 particles for dissolution experiments. Gaining knowledge on the dissolution kinetics of CA_6 particles can provide a better picture of interplay between inclusion removal and calcium treatment during the refining process.

- Finally, the effect of convection on dissolution kinetics was indirectly incorporated in the modified dissolution model by correlating correction coefficients with interfacial slag viscosity. In the present study, the effect of convection is less significant than diffusion as inclusions only experience minor rotations and movements. However, with the ultimate goal of developing a general mathematical model that correctly models all major phenomenon observed during inclusion dissolution, a clearer understanding of the effect of convection on dissolution kinetics is essential. It will be ideal to directly include the relative motion between slag and inclusions as part of the model.

Chapter 7 Conclusions

The dissolution behaviour of CA_2 particles in the CaO-SiO_2-Al_2O_3 slags was studied in the temperature range of 1500°C to 1600°C by using CSLM. The following conclusions can be drawn from this study:

1. Techniques to produce high purity and dense CA_2 particles were established. By producing synthetic inclusions with a known size and composition, a better control of the initial conditions of dissolution kinetic experiments is achieved.

2. The dissolution rate increases as the temperature increases. The dissolution driving force and diffusion coefficients both increase with temperature, and this results in an accelerated CA_2 dissolution rate at a higher temperature in both slag systems.

3. Slag compositions have shown to have a significant effect on the dissolution rate. The dissolution time is reduced in low SiO_2 slag S2 by approximately 50%. The accelerated dissolution in slag 2 can be related to the significantly lower viscosity compared to slag 1 at any temperature. Slag viscosity is inversely proportional to the diffusion coefficient according to Eyring's relation. Therefore, the dissolution rate, which is proportional to the diffusion coefficient when diffusion in slag is in control, will increase with a lower slag viscosity.

4. Temperature affects the CA_2 dissolution rate but it's not always by increasing the rate related constants. The dissolution mechanism may also vary with temperature. For CA_2 dissolution in slag 1, the dissolution mechanism changes from diffusion in the product

layer control to diffusion control in slag when CAS_2 becomes thermodynamically unfavourable at 1550°C and 1600°C. When the formation of a reaction product is not thermodynamically favourable, the dissolution of CA_2, in both S1 and S2, is governed by diffusion in slag.

5. An improvement in the diffusion in stagnant fluid control model is proposed in the present study by introducing a correlation between slag viscosity and the correction coefficient using the equation below. It should be noted that viscosity is calculated using the slag composition at the slag-inclusion interface.

$$f = 0.28\ln(\eta) + 0.31$$

6. The calculated diffusion coefficient of alumina in slag 1 is 1.2×10-10 m2/s at 1550°C and 1.6×10-10 m2/s at 1600°C. This is in agreement with the values that have been reported by other researchers. There is a discrepancy in the prediction of the diffusion coefficient of alumina in slag 2. Further analysis is required to better understand this discrepancy..

References

1 L. Holappa and O. Wijk: in *Treatise on Process Metallurgy, Volume 3: Industrial Processes*, Elsevier, 2014, pp. 347–72.

2 E.T. Turkdogan: *Fundamentals of Steelmaking*, The Institute of Materials, London, 1996.

3 K.W. Yi, C. Tse, J.H. Park, M. Valdez, A. W. Cramb, and S. Sridhar: *Scand. J. Metall.*, 2003, vol. 32, pp. 177–84.

4 K.H. Sandhage and G.J. Yurek: *J. Am. Ceram. Soc.*, 1990, vol. 73, pp. 3633–42.

5 J. Liu, M. Guo, P.T. Jones, F. Verhaeghe, B. Blanpain, and P. Wollants: *J. Eur. Ceram. Soc.*, 2007, vol. 27, pp. 1961–72.

6 J. Liu, F. Verhaeghe, M. Guo, B. Blanpain, and P. Wollants: *J. Am. Ceram. Soc.*, 2007, vol. 90, pp. 3818–24.

7 B.J. Monaghan, L. Chen, and J. Sorbe: *Ironmak. Steelmak.*, 2005, vol. 32, pp. 258–64.

8 Flow line of steelmaking, http://mining-technology.blogspot.ca/2009/05/steel-making-flowchart.html.

9 J. Feng and Y. Bao, eds.: *College Planning Materials: Iron and Steel Metallurgy Tutorial*, College planning materials: iron and steel metallurgy tutorial, 1991.

10 L. Holappa: in *Treatise on Process Metallurgy*, vol. 3, Elsevier Ltd, 2014, pp. 301–45.

11 M. Pomeroy: 2015.

12 L. Ya, Z. Yang, Z. Ren, Y. Sun, and S. Zhou: *College Planning Materials: Steel School*, 1st edn., Metallurgical Industry Press, Beijing, 2010.

13 B. Deo and R. Boom: *Fundamentals of Steelmaking Metallurgy*, 1993.

14 Z. Jian, ed.: *Refining Theory and Practice*, Metallurgical Industry Press, 1999.

15 L. Holappa: *Steel Res. Int.*, 2010, vol. 81, pp. 869–74.

16 J. Son, I. Jung, S. Jung, H. Gaye, and H. Lee: *ISIJ Int.*, 2008, vol. 48, pp. 1542–51.

17 J.H. Park: *Metall. Mater. Trans. B Process Metall. Mater. Process. Sci.*, 2007, vol. 38, pp. 657–63.

18 B. Harcsik and G. Karoly: *Steel Res. Int.*, 2013, vol. 84, pp. 129–35.

19 F. Fuhr, C. Cicutti, G. Walter, and G. Torga: *Iron Steelmak.*, 2003, vol. 30, pp. 53–8.

20 W. Tiekink, R. Boom, A. Overbosch, R. Kooter, and S. Sridhar: *Ironmak. Steelmak.*, 2010, vol. 37, pp. 488–95.

21 R.B.Snow.A.J.A. Shea: *J. Am. Ceram. Soc.*, 1949, vol. 32, pp. 187–94.

22 H. Cui, Y.P. Bao, M. Wang, and W.S. Wu: *Int. J. Miner. Metall. Mater.*, 2010, vol. 17, pp. 154–8.

23 J. Strandh, K. Nakajima, R. Eriksson, and P. Jönsson: *ISIJ Int.*, 2005, vol. 45, pp. 1838–47.

24 M. Herrera, F. Castro, M. Castro, M. Méndez, H. Solís, A. Castellá, and M. Barbaro: *Ironmak. Steelmak.*, 2006, vol. 33, pp. 45–51.

25 L.F. Zhang and S. Taniguchi: *Int. Mater. Rev.*, 2000, vol. 45, pp. 59–82.

26 M. Valdez, G.S. Shannon, and S. Sridhar: *ISIJ Int.*, 2006, vol. 46, pp. 450–7.

27 B. Coletti, B. Blanpain, S. Vantilt, and S. Sridhar: *Metall. Mater. Trans. B*, 2003, vol. 34, pp. 533–8.

28 P. Misra, V. Chevrier, S. Sridhar, and A. W. Cramb: *Metall. Mater. Trans. B*, 2000, vol. 31, pp. 1135–9.

29 D. Bouris and G. Bergeles: *Metall. Mater. Trans. B Process Metall. Mater. Process. Sci.*, 1998, vol. 29, pp. 641–9.

30 D.Y. Sheng, M. Söder, P. Jönsson, and L. Jonsson: *Scand. J. Metall.*, 2002, vol. 31, pp. 134–47.

31 M. Hallberg, P.G. Jönsson, T.L.I. Jonsson, and R. Eriksson: *Scand. J. Metall.*, 2005, vol. 34, pp. 41–56.

32 L. Zhang and B.G. Thomas: *Rep. No. CCC200206, Univ. Illinois Urbana-Champaign*, 2003, pp. 1–19.

33 C. Lyons and P. Kaushik: *Steel Res. Int.*, 2011, vol. 82, pp. 1394–403.

34 S.K. Michelic, G. Wieser, and C. Bernhard: *ISIJ Int.*, 2011, vol. 51, pp. 769–75.

35 K. Sandhage and G. Yurek: *J. Am. Ceram. Soc.*, 1990, vol. 73, pp. 3643–9.

36 F. Oeters: *Metallurgy of Steelmaking*, 1994.

37 O. Levenspiel: *Chemical Reaction Engineering*, vol. 38, 1999.

38 B.J. Monaghan and L. Chen: *J. Non. Cryst. Solids*, 2004, vol. 347, pp. 254–61.

39 S.H. Lee, C. Tse, K.W. Yi, P. Misra, V. Chevrier, C. Orrling, S. Sridhar, and A.W. Cramb: *J. Non Cryst. Solids*, 2001, vol. 282, pp. 41–8.

40 P. Yan, B.A. Webler, P.C. Pistorius, and R.J. Fruehan: *Metall. Mater. Trans. B*, 2015, vol. 46, pp. 2414–8.

41 S. Feichtinger, S.K. Michelic, Y.B. Kang, and C. Bernhard: *J. Am. Ceram. Soc.*, 2014, vol. 97, pp. 316–25.

42 S. Michelic, J. Goriupp, S. Feichtinger, Y.-B. Kang, C. Bernhard, and J. Schenk: *Steel Res. Int.*, 2015, vol. 86, p. n/a-n/a.

43 H. Chikama, H. Shibata, T. Emi, and M. Suzuki: *Mater. Trans.*, 1996, vol. 37, pp. 620–6.

44 H. Shibata, Y. Arai, M. Suzuki, and T. Emi: *Metall. Mater. Trans. B*, 2000, vol. 31, pp. 981–91.

45 T. Emi, M. Suzuki, H. Shibata, H. Yin and S. Yoshinaga: *ISIJ Int.*, 1998, vol. 38, pp. 149–56.

46 Y. Kang, B. Sahebkar, P.R. Scheller, K. Morita, and D. Sichen: *Metall. Mater. Trans. B Process Metall. Mater. Process. Sci.*, 2011, vol. 42, pp. 522–34.

47 C. Orrling, S. Sridhar, and A.W. Cramb: *ISIJ Int.*, 2000, vol. 40, pp. 877–85.

48 W. Mu, N. Dogan, and K.S. Coley: *Metall. Mater. Trans. B*, 2017, vol. 48, pp. 2092–103.

49 W. Mu, N. Dogan, and K.S. Coley: *Metall. Mater. Trans. B*, 2017, pp. 1–10.

50 V. Prasad, D. Semwogerere, and E.R. Weeks: *J. Phys. Condens. Matter*, 2007, vol. 19, pp. 1-25.

51 UCLA: The Confocal Microscope, http://www.gonda.ucla.edu/bri-core/confocal.htm.

52 B.J. Monaghan, S.A. Nightingale, L. Chen, and G.A. Brooks: in *International Conference on Molten Slags Fluxes and Salts*, 2004, pp. 585–94.

53 J.Y. Choi, H.G. Lee, and J.S. Kim: *ISIJ Int.*, 2002, vol. 42, pp. 852–60.

54 M. Valdez, K. Prapakorn, A.W. Cramb, and S. Sridhar: *Ironmaking and Steelmaking*, 2002, vol. 29, pp. 47–52.

55 S. Sridhar and A. W. Cramb: *Metall. Mater. Trans. B*, 2000, vol. 31, pp. 406–10.

56 S. Taira, K. Nakashima, and K. Mori: *ISIJ Int.*, 1993, vol. 33, pp. 116–23.

57 M. Valdez, K. Prapakorn, A.W. Cramb, S. Sridhar, M. Valdez, K. Prapakorn, A.W. Cramb, and S. Sridhar: *Ironmak. Steelmak.*, 2002, vol. 29, pp. 47–52.

58 Z.. Sun, X. Guo, J.V. Dyck, M. Guo, and B. Blanpain: *AIChE J.*, 2013, vol. 59, pp. 2907–16.

59 X. Guo, Z. Sun, J. V. Dyck, M. Guo, and B. Blanpain: *Ind. Eng. Chem. Res.*, 2014, vol. 53, pp. 6325–33.

60 S.H. Amini, M.P. Brungs, S. Jahanshahi, and O. Ostrovski: *Metall. Mater. Trans. B Process Metall. Mater. Process. Sci.*, 2006, vol. 37, pp. 773–80.

61 S. Amini, M. Brungs, and O. Ostrovski: *ISIJ Int.*, 2007, vol. 47, pp. 32–7.

62 T. Deng and D. Sichen: *Metall. Mater. Trans. B Process Metall. Mater. Process. Sci.*, 2012, vol. 43, pp. 578–86.

63 T. Hamano, M. Horibe, and K. Ito: *ISIJ Int.*, 2004, vol. 44, pp. 263–7.

64 B.J. Monaghan and L. Chen: *Ironmak. Steelmak.*, 2006, vol. 33, pp. 323–30.

65 V.D. Eisenhuttenleute, ed.: *Slag Atlas*, 2nd edn., Verlag Stahleisen GmbH, Dusseldorf, 1995.

66 R. Hagemann, L. Pettsold, and P.R. Sheller: *Metall. Min. Ind.*, 2010, vol. 2, pp. 262–6.

67 J. Park and H. Todoroki: *ISIJ Int.*, 2010, vol. 50, pp. 1333–46.

68 B.J. Monaghan, S.A. Nightingale, L. Chen, and G.A. Brooks: *Mater. Sci.*, 2004, pp. 585–94.

69 H. Soll-Morris, C. Sawyer, Z.T. Zhang, G.N. Shannon, J. Nakano, and S. Sridhar: *Fuel*, 2009, vol. 88, pp. 670–82.

70 Y. Tomita: *Mater. Sci. Technol.*, 1989, vol. 5, pp. 1084–9.

71 J.P.C. Cicutti, M. Valdez, T. Perez, R. Ares and R. Panelli: *Steelmak. Conf. Proc.*, 2001, vol. 250, pp. 871–82.

72 Y. Ueshima, H. Kato, K. Kondo, and T. Mizoguchi: *High Temp. Mater. Process.*, 2012, vol. 31, pp. 431–8.

73 S. Abdelaziz, G. Megahed, I. El-Mahallawi, and H. Ahmed: *Ironmak. Steelmak.*, 2009, vol. 36, pp. 432–41.

74 J.M.A. Geldenhuis and P.C. Pistorius: *Ironmak. Steelmak.*, 2000, vol. 27, pp. 442–9.

75 S. Basak, R. Kumar Dhal, and G.G. Roy: *Ironmak. Steelmak.*, 2010, vol. 37, pp. 161–8.

76 D. Lu: McMaster University, 1992.

77 D.L.Sponseller. and R.A.Flinn: *Trans AIME 230*, 1964, pp. 876–87.

78 M. Köhler, H.J. Engell, and D. Janke: *Steel Res. 8*, vol. 1985, pp. 419–23.

79 Japan Society for the Promotion of Science: *Steelmaking Data Sourcebook*, Gordon and Breach Science Publishers, New York, 1988.

80 L. Holappa, M. Hämäläinen, M. Liukkonen, and M. Lind: *Ironmak. Steelmak.*, 2003, vol. 30, pp. 111–5.

81 H.M. and R.I. H. Nashiwa, A. Mori, S. Ura and T. Ikeda: in *The 6th Japan-USSR Joint Symposium on Physical Chemistry of Metallurgical Processes*, 1977.

82 H. Ohta and H. Suito: 2003, vol. 43, pp. 1293–300.

83 S. Ban-Ya. H. Itoh and M. Hino: *Metall. Mater. Trans. B*, 1997, vol. 28, pp. 953–6.

84 K. Kawakami, T. Taniguchi, and K. Nakashima: *Tetsu-to-Hagane*, 2007, vol. 93, pp. 743–52.

85 S. Yang, L. Zhang, L. Sun, J. Li, and K.D. Peaslee: *Iron Steel Technol.*, 2012, vol. 9, pp. 245–58.

86 M. Jiang, X. Wang, B. Chen, and W. Wang: *ISIJ Int.*, 2010, vol. 50, pp. 95–104.

87 A. Mrad: *Private Conversation*, 2016.

88 G. Ye, P. Jonsson, and T. Lund: *ISIJ Int.*, 1996, vol. 36, p. Supplement,S105-S108.

89 Y. Ren, L. Zhang, and S. Li: *ISIJ Int.*, 2014, vol. 54, pp. 2772–9.

90 M. Lind and L. Holappa: *Metall. Mater. Trans. B Process Metall. Mater. Process. Sci.*, 2010, vol. 41, pp. 359–66.

91 W. Yang, L. Zhang, X. Wang, Y. Ren, X. Liu, and Q. Shan: *ISIJ Int.*, 2013, vol. 53, pp. 1401–10.

92 Y. Wang, S. Sridhar, and M. Valdez: *Metall. Mater. Trans. B*, 2002, vol. 33, pp. 625–32.

93 S.K. Choudhary and A. Ghosh: *ISIJ Int.*, 2008, vol. 48, pp. 1552–9.

94 R.J. Fruehan and K. Larsen: in *Steelmaking conference Proceedings*, vol. 73, 1990, pp. 497–506.

95 N. Verma, P.C. Pistorius, R.J. Fruehan, M. Potter, M. Lind, and S.R. Story: *Metall. Mater. Trans. B*, 2011, vol. 42, pp. 720–9.

96 N. Verma, P.C. Pistorius, R.J. Fruehan, M. Potter, M. Lind, and S. Story: *Metall. Mater. Trans. B Process Metall. Mater. Process. Sci.*, 2011, vol. 42, pp. 711–9.

97 Y. Higuchi, M. Numata, S. Fukagawa, and K. Shinme: *ISIJ Int.*, 1996, vol. 36, pp. S151–4.

98 N. Verma, P.C. Pistorius, R.J. Fruehan, M.S. Potter, H.G. Oltmann, and E.B. Pretorius: *Metall. Mater. Trans. B Process Metall. Mater. Process. Sci.*, 2012, vol. 43, pp. 830–40.

99 W. Yang, X. Wang, L. Zhang, and W. Wang: *Steel Res. Int.*, 2013, vol. 84, pp. 878–91.

100 D. Yang, X. Wang, G. Yang, P. Wei, and J. He: *Steel Res. Int.*, 2014, vol. 85, pp. 1517–24.

101 B.M. Mohamed and J.H. Sharp: *J. Mater. Chem.*, 1997, vol. 7, pp. 1595–9.

102 B.M. Mohamed and J.H. Sharp: *Thermochim. Acta*, 2002, vol. 388, pp. 105–14.

103 Y. Wang and W. Thomson: *Thermochim. Acta*, 1995, vol. 255, pp. 383–90.

104 K. Chu and R. Thompson: *J. Chem. Eng. data*, 1962, vol. 7, pp. 358–60.

105 S. Jonas, F. Nadachowski, and D. Szwagierczak: *Ceram. Int.*, 1998, vol. 24, pp. 211–6.

106 W. D.Callister: *Materials Science and Engineering an Introduction*, 2007.

107 K. Miao, A. Haas, M. Sharma, W. Mu, and N. Dogan: *Metall. Mater. Trans. B.*, currently under review.

108 Technical Notes: Thermocouple Accuracy, http://www.microlink.co.uk/tctable.html.

109 S. Jonas, F. Nadachowski, and D. Szwagierczak: *Science (80-.).*, 1999, vol. 25, pp. 77–84.

110 R. Frykholm, M. Ekroth, B. Jansson, J. Agren, and H.-O. Andren: 2003, vol. 51, pp. 1115–21.

111 J. Hoogschagen: *Ind. Eng. Chem.*, vol. 47, pp. 906–12.

112 A. Engstrim, L. Hoglund, and J. Agren: 1994, vol. 25, pp. 1127–34.

113 H. Abdeyazdan, B.J. Monaghan, R.J. Longbottom, M.A. Rhamdhani, N. Dogan, and M.W. Chapman: *Metall. Mater. Trans. B Process Metall. Mater. Process. Sci.*, 2017, pp. 1–11.

114 B.J. Monaghan, H. Abdeyazdan, N. Dogan, M.A. Rhamdhani, R.J. Longbottom, and M.W. Chapman: *ISIJ Int.*, 2015, vol. 55, pp. 1834–40.

115 F. Verhaeghe, J. Liu, M. Guo, S. Arnout, B. Blanpain, and P. Wollants: *J. Appl. Phys.*, 2008, vol. 103, p. 23506.

116 X. Yu, R.J. Pomfret, and K.S. Coley: *Metall. Mater. Trans. B*, 1997, vol. 28, pp. 275–9.

117 P. Rocabois, J. Lehmann, C. Gatellier, and J.P. Teres: *Ironmak. Steelmak.*, 2003, vol. 30, pp. 95–100.

118 University of Pennsylvania., pp. 1-8

119 G. Urbain: *steel Res. Int.*, 1987, vol. 58, pp. 111–6.

Appendix I Calculation of Diffusion in Stagnant Fluid Control Model

The first version written by Yousef Tabatabaei and Mukesh Sharma. Author corrected mistakes in the RK4 solver and adjusted some parameters to suit the present study.

```
----------------------------------Define function-----------------------------------------------

function dR = Diff_Eqn( R,t,K,D,f )
dR = -K*D/R-f*K*sqrt(D/(pi*t));
end

---------------------------------Numerical solution solver-------------------------------------

% Runge-Kutta Solver
function [t,data] = RK_Solver(R,dt,t_range,K,D,f,Diff_Eqn)
time = t_range(1);
Nsteps = round((t_range(2)-t_range(1))/dt);                    %% number of
steps to take (time).
t = zeros(Nsteps,1);                                            %% N*1
matrix contains 0
data = zeros(Nsteps,length(R));

t(1) = time;                                                    %% store
intial condition
data(1,:) = R';

for i = 2:Nsteps

   k1 = dt*feval(Diff_Eqn,R,time,K,D,f);
   k2 = dt*feval(Diff_Eqn,R+k1/2,time+0.5,K,D,f);
   k3 = dt*feval(Diff_Eqn,R+k2/2,time+0.5,K,D,f);
   k4 = dt*feval(Diff_Eqn,R+k3,time+1,K,D,f);
   R = R + k1/6 + k2/3 + k3/3 + k4/6;

   if R < 1e-11
      fprintf ('Inclusion dissolved completely t= %0.1f s \n',time);
      time = time+dt;
```

```
      t(i) = time;
      data(i,:) = 0;
      break
    else
      t(i) = time;
      time = time+dt;
      data(i,:) = R';
      %data(i)
    end
end
data(i+1:end,:)=[];
t(i+1:end,:)=[];
end

----------------------------------Dissolution time calculation-------------------------------------
clear
clc
dbstop if error
R =100e-6;
K = 0.299;
D = [6e-11];
dt = 0.05;
t_final = 10000;
counter = 1;

textleg = cell(1,1);
for f = 0.55                    %% for loop used to generate multiple solutions with
different f values
   for i=1:length(D)             %% generate multiple solutions with different D values

      t_range = [0.01 10000];                          %% t = 0 causes error in RK4

      [t_data, R_data] = RK_Solver(R,dt,t_range,K,D(i),f,@Diff_Eqn);
      t_final = t_data(end);

      %unnormalized plots
      figure(1)
```

```
        plot(t_data,R_data)
        hold on
        xlabel('Dissolution time');
        ylabel('Equivalent radius');

        %normalized plots
        figure(2);
        plot(t_data./t_final,R_data./R);
        hold on;
        textleg(i)={['f = ' num2str(f)]};
        axis([0 1.1 -0.1 1.1]);
        xlabel('Normalized time');
        ylabel('Normalized radius');
    end
    counter = counter + 1;
    fprintf ('---------------------- \n')
end
legend(textleg);
```

Appendix II Properties of Initial and Al_2O_3 Saturated Slag

Table A.1 CA_2 dissolution

Slag	Composition (wt%)	Temperature (°C)	Density (kg/m^3)	Al_2O_3 concentration (mol/m^3)	Viscosity (Pa·S)
1	46.3SiO_2-30.5CaO-23.2Al_2O_3	1500	2718	6182	9.49
		1550	2705	6153	6.16
		1600	2691	6121	4.10
2	46.3SiO_2-30.5CaO-23.2Al_2O_3	1550	2799	10592	0.493
		1600	2785	10539	0.374
Interface 1	43.1SiO_2-20.0CaO-36.9Al_2O_3	1500	2730	9876	-
	39.0SiO_2-27.2CaO-33.7Al_2O_3	1550	2741	9056	4.86
	38.2SiO_2-26.1CaO-35.7Al_2O_3	1600	2729	9551	3.27
Interface 2	2.48SiO_2-38.0CaO-64.5Al_2O_3	1550	2744	17352	0.683
	4.1SiO_2-35.1CaO-60.8Al_2O_3	1600	2762	16464	0.980

Table A. 2 Al_2O_3 dissolution

Slag	Composition (wt%)	Temperature (°C)	Density (kg/m^3)	Al_2O_3 concentration (mol/m^3)	Viscosity (Pa·S)	Dimensionless concentration	Correction coefficient
1	$46.3SiO_2$-$30.5CaO$-$23.2Al_2O_3$	1550	2705	6153	6.16		
		1600	2691	6121	4.10		
Interface 1	$33.2SiO_2$-$21.6CaO$-$45.2Al_2O_3$	1550	2747	12172	3.94	0.264	0.69
	$31.2SiO_2$-$20CaO$-$48.8Al_2O_3$	1600	2673	12760	2.39	0.299	0.55

Table A.3 SiO_2 dissolution

Slag	Composition (wt%)	Viscosity (Pa·S)	Correction coefficient
1	$54.6SiO_2$-$34.1CaO$-$10.6Al_2O_3$	2.40	0.35
2	$50.5SiO_2$-$38.3CaO$-$10.6Al_2O_3$	1.25	0.24
3	$37.1SiO_2$-$36.4CaO$-$26.5Al_2O_3$	0.601	0.13
4	$42.3SiO_2$-$38.8CaO$-$18.9Al_2O_3$	0.469	0.08
5	$45.3SiO_2$-$43.7CaO$-$10.4Al_2O_3$	1.08	0.15
6	$42.8SiO_2$-$46.6CaO$-$10.8Al_2O_3$	1.02	0.1
Sat 1	$68.3SiO_2$-$23.1CaO$-$8.6Al_2O_3$	192	-
Sat 2	$67.4SiO_2$-$25.3CaO$-$7.2Al_2O_3$	122	-
Sat 3	$70.4SiO_2$-$17.1CaO$-$12.4Al_2O_3$	663	-
Sat 4	$69.0SiO_2$-$21.0CaO$-$10.0Al_2O_3$	295	-
Sat 5	$67.0SiO_2$-$26.5CaO$-$6.5Al_2O_3$	95.9	-
Sat 6	$66.6SiO_2$-$27.6CaO$-$5.8Al_2O_3$	77.1	-

Appendix III Estimation of Slag Properties

It is well known that dissolution of inclusions largely depends on the properties of slag such as density and viscosity [2]. The experimental data on slag density and viscosity are mainly summarized in the Slag Atlas [65]. However these properties are strong function of temperature and composition and it is difficult to directly use the data available in the literature. Moreover, different experimental approaches may also influence the reported values. Therefore, models are used to estimate the density and viscosity of slags. These models are successfully applied to wide range of temperature and slag composition relevant to steelmaking conditions. The author recognizes the potential inaccurate estimation with using models.

The density of slag can be calculated based on the molar volume of individual constituents at 1500°C. Most slag components have a constant molar volume, while molar volume of Al_2O_3 and SiO_2 are function of their molar fraction because slag with Al_2O_3 and SiO_2 may form rings and complexes [65]. The recommended values for partial molar volume of slag constituents used in this study at 1500°C are listed in Table A.4. The density of slag ρ at temperature T can be calculated using Equation (A.1) and Equation (A.2). V_n and X_n are molar volume and molar fraction of component n respectively.

Table A.4 Recommended partial molar volume of slag constituents at 1500°C [65]

Constituent	Molar volume V (cm^3/mol)
Al_2O_3	$28.31 + 32X_{Al_2O_3} - 31.45{X_{Al_2O_3}}^2$
CaO	20.7
SiO_2	$19.55 + 7.966X_{SiO_2}$

$$V_{slag} = [1 + 0.0001(T - 1500)] \sum_{n=1}^{n} X_n V_n \quad \text{(A.1)}$$

$$\rho'_{slag} = \frac{\sum_{n=1}^{n} X_n M_n}{V_{slag}} \quad \text{(A.2)}$$

There are two viscosity models available in Slag Atlas. The Riboud's model is valid for slag with SiO_2 > 50 wt%, which is not satisfied by the slags used in this study. Therefore, slag viscosity was calculated using the Urbain model in this work. Scientific basis of this model has been documented elsewhere [119]. This model classifies all slag constituents into three categories, glass formers, modifiers, amphoterices, which have normalized weight percent of X_G^*, X_M^* and X_A^* respectively [65].

$$X_G^* = X_{SiO_2} + X_{P_2O_5} \quad \text{(A.3)}$$

$$X_M^* = X_{CaO} + X_{MgO} + X_{Na_2O} + X_{K_2O} + 3X_{CaF_2} + X_{FeO} + X_{MnO} + 2X_{TiO_2} + 2X_{ZrO_2} \quad \text{(A.4)}$$

$$X_A^* = X_{Al_2O_3} + X_{Fe_2O_3} + X_{B_2O_3} \quad \text{(A.5)}$$

Base on normalized weight fractions, viscosity parameter A and B can be calculated using Equation (A.6) to (A.12). Slag viscosity can be calculated by substituting temperature and composition dependent parameter A and B into Equation (A.13).

$$\alpha = \frac{{X_M}^*}{{X_M}^* + {X_A}^*} \quad \text{(A.6)}$$

$$B_0 = 13.8 + 39.9355\alpha - 44.049\alpha^2 \quad \text{(A.7)}$$

$$B_1 = 30.481 - 117.1505\alpha + 139.9978\alpha^2 \quad \text{(A.8)}$$

$$B_2 = -40.9429 + 234.0486\alpha - 300.04\alpha^2 \quad \text{(A.9)}$$

$$B_3 = 60.7619 - 153.9276\alpha + 211.1616\alpha^2 \quad \text{(A.10)}$$

$$B = B_0 + B_1{X_G}^* + B_2({X_G}^*)^2 + B_3({X_G}^*)^3 \quad \text{(A.11)}$$

$$-\ln A = 0.2693B + 11.6725 \quad \text{(A.12)}$$

$$\eta = ATe^{\frac{1000B}{T}} \quad \text{(A.13)}$$